METAMORPHISM OF METACHERT FROM THE SOUTHERN ALPS, NEW ZEALAND

A THERMODYNAMIC FORWARD MODELLING STUDY

Jill Fernandes

A thesis submitted to Victoria University of Wellington as requirement for the

degree of

Master of Science

Geology

2016

School of Geography, Environment and Earth Sciences, Victoria University of

Wellington

ABSTRACT

Scattered, scarce occurrences of garnet- and quartz-rich metamorphic rock, probably derived from Mn- and Fe-rich chert, occur within metamorphosed greywacke sequences worldwide. The metamorphism of such garnetiferous metacherts has not previously been investigated using modern thermodynamic forward modelling techniques due to the lack of appropriate, internally-consistent activity-composition *(a–x)* models for Mn-bearing minerals. The present study applies thermodynamic forward modelling using the recently-proposed *a–x* models of White *et al.* (2014) to investigate the metamorphism of garnetiferous metachert samples from the Southern Alps, New Zealand.

Pressure-temperature *(P–T)* pseudosections are used in combination with results from petrography, element composition mapping using micro X-ray fluorescence (µXRF) and scanning electron microscope (SEM) methods, and garnet composition data from analytical transects by electron probe microanalysis (EPMA), to study metachert metamorphism. All the samples are compositionally layered, so the possibility exists that an input bulk rock composition might not match the effective bulk composition at the site of garnet growth. If a mineral assemblage stability field in a calculated *P–T* pseudosection matched the mineral assemblage in the rock, this was taken as an initial indication of a permissible input bulk rock composition. In that case, refined constraints on the *P–T* conditions were sought by comparing calculated and measured garnet compositions. The studied rocks include samples that are carbonate-bearing, which require consideration of the effects of fluid composition in mixed H_2O–CO_2 fluids, as well as a sample in which the garnet is strongly zoned, texturally-complex, and inferred to be of polymetamorphic origin. The effects of element fractionation by that garnet were investigated by recalculating the *P–T* pseudosection using a new bulk rock composition with the garnet core content removed. In none of the samples did the calculated and observed composition isopleths for the garnet cores match, suggesting that initial garnet nucleation in these Mn-rich rocks was locally controlled. For most samples in which the calculated and observed mineral assemblages matched, successful estimates of the peak

Fernandes, J.

metamorphic conditions were obtained. A garnet chert (A12E) from the mylonite zone of the Alpine Fault at Vine Creek, near Hokitika, gave a tight intersection of composition isopleths, indicating peak metamorphic conditions of 510 °C/5.5 kbar, after recalculation to correct for element fractionation by the strongly-zoned garnet. This tight, modern constraint is within error of previously-reported results from traditional geothermobarometry (420–600 °C/5.9–13 kbar) and Raman spectroscopy of carbonaceous material (RSCM T = 556 °C) from nearby sites. A peak metamorphic estimate of 520–550 °C/7–10 kbar was obtained from a dolomite-bearing sample from the garnet zone near Fox Glacier (J34), in good comparison with published temperatures from Raman spectroscopy of carbonaceous material in nearby metagreywacke samples (526–546 °C). The prograde metamorphic $P–T$ path was probably steep, based on growth of the garnet core at ~475–535 °C/5–9 kbar. The successful results for these garnet chert samples show that the new a-x models for Mn-bearing minerals extend the range of rock types that are amenable to pseudosection modelling.

Results obtained in this study also serve to highlight several possible concerns: a) garnet nucleation and initial growth in very Mn-rich rocks may be subject to local compositional or kinetic controls; b) bulk rock compositions may not always mimic the effective bulk composition; c) the existing $a–x$ models for Mn-bearing minerals and white micas may need refining; and d) some rocks may simply be ill-suited to thermodynamic forward modelling. Items a) and b) may be indicated by the common observation of a mismatch between predicted and measured garnet composition isopleths for garnet cores, and by a mismatch between garnet composition isopleths and the appropriate mineral assemblage field for sample AMS01, from the mylonite zone, Hari Hari, Southern Alps. For item c) every $P–T$ pseudosection calculated using the new $a–x$ models for Mn-bearing minerals showed garnet stable to very low temperatures below 300 °C. In addition, the $P–T$ pseudosection for an oligoclase-zone metachert (Sample J36) from Hari Mare stream, Franz Josef - Fox Glacier, indicated that the white mica margarite should be present instead of plagioclase (oligoclase), for a rock in which oligoclase is present and margarite is absent, a problem previously noted elsewhere. Item d) is exemplified by a very garnet-rich ferruginous metachert sample (J35, garnet zone, headwater region, Moeraki River, South Westland) which proved impossible to model successfully due to its complex

Fernandes, J.

mineral growth and deformation history. This sample contained multiple generations of carbonate with differing compositions, amphibole (not incorporated for modelling with the new *a–x* models for Mn-bearing minerals), large porphyroblasts of Fe-Ti oxides (magnetite associated with smaller, possibly later-formed ilmenite), and the garnet bands were offset by late deformation.

The garnetiferous metachert samples studied here preserve in their textures and compositions clues to their growth mechanism and metamorphic history. The textures in at least two of the samples are consistent with the diffusion controlled nucleation and growth model for garnet. This research has successfully used state of the art thermodynamic modelling techniques in combination with the latest internally consistent *a-x* models on Mn-rich metachert, for the first time, extracting *P–T* conditions of the metamorphism of garnetiferous metachert from the Southern Alps.

Fernandes, J.

ACKNOWLEDGEMENTS

Fernandes, J.

TABLE OF CONTENTS

Fernandes, J.

Fernandes, J.

LIST OF FIGURES

Fernandes, J.

Fernandes, J.

Fernandes, J.

Fernandes, J.

Fernandes, J.

Fernandes, J.

LIST OF TABLES

Fernandes, J.

1. INTRODUCTION

Metamorphism of the rare garnetiferous metachert will be analysed from samples that occur within the metagreywacke-dominated Alpine Schist, Southern Alps (Fig. 1.1), South Island, New Zealand.
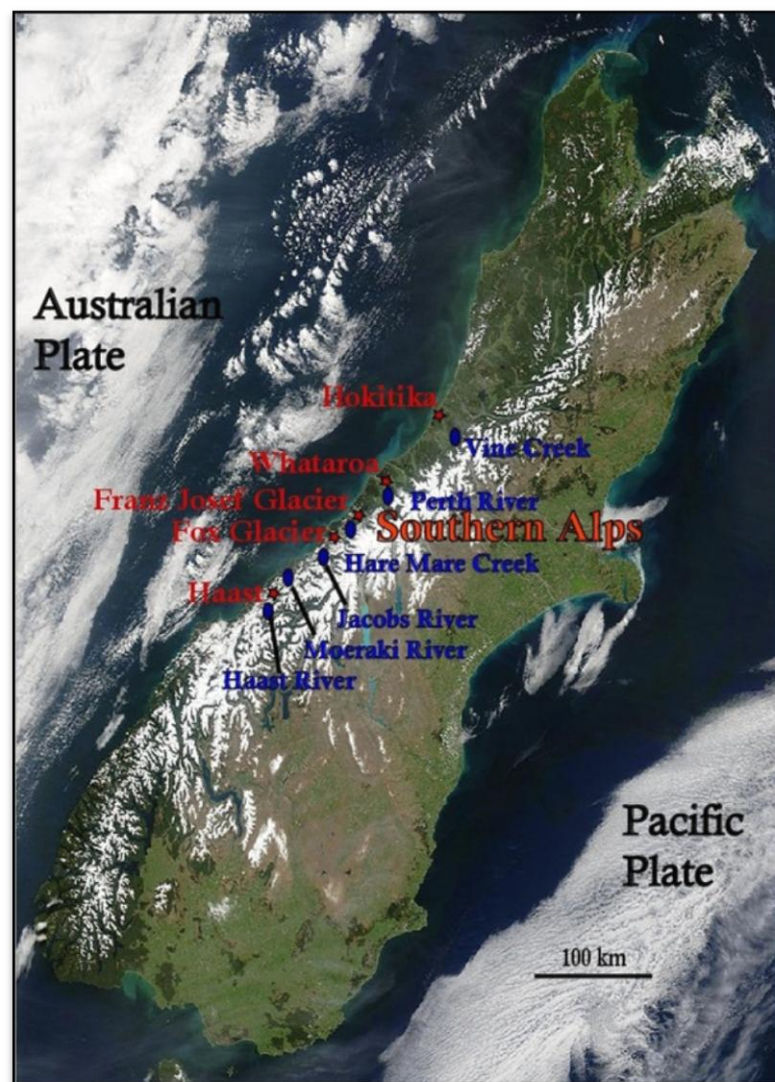
Figure 1.1 Satellite imagery showing snow covered Southern Alps (Schmaltz, 2007), South Island of New Zealand and locations of study area from Haast to Hokitika.

Fernandes, J.

The rare garnetiferous metacherts that make up less than 0.05% of the rocks in the Southern Alps (Tenzer *et al.,* 2011), have never been studied using modern forward modelling techniques, due to lack of appropriate $a-x$ models that deal with their Mn-rich composition. The metachert in the Alpine Schist is typically a Mn-rich siliceous rock composed mainly of quartz, Mn-garnet, and micas with minor or accessory minerals such as rutile, apatite, tourmaline, magnetite, haematite and kyanite (Grapes *et al*., 1985). The metacherts investigated in the present study typically consist mainly of alternating layers of quartz and garnet, with interspersed micas. The garnets are typically compositionally zoned. Their zonation composition information will be used in combination with pseudosections for the first time, to study metachert from the Southern Alps. The garnets in the metachert samples preserve within their texture and composition information that can potentially be used to unravel the metamorphic history of the rock.

Petrographic forward modelling has previously been successfully applied to a few, carefully selected greyschist samples from a single site in the garnet zone Alpine Schist near Hokitika, Southern Alps, New Zealand (Fig. 1.1 & Fig. 2.1, Vry *et al.*, 2008). The results of that study clarified the metamorphism of greywacke and yielded the first detailed metamorphic $P-T$ path ever obtained from garnet-albite zone greyschist. Except for the Vry *et al.* (2008) research and a few recent $P-T$ estimates from (Beyssac *et al*., 2016) utilising a pseudosections, all published $P-T$ estimates for samples of Alpine Schist have been obtained using traditional geothermobarometry methods. Despite the early success of Vry *et al.* (2008) and the abundance of metamorphosed greywacke in the Southern Alps, many greyschist samples still cannot be investigated in this way. Samples that contain carbonate require an understanding of fluid composition and the controlling effects of an evolving, mixed H_2O-CO_2 fluid on metamorphic processes and phase equilibria. In addition, some greyschist samples preserve textural and compositional evidence of a complex metamorphism-deformation-fluid flow history (J. Vry, pers. comm., 2013) that has partially adjusted their bulk-rock chemistry, making basic petrographic forward modelling impossible. Modern petrographic forward modelling of garnet-bearing metachert could potentially yield improved constraints on local metamorphic $P-T$ conditions and $P-T$ paths, which are otherwise unobtainable from the more abundant associated greyschist.

PREVIOUS RESEARCH ON METACHERT

The metamorphism of garnet metachert has remained largely unstudied. Previous studies of metachert in Southern Alps have focused primarily on minerals within the metacherts such as Cooper (1980) and Grapes (1993). Grapes (1993) studied the Ba content of micas in two samples of metachert, one of which (no. 34, Victoria University (VUW) number 28666) is included in Grapes *et al.* (1985), and is sample J34 in this study. Grapes (1993) suggested that Ba precipitated along with silica during chert formation in a subaqueous environment, and that Ba-rich metachert forms in association with oceanic basalt. Cooper (1980) examined in detail the retrograde alteration of kyanite in a float sample of metachert from Jacobs River (Fig. 1.1). There has not been a detailed thermodynamic forward modelling study of metachert, yet. This will be the first research to investigate metachert using thermodynamic forward modelling techniques.

AIMS OF THIS RESEARCH

Garnet is a very useful petrogenetic indicator for studying metamorphic processes and events of the rock in which it occurs (Blackburn & Navarro, 1977). Previously, the Mn-rich bulk compositions of the metacherts made them unsuitable for metamorphic studies by either traditional or modern forward modelling methods. The proposed research makes use of recent advances in thermodynamic modelling of Mn-rich minerals (White *et al.*, 2014) to undertake the first modern, petrographic forward modelling studies of the metamorphism of garnet metachert, from the Alpine Schist of the Southern Alps in the region from Hokitika–Haast (Fig. 1.1). The study will investigate garnet-bearing chert samples,

i.   to predict theoretically, for the first time, how the metamorphic assemblages and mineral compositions of these rocks respond to changing metamorphic pressure-temperature (*P–T)* conditions, through calculation of *P–T* pseudosections, using the most up-to-date internally-consistent thermodynamic data and activity composition models;

ii. to use the results of the calculations together with mineral composition data to gain a better understanding of the peak metamorphic pressure conditions that affected the studied samples and the associated rocks;
and hopefully,

iii.   to extract detailed *P*–*T* path information that will illuminate our understanding of the overall metamorphic history of the localities of the analysed rocks.

Traditional thermobarometry uses equilibrium thermodynamics of balanced equations between mineral end members in combination with observed mineral compositions. The forward modelling method involves calculation of pseudosections and prediction of mineral equilibria using equilibrium thermodynamics, for a given bulk composition. Pseudosections are used in combination with the real rock mineral assemblage, proportions and compositions to predict *P*–*T* conditions. In addition forward petrographic methods can predict the stability of mineral assemblages (Powell & Holland, 2008) and the *P*–*T* conditions under which new phases are added to, or removed from an assemblage. Hence, the forward modelling technique can be more powerful than conventional thermobarometry for constraining metamorphic histories (Powell and Holland, 2010). The present research uses the forward modelling technique to obtain *P*–*T* information from garnetiferous metachert.

THE FORWARD MODELLING APPROACH

The capacity to analyse and extract metamorphic histories from rocks has significantly improved with the shift from inverse modelling (conventional thermobarometry methods) to forward modelling (pseudosection methods). The forward modelling approach to study rock metamorphism involves the use of thermodynamically calculated pseudosections based on the bulk rock composition in combination with quantitative methods to extract *P*–*T* information from a rock (Powell and Holland, 2010).

THERMODYNAMIC FORWARD MODELLING TECHNIQUE

Forward modelling involves the use of thermodynamically calculated pseudosections that are based on the assumption that all the phases in the rock assemblage were in a state of equilibrium (Powell & Holland, 2010). It is built up by reaction lines (zero

4

mode lines), across which a phase is either gained or lost. Pseudosections show the variation in mineral assemblage with $P-T$ for a given bulk composition (Powell & Holland, 2010). These diagrams have a similar topology for chemically similar rocks but the boundaries of the mineral assemblage stability fields vary in position as the components in the bulk composition vary. A pseudosection graphically presents the interdependence of mineral assemblages to variables dominating metamorphic conditions (e.g. P, T, X where X is the composition). This diagram represents stability fields and changes in equilibrated assemblages varying with temperature and pressure, for a specific bulk composition. Once a $P-T$ pseudosection is calculated, the theoretically predicted mineral compositions or modal percentages of individual minerals can be contoured upon it. By comparing those predictions with results of electron probe microanalysis (EPMA) studies of the minerals in thin-section from that sample, it should be possible to more tightly constrain the peak metamorphic conditions and gain new insights into the changing conditions along the metamorphic $P-T$ path.

SUMMARY

This study uses the forward modelling technique on garnet metacherts of the Alpine Schist. THERMOCALC (Powell & Holland, 1988) has been used to calculate $P-T$ pseudosections, using the new, internally-consistent *a-x* models for Mn-bearing minerals that deal with Mn-rich rock compositions in a rigorous way (White *et al*., 2014).

Fernandes, J.

2. GEOLOGICAL SETTING

TECTONIC SETTING

The Southern Alps of New Zealand (Fig. 1.1) which extend from the northeast to southwest of the South Island, are a product of the ongoing oblique continental convergence of the Australian and Pacific Plates (Fig. 1.1 & 2.1), at the Alpine Fault (Fig. 2.1). The Pacific-Australian boundary is presently a transpressional setting that has a dextral reverse slip on the southeast dipping Alpine Fault. The relative displacement is 34–42 mm year^{-1} at 071 ± 2° (Wellman, 1972; Little *et al*., 2002a; Little *et al*., 2005) and the uplift rate is 8–11mm year^{-1} (Simpson *et al*., 1994; Walcott *et al.*, 1998; Sutherland *et al.,* 2006). More than half of the plate convergence is accommodated for by the Alpine Fault boundary between the Pacific and Australian Plates (Norris *et al*., 1990; Norris & Cooper, 1995; Walcott, 1998). Initially the boundary was dominantly a strike-slip fault (at 45 Ma), which then changed to an oblique slip fault at 25–22 Ma, which is the present modern phase of plate boundary development (Sutherland, 1999). The modern phase of oblique convergence led to mountain (Southern Alps) building which began at 6−8 Ma (Walcott *et al.*, 1998; Batt *et al*., 2004). This modern phase of tectonism, accompanied by increased rates of shortening (Walcott *et al.*, 1998; Batt *et al*., 2004), was the effect of changing subduction kinematics of the Australian and Pacific plates (King, 2000). The Pacific Plate has been exhumed in the last 3−5 Ma forming the Southern Alps (Little *et al*., 2002b). The change from strike-slip tectonics to oblique convergence has led to shortening of 90 ± 20 km across the Southern Alps and 230 km of dextral strike slip along the Alpine Fault, inferred from plate reconstructions studies (Walcott *et al*., 1998; Little *et al*., 2005).

The Late Cenozoic phase of uplift and exhumation has exposed a narrow strip of metamorphic rocks (the Alpine Schist) that stretches NE-SW ~ 400 km along the eastern side of the Alpine Fault (Fig. 2.1, Grapes, 1995; Cooper & Ireland, 2015). The Alpine Schist is comprised mainly of texturally intricate metamorphosed greywacke (greyschist) interlayered with rarer rock types, such as metachert and metabasites (Little *et al*., 2002a; Vry *et al*., 2004).

Fernandes, J.

Map of the South Island of New Zealand
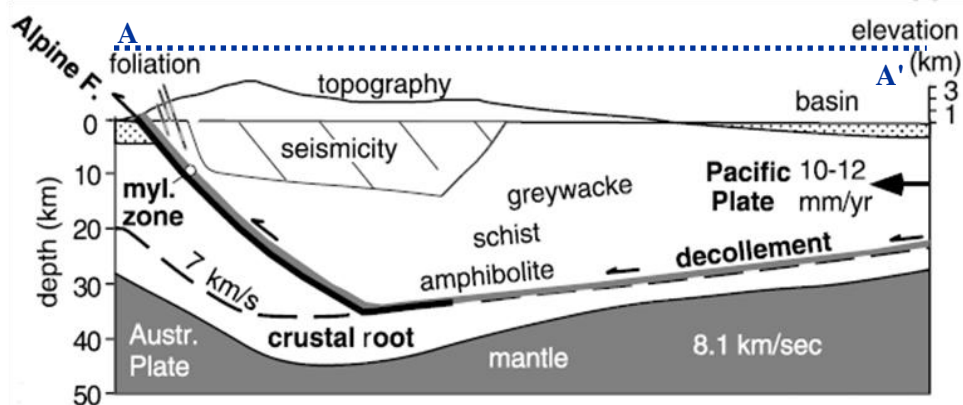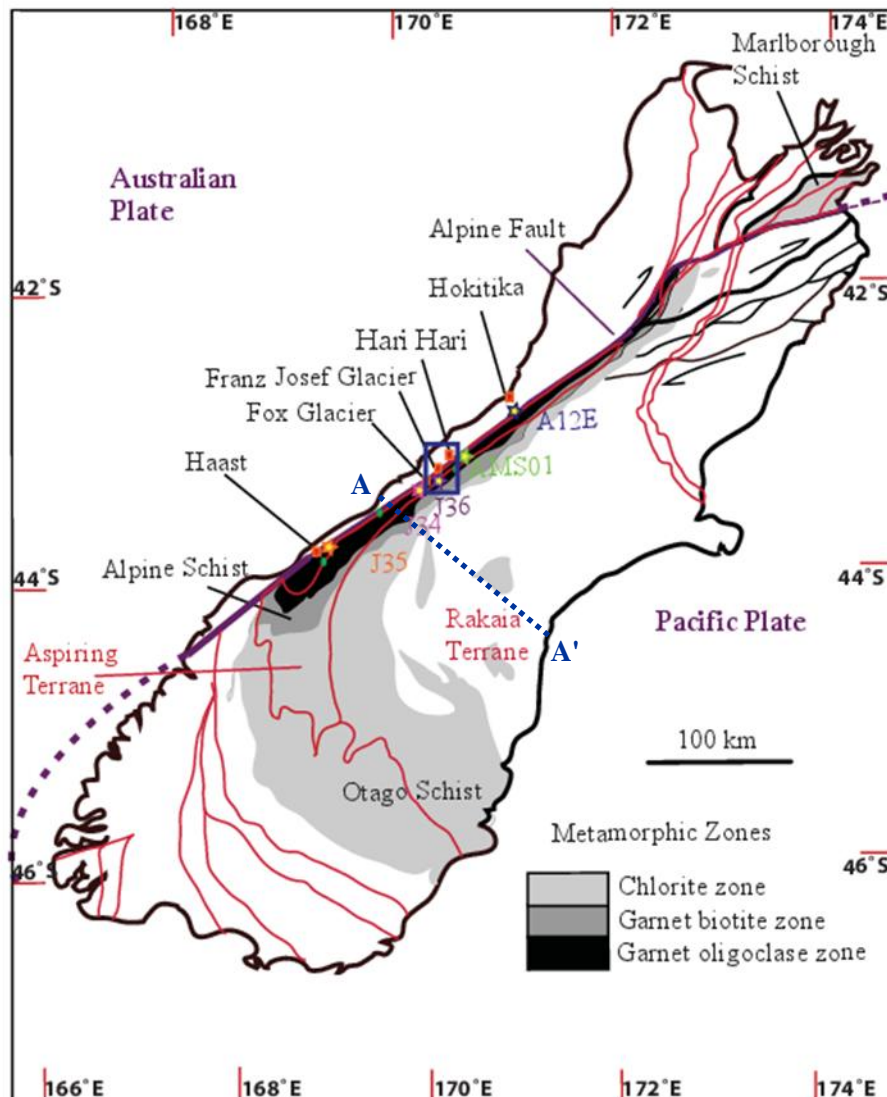
Figure 2.1. Map of the South Island, New Zealand showing metamorphic zones, terranes (Cooper & Ireland, 2013) and sample locations for A12E, AMS01, J34, J35 and J36. The red lines are terrane boundaries shown in detain in Fig. 2.2 below. The blue box is the location of map shown in Fig. 2.3. Cross-section A-A' shows a vertical profile interpretation of the crustal structure perpendicular to the Alpine Fault.

7
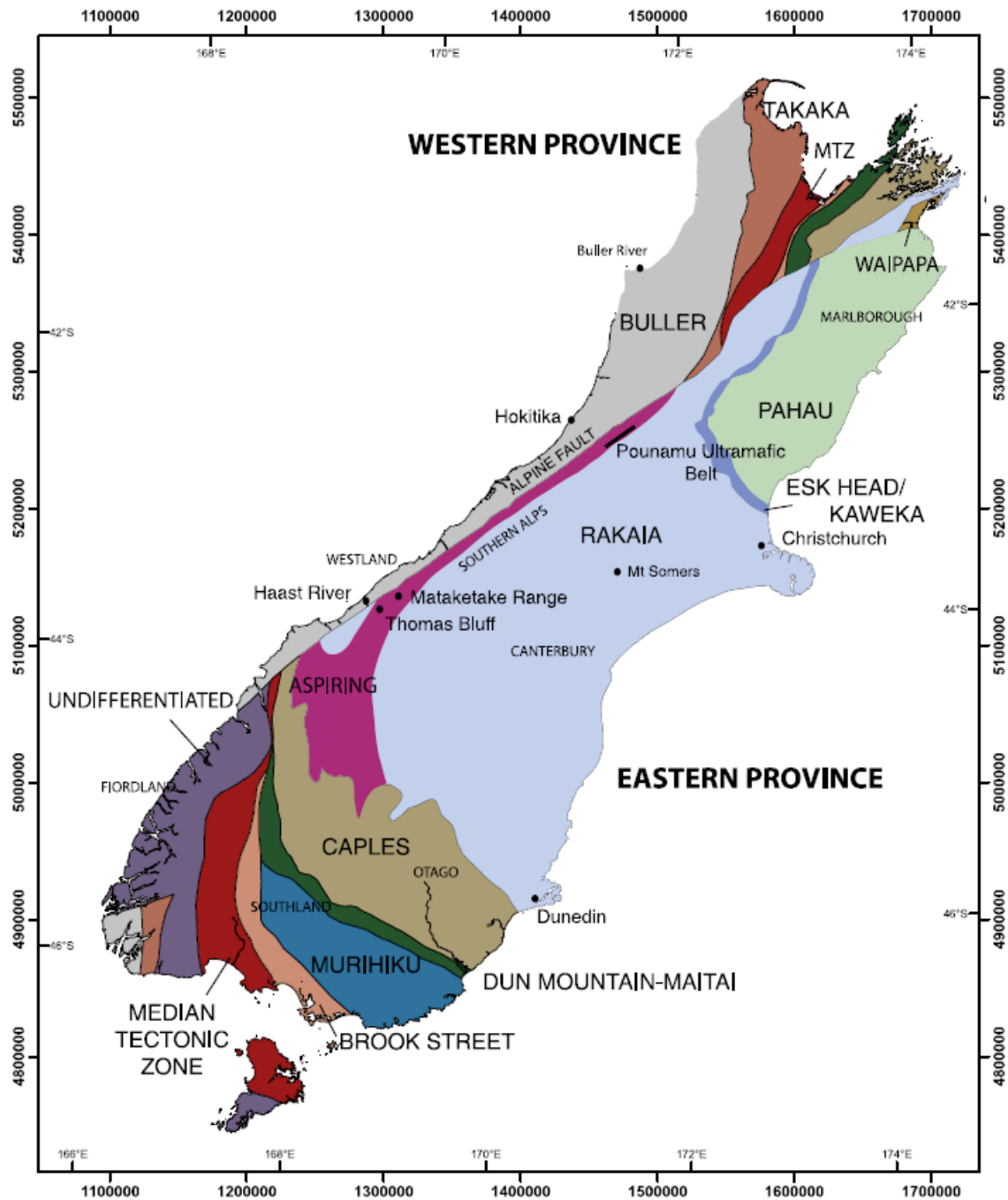
Figure 2.2. Map of the South Island of New Zealand, showing its constituent terranes. After Cooper & Ireland (2013), this figure provides details of the terranes demarcated by the red lines of Fig. 2.1.

The abundant greywacke of the Alpine Schist record a polymetamorphic and polydeformational history (Grapes & Watanabe, 1992; Grapes, 1995; Little *et al.*, 2002a; Vry *et al.*, 2004). The Alpine Schist together with the Marlborough Schist in the north and the Otago Schist in the south, comprise the Haast Schist belt (Fig. 2.1). In the central Southern Alps (Franz Josef–Fox Glacier area), the Alpine Schist belt is narrowest and tight to isoclinal folding has aligned the strike of the schistosity subparallel to the Alpine Fault (Little *et al.*, 2002a). Away from the central regions as the schist belt widens (Fig. 2.1), the folds are more open, aligning the pre-existing schistosity strike almost perpendicular to the Alpine Fault (Little *et al.*, 2005; Beyssac *et al.*, 2016).

The metamorphic record in the Alpine Schist is inherited from the early Jurassic – Cretaceous (Adams & Gabites, 1985; Sheppard *et al.*, 1985; Chamberlain *et al.*, 1995; Vry *et al.*, 2004) and for the most part is unrelated to the Cenozoic modern phase of exhumation of the Alpine Schist and the development of the Southern Alps.

FABRICS OF THE ALPINE SCHIST

The rocks of the Alpine Schist belt preserve a record of the polydeformational metamorphism in its fabric and structure (Cooper, 1974; Grapes & Watanabe, 1992; Grapes, 1995; Little *et al.*, 2002a; Little *et al.*, 2005). These fabrics (Fig. 2.3) are preserved in the metamorphosed greywacke within which the rare thin metachert layers occur, and hence, these fabrics provide a textural context for the metachert of this research. Textural zones and fabrics indicate the intensity of foliation development and accommodation of the shearing stress (Grindley, 1963; Little *et al.*, 2005). Little *et al.* (2002a) has described deformation events D_1– D_4 for fabrics of the Alpine Schist near Franz–Josef Glacier and in Whataroa and Perth River Valleys (Fig.1.1 & 2.3).

EARLY FABRIC DEVELOPMENT

Deformations D_1 and D_2 are early events, both late Mesozoic in age, and produce fabrics S_1 and S_2 respectively. Foliations S_1, S_2 and S_3 are extensive throughout the

9

western part of the Southern Alps. The early foliations (S_1, S_2) are subparallel to the metamorphic isograds (Little *et al*., 2002a; Beyssac *et al*., 2016). The early metamorphic fabric S_1 of deformation D_1, has been overprinted by a later, more dominant, deformation D_2 producing fabric S_2. This fabric (S_2) is further overprinted by Cenozoic mylonitisation along the Alpine Fault and the uplift and exhumation of the Southern Alps (Craw *et al*., 1994).

The effects of Jurassic metamorphism related to development of the Otago schist are recorded in some microtextures in the Alpine Schist e.g. inclusion trails in porphyroclastic garnet and crenulated trails of graphitic material preserved within biotite porphyroblasts (Little *et al*., 2002a; Vry *et al*., 2004). It is possible that garnet from the Alpine schist metachert may be wholly, or have early cores, inherited from the Jurassic episode S_1 of metamorphism.

PEAK METAMORPHISM AND POST METAMORPHIC FABRIC DEVELOPMENT

The foliation S_3 (Fig. 2.3, sketch of the Main planar zone fabrics) is steeply dipping axial planar to the folds of the pre-existing fabric (Little *et al*., 2002a; Beyssac *et al*., 2016). The S_2 (Fig. 2.3, sketch of the Main planar zone fabrics) laminations are crenulated and overprinted by the younger Alpine foliation S_3 that formed during the D_3 metamorphism in the (Little *et al*., 2002a) mid Cretaceous to early Miocene. In the non mylonitic schists, D_3 is represented by porphyroblast growth, peak metamorphism and development of the Alpine foliation (S_3, Fig. 2.3 sketch of the Main planar zone fabrics). The pre-existing Mesozoic foliation (S_3) was constructively reinforced in the Cenozoic (Little *et al*., 2002a; Toy *et al*., 2008) by a late tectonic overprint. The Late Cenozoic mylonitic foliation (S_m, Fig. 2.3 sketch of mylonite/ distal mylonite zone fabrics) that occurs as extensional crenulation cleavage fabric that formed as a product of shear strain incurred during vertical thickening and rotation of the schists, is the youngest fabric preserved in the Alpine Schists (Fig. 2.3, Toy *et al*., 2008).
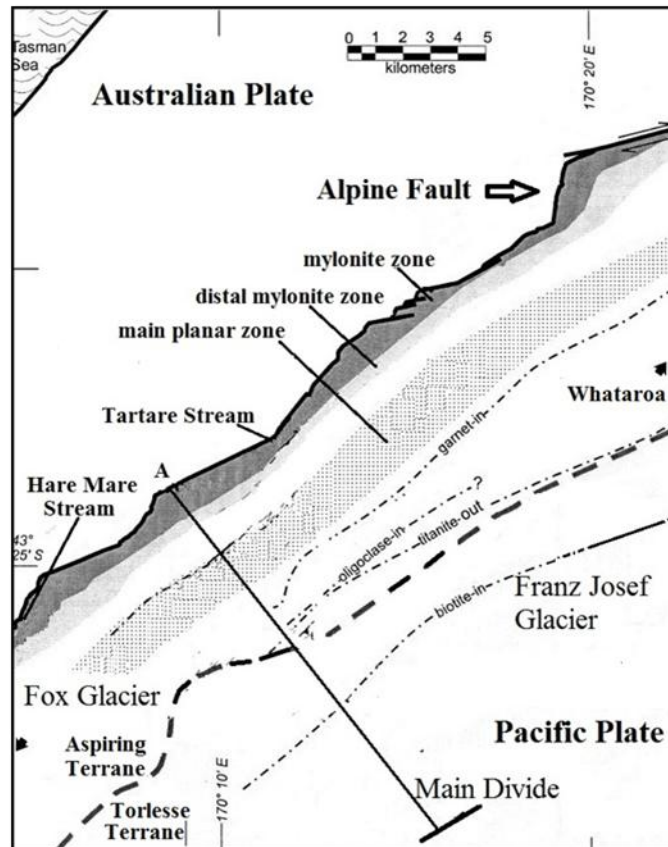
Figure 2.3. Schematic description of the mylonite zone and cross-section showing structural boundaries at depth near Franz Josef- Fox Glacier. Sketches of S2, S3 and Sm fabrics, simplified from Little *et al*. (2002a). The dashed line represents the division between the Aspiring and Torlesse Terranes. For map location refer to blue box in Fig. 2.1.
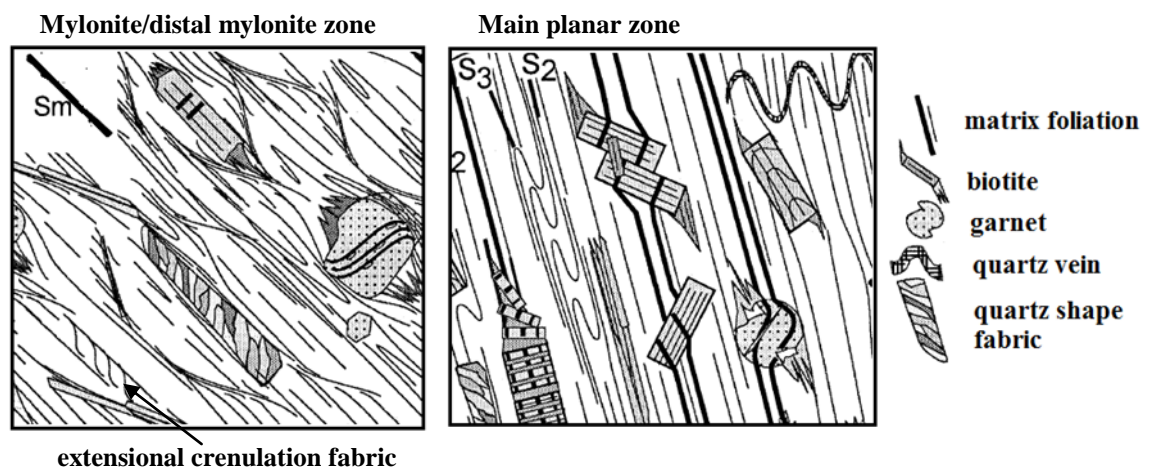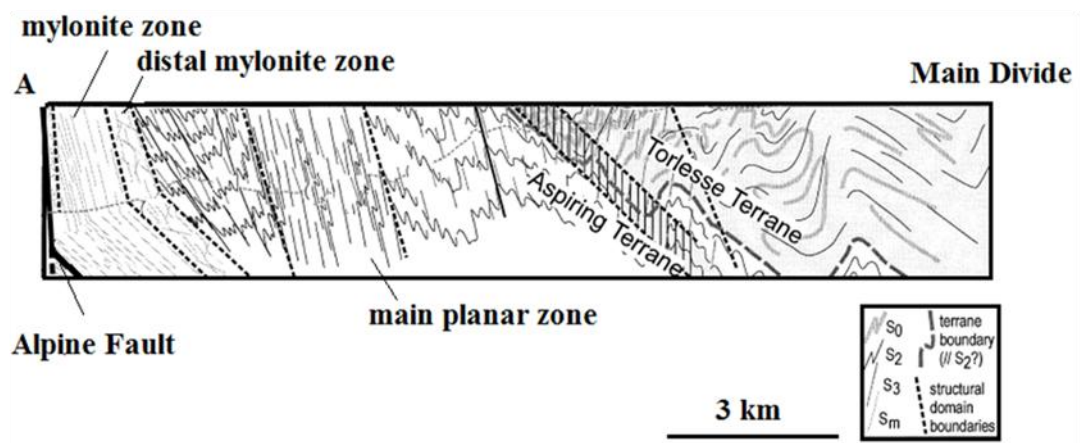
METAMORPHISM

Rocks of highest metamorphic grade in the Alpine Schist, crop out immediately adjacent to the Alpine Fault and grade eastwards into rocks of progressively lesser metamorphic grade towards the non-schistose greywacke (Fig. 2.1, Grapes & Watanabe, 1992a; Grapes, 1995; Little *et al*., 2002a; Cooper & Ireland, 2013). Metamorphic grade changes are as follows — from high grade K-feldspar zone (amphibolite facies) adjacent to the Alpine Fault, to garnet oligoclase schists, through to biotite schists (greenschist facies), to a chlorite zone of semischists and finally to the low grade prehnite-pumpellyite facies (sub-greenschist facies). The metamorphic zones (1) chlorite zone, (2) garnet and biotite zones and (3) garnet-oligoclase zone (Fig. 2.1) are steeply dipping, and subparallel to the structural trend of the Southern Alps (Grapes & Watanabe, 1992; Little *et al*., 2002a; Beyssac *et al*., 2016). The high-grade metamorphic assemblages in the Alpine Schist are inherited from events prior to the modern Cenozoic phase (Grapes, 1995; Walker and Mortimer, 1999; Little *et al*., 2002a) and isograd mineral zonation for the most part represents the thermal structure of the Mesozoic (Grapes & Watanabe, 1992).

Table 2.1. Temperature results from previous temperature studies in the area of the chosen samples for this study.

Sample		*T*'s from RSCM[1]	*T*'s from other studies
J34	Fox Glacier	526–546 °C	650–700 °C[2], 415–625 °C[3]
J35	Moeraki River	552–583 °C	530–550 °C[4]
J36	Franz Josef	530–571 °C	415–625 °C[3]
A12E	Near Hokitika	556 °C	420–600 °C[5]
AMS01	Hari Hari	382–544 °C	

[1]Raman spectroscopy of carbonaceous material; Results from Beyssac *et al*. (2016)
[2]Cooper (1980)
[3]Grapes & Watanabe (1992)
[4]Wallace (1975)
[5]Pepper (2000)

Figure 2.4 shows the metamorphic isograds and results of RSCM T's (Beyssac *et al*., 2016) from the Central parts of the Southern Alps. Figure 2.4b clearly shows that temperatures are highest closest to the fault and decrease away from the fault. Figure

Fernandes, J.

2.4b shows colour coded temperatures along the Alpine Fault. Table 2.1 shows the expected temperatures for the five samples of this study.
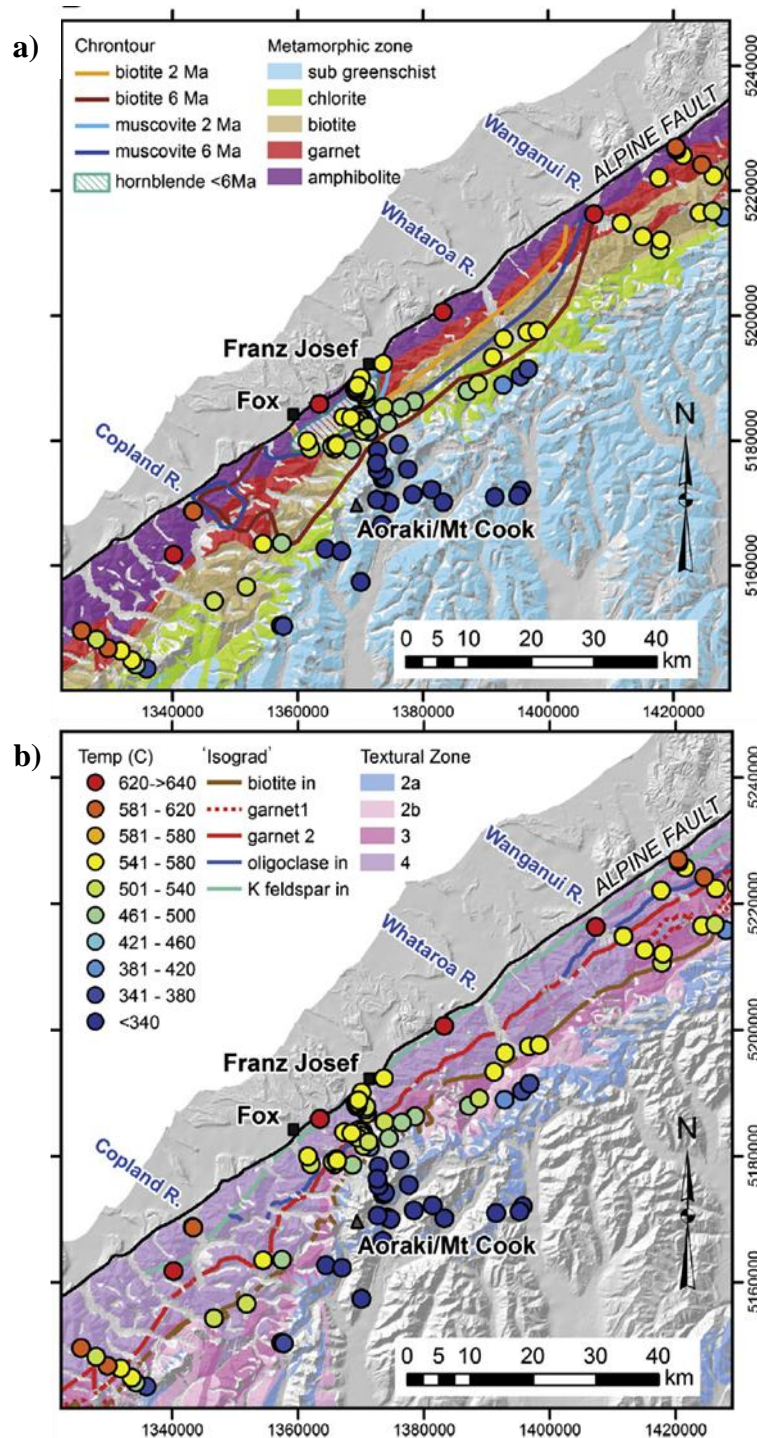
Figure 2.4. Map of the Franz-Josef and Fox regions (Central Southern Alps) showing a) mineral isograd boundaries b) RSCM temperature data, after Beyssac *et al*., 2016.

PREVIOUS STUDIES ON METAMORPHIC CONDITIONS FOR THE SAMPLE AREAS

Cooper (1980) obtained a *P−T* path, from schist in the amphibolite facies, with peak pressures of 10 kbar and temperatures from 650−700 °C for the rocks around Jacobs River (Fig. 1.1). Wallace (1975) determined metamorphic temperatures of 530−550°C on the basis $\delta^{18}O/^{16}O$ isotope geothermometry of quartz and magnetite in metachert of rocks within the oligoclase zone, Moeraki River (Fig. 1.1), South Westland. Cooper (1970) used oxygen isotope thermometry results to suggest that oligoclase zone metachert from Haast River (Fig. 1.1) attained temperatures of ~600−700 °C (Cooper, 1980). In studies of Alpine Schist from the Franz Josef-Fox Glacier area (Fig. 1.1 & 2.1), Grapes & Watanabe (1992) obtained peak *P−T* estimates of 415−625 °C and 5.2−9.2 kbar for ten schist samples in the oligoclase zone. All the calibrations used predate the new activity-composition (*a−x*) models for Mn-bearing minerals (White *et al.*, 2014). Sample A12E of the present study is from a suite of rocks analysed by Pepper (2000) using traditional petrographic methods; temperature estimates were 420−600 °C and pressures of 5−10.5 kbar.

AGES FOR METACHERT OF THE ALPINE SCHIST

The exact ages of the polymetamorphic Alpine Schist are still uncertain. A range of K-Ar, Ar/Ar ages for the Alpine schist have been obtained from 6 to 143 Ma with youngest ages estimated closest to the fault (Sheppard *et al*., 1975), implying that the deepest parts of the Schists are exposed closest to the Alpine Fault (Adams *et al*., 1985; Adams & Gabites, 1985; Grapes & Watanabe, 1992a; Little *et al.*, 1999).
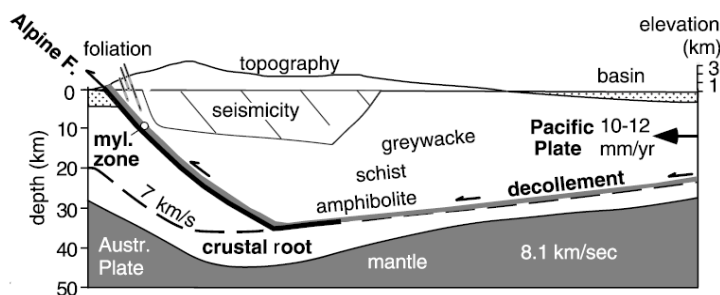
Figure 2.5. Showing a sketch of the crustal structure across the Southern Alps, after Vry *et al*., 2004.

The oldest ages from the peak Jurassic metamorphism were initially considered to be 190–200 Ma (early Jurassic; Adams *et al*., 1985) or 170–180 Ma (Middle Jurassic; Little et al., 1999), from K-Ar and Ar-Ar dating (Mortimer, 2000).

In the Alpine Schist, a relict foliation preserved inside a porphyroblast is probably inherited from this early (Jurassic) metamorphism. The garnet in the metachert of this research, from the Alpine Schist could be inherited wholly or at least partially, from this early episode. Mn-rich garnet-bearing cherts occur in the Otago Schist, where the high Mn contents in the precursor rocks stabilized garnet growth at relatively low temperatures (Mortimer, 2000).

Timing constraints for the growth of any such inherited garnet in the Alpine Schist remain elusive, and might possibly be closer to the Cretaceous ages for the main metamorphism of the Alpine Schist. The recent discovery of 108 Ma detrital zircons in an exposure of the highest grade (garnet-biotite-albite zone) Otago Schist, together with results of new (U-Th)/He ages of 99 Ma from zircon of that region (Mortimer *et al*., 2015) drastically reduces the amount of time available for the subduction, metamorphism and exhumation of the Otago Schist, with exhumation probably complete by 85−93 Ma. The main metamorphism of the Alpine Schist probably results from its collision with the Hikurangi basalt plateau in Cretaceous time. The available timing constraints for the growth of the main high grade minerals in the Alpine Schist indicate that this progressed sporadically, over as much as 30 Ma (Vry *et al*., 2004). Evidence for the metamorphic events are sometimes preserved within compositional zones of minerals. Compositional zones of a single garnet from the mylonite zone (Fig. 2.3) provides a Sm-Nd age of 97.8 ±8.1 Ma for the innermost core, Lu-Hf ages of 86.2±0.2 Ma and 86.3±0.2 Ma for the overlying zones, a step leach Sm-Nd age of 12 ±37Ma for the next overlying zone and a final rim age of 5−6 Ma (Vry *et al*., 2004). Ages for the amphibolite facies of the Alpine Schist that represent Cretaceous mineral growth have been obtained by U-Pb of 71 ± 2 Ma for monazite fractions from a Mataketake Range garnet biotite greyschist, and a Sm-Nd isochron age of 100 ± 12 Ma for titanite, garnet, hornblende, and whole rock fractions from the Haast River (Mortimer & Cooper, 2004). Pegmatites from the Mataketake Range provide ages of 68 ± 2.6 Ma based on U-Pb dates on monazite, and 67.9 ± 2.5 Ma from zircon SHRIMP ion-probe (Chamberlain *et al*., 1995). These

pegmatites have been metamorphosed and exhumed at a later age of 5 Ma (Chamberlain *et al*., 1995). Late Cenozoic oblique convergence of the Pacific and Australian plates has been estimated from sea floor spreading data at ~6 Ma (Walcott, 1998; Cande & Stock, 2004). A change in tectonics from a dominantly strike-slip to an obliquely convergent setting ensured the modern phase of mountain building forming the Southern Alps at 5–3 Ma (Walcott, 1998; Tippett & Kamp, 1993; Batt *et al*., 2000, 2004; Little *et al*., 2005).

SAMPLE INFORMATION

Table 2.2 provides sample information: sample number, degree of metamorphism, location and contained assemblage for the five cherts investigated in this research.

Table 2.2. Locations metamorphic zone and assemblage of metachert samples of the present research.

Sample No.	Location	PETLAB No.	VUW Number	Grid Reference No	Metamorphic Zone	Latitude/ Longitude:
J34[1]	Fox Glacier	P98245	VU 28666	(H35) 2270800 5741400	Garnet Zone	43.49833°S 170.04162°E
J35[1]	Moeraki River	P97527	VU 28062	(G37) 2226500 5701100	Garnet Zone	43.84518°S 169.47324°E
J36[1]	Hare Mare Stream	P97507	VU 28701	(H35) 2274400 5747600	Oligoclase Zone, mylonite zone	43.44371°S 170.08878°E
A12E[2]	Vine Creek	P85584	VU 37661	(J33) 23528 E 58040 N	Mylonite zone	42.9283° S 171.0301° E
AMS01[3]	Amethyst Tunnel, Hari Hari	P85581	VU 43156		Mylonite zone	43.157213° S, 170.629483° E

[1]The locations, mineralogy, and bulk chemical analyses of samples J34, J35 and J36 are presented in Grapes *et al*. (1985).
[2]A12E was collected by Andrea Pepper (Pepper, 2000).
[3]Sample AMS01 was collected by Stephen Keys.

Fernandes, J.

3. METHODS

THIN-SECTION PETROGRAPHY

Thin section microscopy is an indispensable tool for rock analyses (Raith *et al.*, 2012). Thin section petrography is the use of transmitted as well as reflected light microscopy to provide insight into the mineralogy of the rock that might not be immediately evident from a hand specimen. This method is a necessary precursor to more sophisticated high resolution analytical techniques.

The identification of minerals and documentation of textures in polished thin sections by digital imaging was initially made in the School of Geography, Environment and Earth Sciences (SGEES) at Victoria University of Wellington (VUW), New Zealand. The samples were cut into billets and submitted to the thin-section laboratory, SGEES, VUW for preparation into standard polished thin sections (Figure 3.1), 30µm thick. Billets of a cut perpendicular to the dominant foliation were made. The thin sections were made to show variation of compositional layering in the sample.
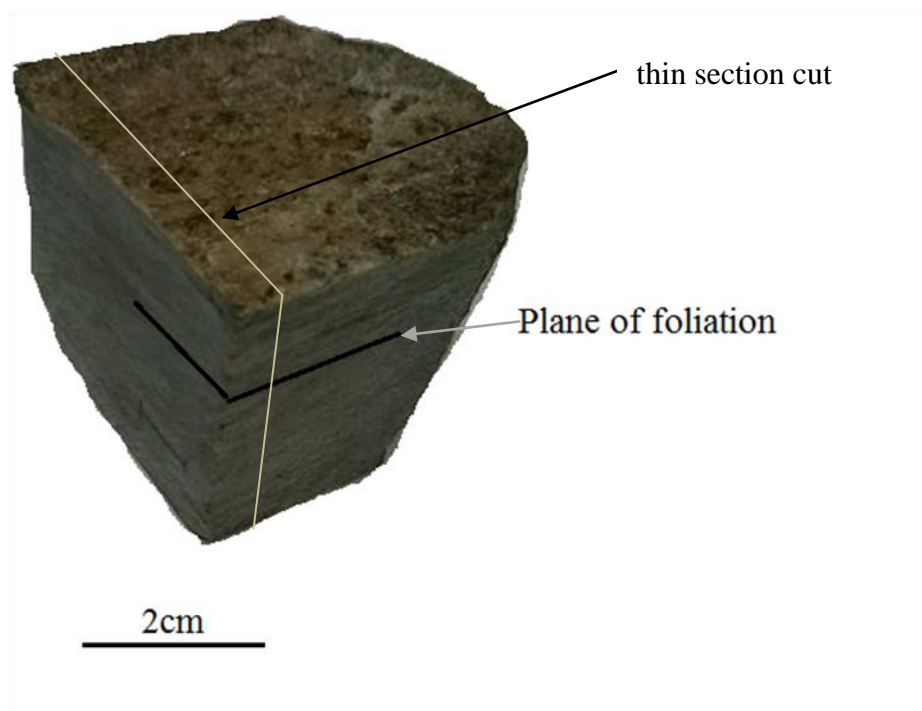
Figure 3.1. Metachert showing Thin-section cut for all samples.

The major minerals in the rocks along with their textures were documented, using transmitted and reflected light microscopy and plane- and cross-polarized illumination. Photomicrographs were used to document the characteristic or distinctive features of each thin section.

Subsequent textural and mineral composition information was obtained using μXRF-mapper and SEM methods at the Commonwealth Scientific and Industrial Research Organisation (CSIRO) Australian Resources Research Centre, Kensington, Perth, Australia, and by BSE imaging and EPMA compositional mapping using the EPMA at VUW. Information regarding these subsequent methods is provided below.

MICRO X-RAY FLUORESCENCE (μXRF) MAPPING

Micro XRF is a high-resolution method for non-destructive elemental analysis that can be used for a diverse range of rocks. Micro XRF uses the unique radiation signature obtained on interaction between electron beams and the sample. Exposure of a mineral to high energy radiation causes excitation and dislodges an electron from the inner shell. This electron may be replaced by an electron from the outer shell. This causes a release of energy in the form of low energy X-rays called fluorescent radiation. The emitted radiation is unique to the transition between electron orbits. Hence, X-ray fluorescent radiation is used for chemical analysis of a rock. Micro XRF maps of polished thin sections were obtained using the μXRF equipment, at the Australian Resources Research Centre, Perth, Australia, by my research supervisors, Dr. Julie Vry and Dr. Michael Gazley. The Bruker spectrometer is a state of the art μXRF device (von Bohlen, 2009). The Bruker M4 Tornado X-ray fluorescence mapper uses an Rh tube X-ray source. An analytical spot size of 25 μm and a step size of 25 μm was used. A map is produced by moving the sample beneath a stationary beam. At each point a full X-ray spectrum is recorded and can then be deconvoluted to give elemental concentrations. Detection limits vary from ppm levels for transition series metals to fractions of a weight percent for light (Mg and Al) and heavy elements. Datasets collected using the Tornado were processed with the M4 TORNADO software ESPRIT, based on a modification of the Sherman equation. The Bruker software uses matrix effects to improve accuracy (Bruker, 2015).

Fernandes, J.

SCANNING ELECTRON MICROSCOPE (SEM) MAPPING

The SEM is a state of the art non-destructive instrument with a high image resolution of 1−2 μm, magnification ranging from 20X to approximately 30,000X and spatial resolution of 50 to 100 nm. Chemical compositions are obtained using Oxford Instruments X-Max EDS (energy dispersive spectrometer) detector. Interaction between electron beam and the sample produces characteristic high energy signals such as secondary electrons producing SEM images, backscattered electrons (BSE), photons that have characteristic X-rays used for elemental analysis. The signals provide elemental, crystallographic, textural information about the rock.

A MIRA3 TESCAN SEM with an Oxford Instrument X-MaxN detector was used to make Energy dispersive spectrometry (EDS) composition maps at the Australian Resources Research Centre, Perth, Australia. The SEM composition maps were obtained by my research supervisors Dr. Julie Vry and Dr. Michael Gazley. The typical operating conditions used an accelerating voltage of 15 kV, 5 nA beam current, and a <1 μm beam diameter. The datasets collected using the TESCAN were processed using Oxford AZtec software.

WHOLE ROCK ANALYSES

The whole rock analyses provide the initial basic input information for calculations of $P-T$ pseudosections, which are essential to studies that use the forward modelling approach to study metamorphism.

The rock samples A12E and AMS01 were crushed to powder at Victoria University of Wellington using a TEMA tungsten carbide mill. Major and minor element whole rock analyses for the garnet cherts were conducted by Australian Laboratory Services Pty. Ltd. using X-Ray fluorescence spectrometry (XRF). Whole rock data for samples J34, J35 and J36 were obtained from Grapes *et al*., 1985. For the THERMOCALC calculations described below, the wt% oxide data was converted to mole percent (mol %). Minor amounts of BaO (< 0.06), Cr_2O_3 (< 0.01), SrO (<0.01), P_2O_5 (0.02 wt %) and trace elements were disregarded from the calculation. Apatite ($Ca_5(PO_4)_3(F,Cl,OH)$) was excluded by proportionately removing Ca and P_2O_5 from the bulk composition. Table 4.0 shows wt % and corresponding mol % for each

Fernandes, J.

sampled garnet chert. The XRF data for representative samples of garnet chert were corrected for LOI and presented as wt % oxide.

K-MN-NA TERNARY PLOT

Reflex ioGAS is software for chemical analysis that enables detection of patterns, anomalies and relationships in large geochemical datasets. Three end member compositions K, Mn and Na have been plotted using ioGAS™ data analysis software to show variation in the chemistry of garnet cherts and how it affects the stability of phases in pseudosection.

ELECTRON PROBE MICRO-ANALYSIS

The fraction of electrons backscattered varies with atomic number (Z) of the mineral being analysed. The higher the mineral density, more extensive is the backscattering of electrons. Hence highly dense minerals (e.g. Fe-Ti oxides) with high Z appear bright in a BSE image, whereas light minerals (e.g. quartz) appear dark. For quantitative analyses the EPMA uses the same principle as XRF and SEM, where the atoms in the sample are excited by a high energy source that liberate electrons from the inner shell. Electrons from the outer shell move to the inner shell and emit X-rays characteristic of the element under analysis.

Mineral analyses and associated imaging of minerals in the garnet metacherts were obtained using the JEOL JXA-8230 Superprobe that is housed in the SGEES at VUW. Analysed sites were located and documented using backscattered electron (BSE) images from the EPMA in combination with photomicrographs and µXRF maps. Operating conditions for while obtaining BSE images were 8.01nA and 15.0kV, and during transect runs were 15kV and 12nA with a 1µ spot size. Energy dispersive spectrometry was used initially to identify the mineral assemblage by spot analysis which produces a compositional spectrum of the phases present. Locations of textural interest were imaged and qualitative analyses for mineral identifications were made. On imaging in EDS the image location can be saved, stored and retrieved. Using quantitative wavelength dispersive spectrometry (WDS), transects were run across garnets that were chosen representing rock conditions within bands of different texture and composition. To enable corrections for drift, standards of known composition were run between transects. Details of the two garnet standards a

Fe-rich almandine and a Mg-rich garnet Kakanui pyrope are presented in the table below.

Table 3.1. Compositions of garnet EPMA standards.

oxide wt%

Almandine	Kakanui pyrope
SiO_2 - 35.84	SiO_2 - 41.46
Al_2O_3 - 21.2	Al_2O_3 - 23.73
TiO_2 - n.a.	TiO_2 - 0.47
MgO - 1.04	MgO - 18.53
FeO(calc) - 27.84	FeO(calc) -10.68
Fe_2O_3(calc) - 0.28	MnO - 0.26
MnO - 14.33	CaO - 5.17
CaO - 0.286	NiO - 0.01
Cr_2O_3 - 0.00	
Total - 100.816	Total - 100.31

Details of the pyrope standard can also be retrieved from:
http://cub.geoloweb.ch/index.php?page=std_info&id=21

THERMODYNAMIC FORWARD MODELLING

P-T PSEUDOSECTIONS

THERMOCALC is a computer program created by Powell and Holland (1988). THERMOCALC uses the solution of non-linear equations to calculate phase equilibria and is a powerful program for pseudosection construction because it can optimise calculations for a particular rock bulk composition or sample. It requires *a-x* models appropriate to the sample, a dataset and bulk composition of the equilibrated metamorphic rock. It is capable of producing petrogenetic grids for a system showing all the reactions in that system and *P–T, P–x* and *T–x* pseudosections for a specific bulk composition in a rock. Drawpd is a THERMOCALC tool that plots the calculations on a set of axes (*P–T, P–x, T–x*) creating a pseudosection. Automated contouring of pseudosections for mineral mode and compositions are created using TCInvestigator, a new graphical interface for THERMOCALC developed Dr Michael Gazley and his colleagues at CSIRO (Pearce *et al*., 2015).

The pseudosections for four of the samples were calculated in the eleven-component system MnNCKFMASHTO (MnO, Na_2O, CaO, K_2O, FeO, MgO, Al_2O_3, SiO_2, H_2O, TiO_2, O) using the thermodynamic dataset 6.2 (ds62) (Holland & Powell, 1998). The fifth one, J35 contains amphibole that is not yet implemented in the latest THERMOCALC dataset and *a-x* models. For this reason, the *P–T* pseudosection for J35 was calculated in a ten-component system MnNCFMASHTO, K-free with the thermodynamic dataset ds55s and it's *a–x* models for amphibole. THERMOCALC input is calculated from the whole rock compositions by converting weight% oxide to mol% the XRF data was converted into mol % oxide for input into THERMOCALC.

Pseudosections for all samples were calculated using THERMOCALC v. 3.40 (Powell & Holland, 1988) as downloaded in May, 2014 from the THERMOCALC website http://www.metamorph.geo.uni-mainz.de/thermocalc/ (Powell & Holland, 2009). The cherts being Mn-rich rocks have been modelled using the latest internally consistent *a-x* models for Mn bearing rocks (White *et al*., 2014). J35 was calculated in a K-free system using the older database ds55 and its *a-x* models for amphiboles.

Fernandes, J.

4. RESULTS AND INTERPRETATIONS

WHOLE ROCK ANALYSES

Whole rock analyses for five garnet chert samples from the Alpine Schist of New Zealand are presented in Table 4.0.

Table 4.0. Garnet chert bulk rock compositions* and as input for THERMOCALC $P-T$ pseudosection calculations.

	J34 28666	TC	J36 28701	TC	A12E 37661	TC	J35 26062	TC	AMS 01	TC
	wt. %	mol. %	wt. %	mol. %	wt. %	mol. %	wt. %	mol. %	wt. %	mol. %
SiO$_2$	89.81	92.87	85.40	89.23	89.9	92.48	48.83	52.98	90.4	93.61
TiO$_2$	0.17	0.13	0.47	0.37	0.18	0.14	0.39	0.32	0.13	0.10
Al$_2$O$_3$	3.44	2.10	5.05	3.11	3.97	2.41	8.01	5.11	3.13	1.91
Fe$_2$O$_3$	0.18	-	0.13	-	1.61	-	13.29	-	1.47	-
FeO	1.64	1.56	2.71	2.47	1.24	1.25	11.98	21.65	0.94	1.15
MnO	0.88	0.77	1.68	1.49	0.64	0.56	7.25	6.65	0.88	0.77
MgO	1.00	1.54	1.37	2.13	1.06	1.62	1.37	2.21	0.69	1.06
CaO	0.62	0.61	0.92	0.87	0.54	0.57	5.16	5.63	0.63	0.67
P$_2$O$_5$**	0.05	-	0.11	-	0.02	-	0.96	-	0.02	-
Na$_2$O	0.03	0.03	0.03	0.03	0.53	0.53	0.04	0.04	0.42	0.42
K$_2$O	0.59	0.39	0.46	0.31	0.68	0.45	0.01	-	0.46	0.30
O	-	0.035	-	0.026	-	0.045	-	5.41	-	0.084
LOI	0.64		0.62		0.49		0.97		0.27	
Total	99.05		98.95		99.77		98.26		98.63	

 * Samples J34, J35 and J36 are from Grapes *et al*. (1985). AMS01 and A12E were analysed at Australian Laboratory Services Pty Ltd.
**All P and proportionate amounts of Ca removed as apatite.
LOI = loss on ignition.
 TC = recalculated analysis, apatite free and in mol%

Fernandes, J.

5K₂O-MnO-10Na₂O TERNARY PLOT
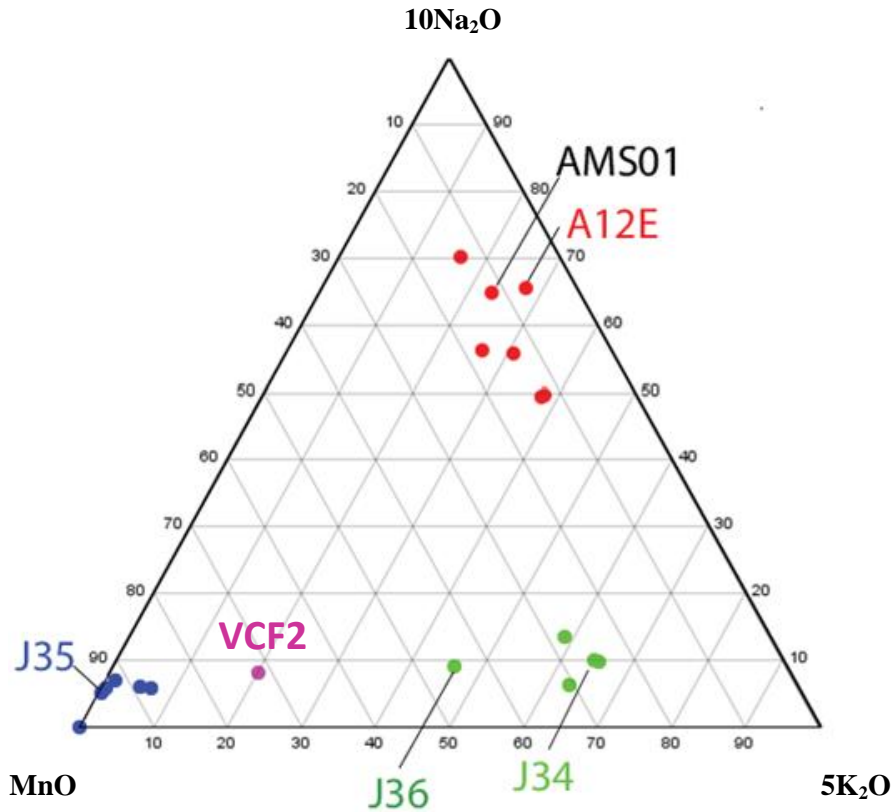
Figure 4.0. Ternary plot of 5K₂O-MnO-10Na₂O from seventeen Alpine Schist garnet chert samples. They have been calculated as SiO₂ free mol% compositions.

The five samples for which the whole rock data is presented in Table. 4.0 were chosen from a larger data set; the data used in the ternary plot is presented in Appendix 1. The compositions of all the samples were plotted in the ternary plot (Fig. 4.0), to make compositional comparisons between the samples. The green dot cluster represents rocks with proportionately high K, red represents high Na and blue has high Mn. The pink isolated dot (Sample VCF 2) has an intermediate composition between the high Mn and high K samples. Na₂O and K₂O have been multiplied by ten and five respectively to increase separation between clusters on the plot.

All abbreviations follow the recommendations of Kretz (1983).

Fernandes, J.

SAMPLE J34 (28666)

RESULTS

Mineral assemblages and textures

Thin-section petrography

The rock is made up of thin, alternating quartz and garnet-rich layers, and consists of fine-grained quartz, garnet, white mica and biotite, with minor chlorite, apatite, rutile and carbonate. The abundance and size of garnet and quartz vary from layer to layer. Garnet-poor layers contain a few, relatively large euhedral garnets (30−70 µm diameter), while more garnet-rich layers contain abundant small subhedral garnets (~5−35 µm diameter). In thin section, the large garnets have brownish cores and paler rims, and typically contain tiny colourless inclusions with low birefringence (probably quartz or apatite) in their cores. The small garnets are not visibly zoned. Representative photomicrographs of this sample are presented in Figures 4.1a–h. The sheet silicates are concentrated in the garnet-rich layers, and define a foliation that is aligned with the compositional layering. Quartz ranges in size from ~200−700 µm, with the largest grain dimension parallel to the foliation direction. The flakes of mica are <2 mm in their largest dimension, with the more abundant biotite forming thicker books ($<$ 40 µm thick) than the white mica ($<$ 15 µm). The white mica is probably muscovite (K-rich white mica), but in such fine-grained rocks, other white micas such as paragonite (Na-rich white mica) cannot be ruled out by optical petrography alone. Small shear bands (e.g. diagonal brown trace, Fig. 4.1a) offset the compositional banding and indicate the direction of extension which is horizontal in the orientation of the thin section.
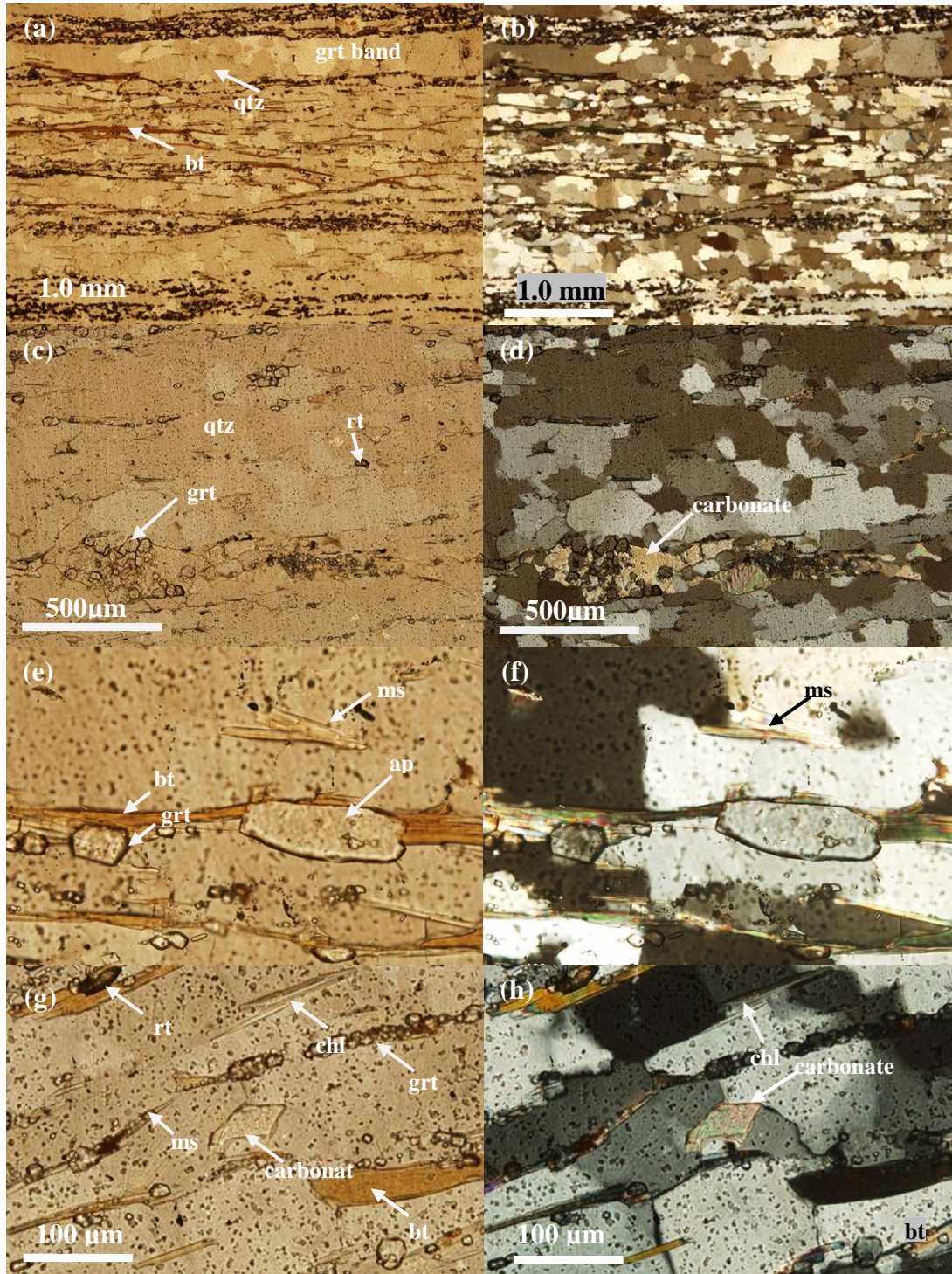
Figure 4.1. Representative photomicrographs of sample J34 (panels a, c, e, g: plane-polarised illumination; panels b, d, f, h: cross-polarized illumination). Panels a & b show garnet-rich and quartz-rich layers, the fine grain size of garnet porphyroblasts, and offsetting of the layering by an extensional shear band. Close-up views in panels c–h show details of the mineralogy.

Fernandes, J.

Micro X-ray fluorescence composition maps

The µXRF maps (Fig. 4.2) show the distribution of elements in the rock at the thin-section scale. When used in conjunction with indicative mineral formulae for the commonly encountered minerals in these rocks (Table 4.1), these maps also can be used to show the distributions of minerals. The results obtained are consistent with, and reinforce, the petrographic observations described above.
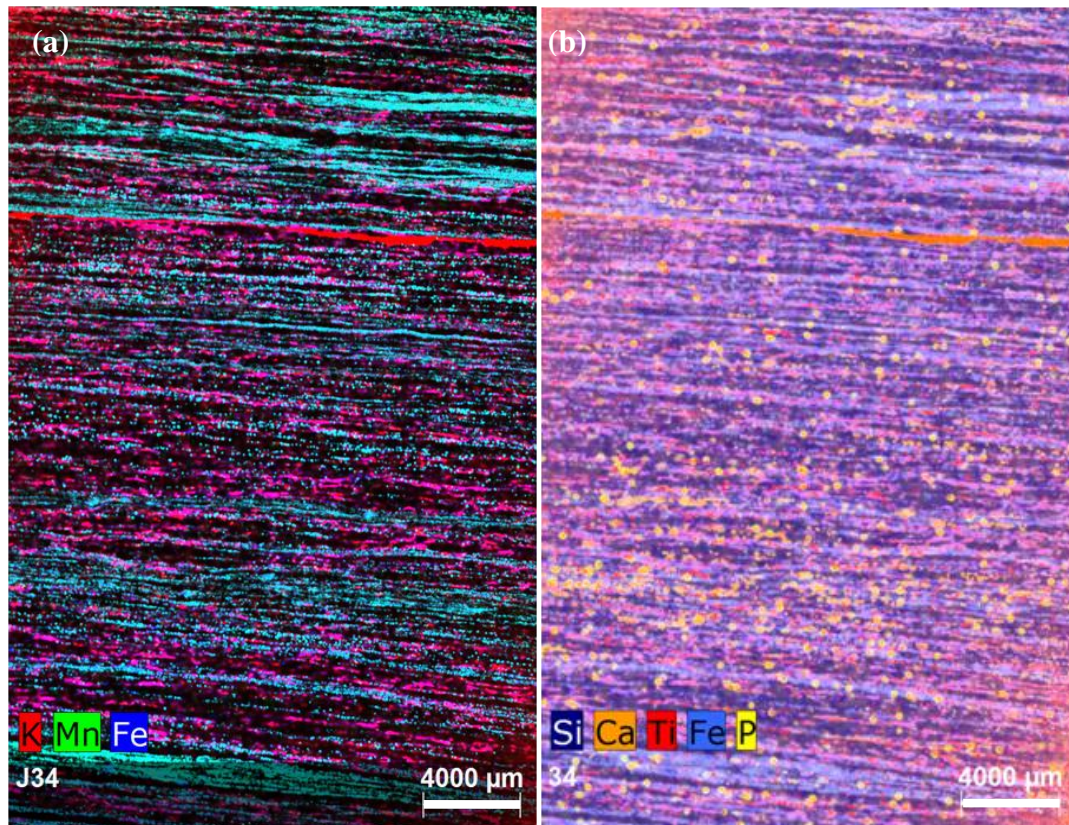
Figure 4.2. The µXRF maps show fine-scale compositional layering in J34. a) Shows Mn-rich garnet layers (pale blue) and K-rich mica bands (dark pink). b) Shows quartz layers (dark blue), rutile (red), and apatite (yellow). Carbonate (light orange, panel b) is associated with the compositional layering, in amounts that vary throughout the slide. The orange band near the top of panel b is a glue filled crack in the thin section.

Table 4.1. Mineral formulae.

Silicates
Albite $NaAlSi_3O_8$
Biotite $K(Mg,Fe)_3(AlSi_3)O_{10}(F,OH)_2$
Chlorite $(Mg,Al,Fe)_6(Si,Al)_4O_{10}(OH)_8$
Epidote $Ca_2(Al,Fe)_2(SiO4)_3(OH)$
Garnet $(Ca,Mn,Mg,Fe)_3Al_2Si_3O_{12}$
Margarite $CaAl_2(Al_2Si_2)O_{10}(OH)_2$
Muscovite $KAl_2(AlSi_3)O_{10}(OH)_2$
Paragonite $NaAl_2(AlSi_3)O_{10}(OH)_2$
Quartz SiO_2
Tourmaline $(Na,Ca)(Mg,Li,Al,Fe^{2+})_3Al_6(BO_3)_3Si_6O_{18}(OH)_4$

Sulphides
Chalcopyrite $CuFeS_2$
Pyrite FeS_2

Oxides
Magnetite Fe_3O_4
Haematite Fe_2O_3
Rutile TiO_2
Ilmenite $FeTiO_3$

Carbonates
Calcite $Ca(CO_3)$
Dolomite $CaMg(CO_3)_2$
Ankerite $Ca(Fe,Mg,Mn)(CO_3)_2$

Phosphate
Apatite $Ca_5(PO_4)_3(OH,F,Cl)$

Fernandes, J.

Scanning Electron Microscopy-based composition maps

Representative EDS element distribution maps are presented in Fig. 4.3 below.

Fig. 4.3 (cont'd.)

Fernandes, J.
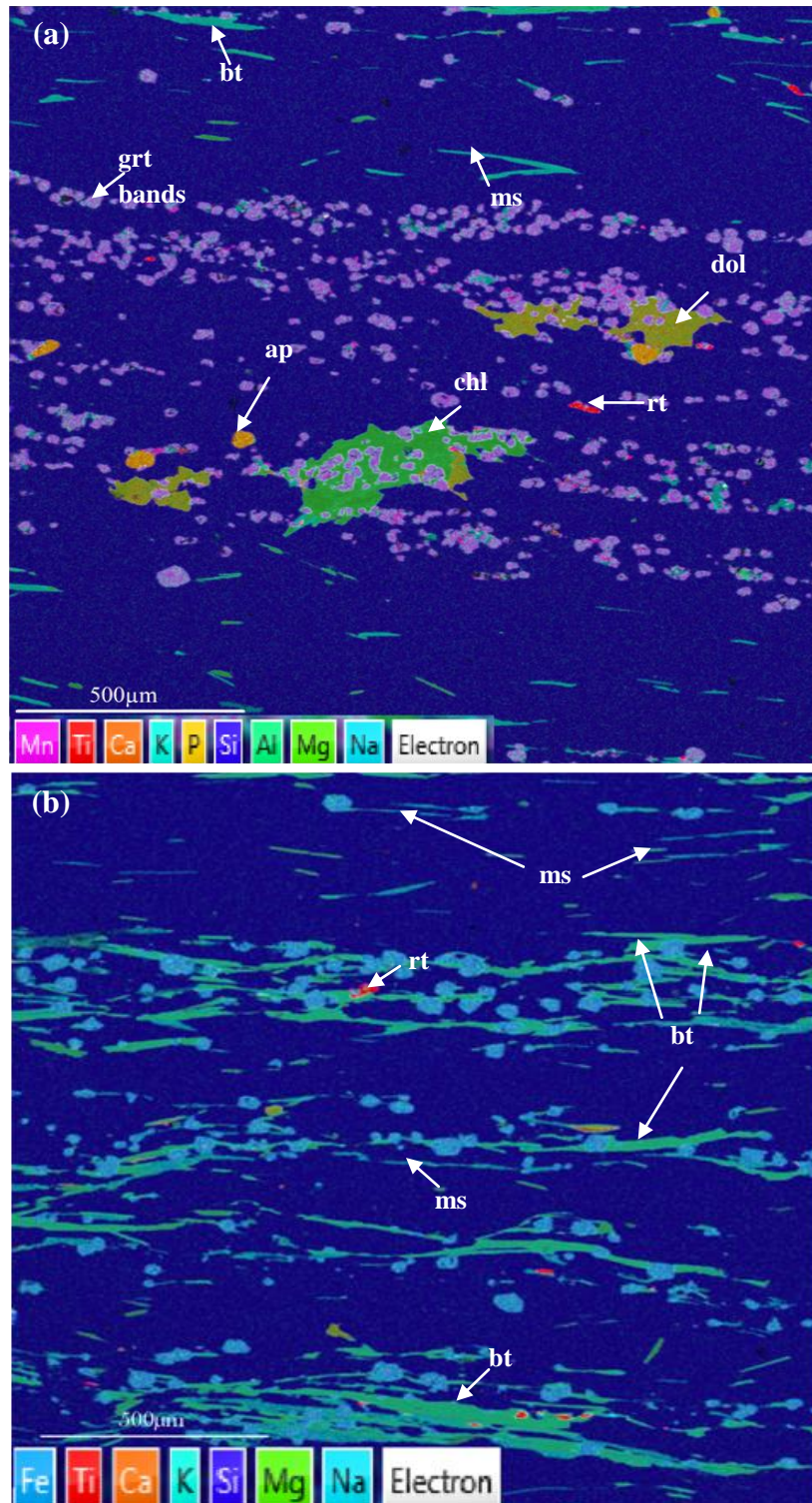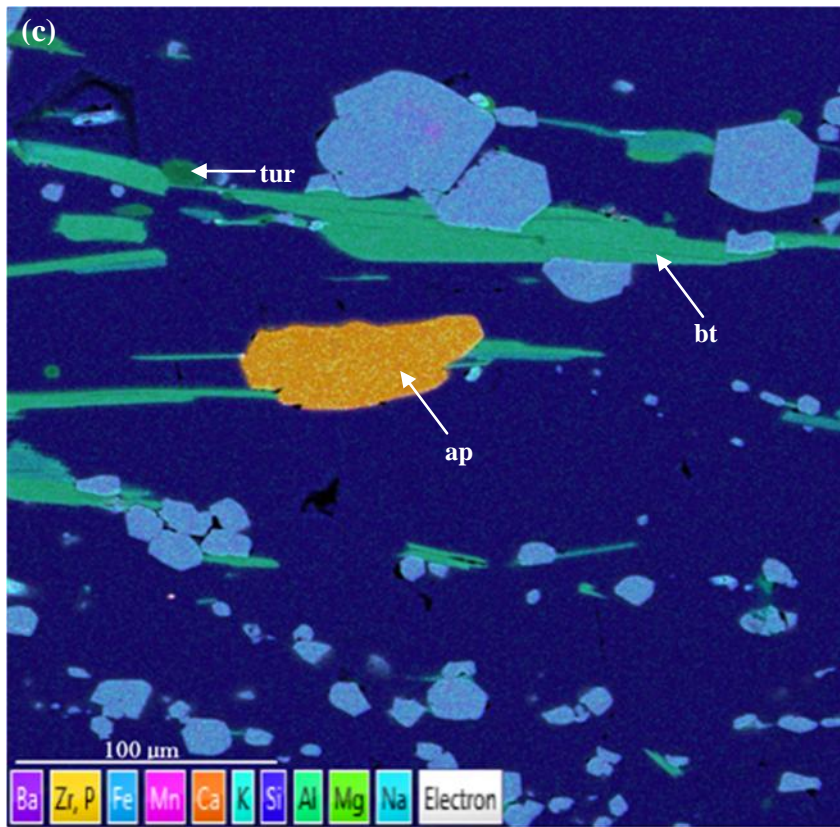
Figure 4.3. SEM-based composition maps of sample J34. Panel a) and b) show compositional layering of quartz (dark blue) and garnet bands (pink), with mica (shades of green) associated with the garnet bands. c) Close-up view showing the assemblage present.

The maps provide a more detailed visual record of mineral chemistry and mineral compositional zoning than the µXRF maps. These results confirm and support information gained from the thin-section and µXRF studies. For example, the EDS map (Fig. 4.3a) shows that the carbonate in this thin section is rich in both Ca and Mg; therefore, it is dolomite.

In addition to the quartz and garnet layering, panel a) and b) show micas−biotite (bright green) with lesser amount of muscovite (pale green), dolomite (yellow-green), apatite (orange), and rutile (red) and an atypical large clot of chlorite (bright green) − most chlorite occurs as disseminated flakes in the rock. Abundant quartz (dark blue) with garnet (pale blue), biotite (green) that is aligned to form the foliation, minor apatite (orange) porphyroblasts and small porphyroblasts of accessory tourmaline are shown in panel c).

Fernandes, J.

Electron Probe Micro-Analysis (EPMA)

Figure 4.4a show backscattered electron (BSE) images of representative garnet in a thin section of sample J34, and the locations of analytical transects across the imaged garnet.

Background colour changes on the garnet composition transect (Fig. 4.4b–d) show where changes in brightness occur in the BSE images. The brightness variations in the BSE images reflect differences in the overall atomic number, such that higher brightness levels are associated with heavy elements.

Figure 4.4b–d show the mole fractions of spessartine (X_{sps}), almandine (X_{alm}), grossular (X_{grs}) and pyrope (X_{pyp}), and the Fe-number $(x(g))$. They are defined as:

$X_{sps} = \text{Mn}/(\text{Fe}_{total} + \text{Mg} + \text{Ca} + \text{Mn})$,

$X_{alm} = \text{Fe}_{total}/(\text{Fe}_{total} + \text{Mg} + \text{Ca} + \text{Mn})$,

$X_{grs} = \text{Ca}/(\text{Fe}_{total} + \text{Mg} + \text{Ca} + \text{Mn})$,

$X_{pyp} = \text{Mg}/(\text{Fe}_{total} + \text{Mg} + \text{Ca} + \text{Mn})$, and

$x(g) = \text{Fe}_{total}/(\text{Fe}_{total} + \text{Mg})$ on a molar basis.

Fernandes, J.
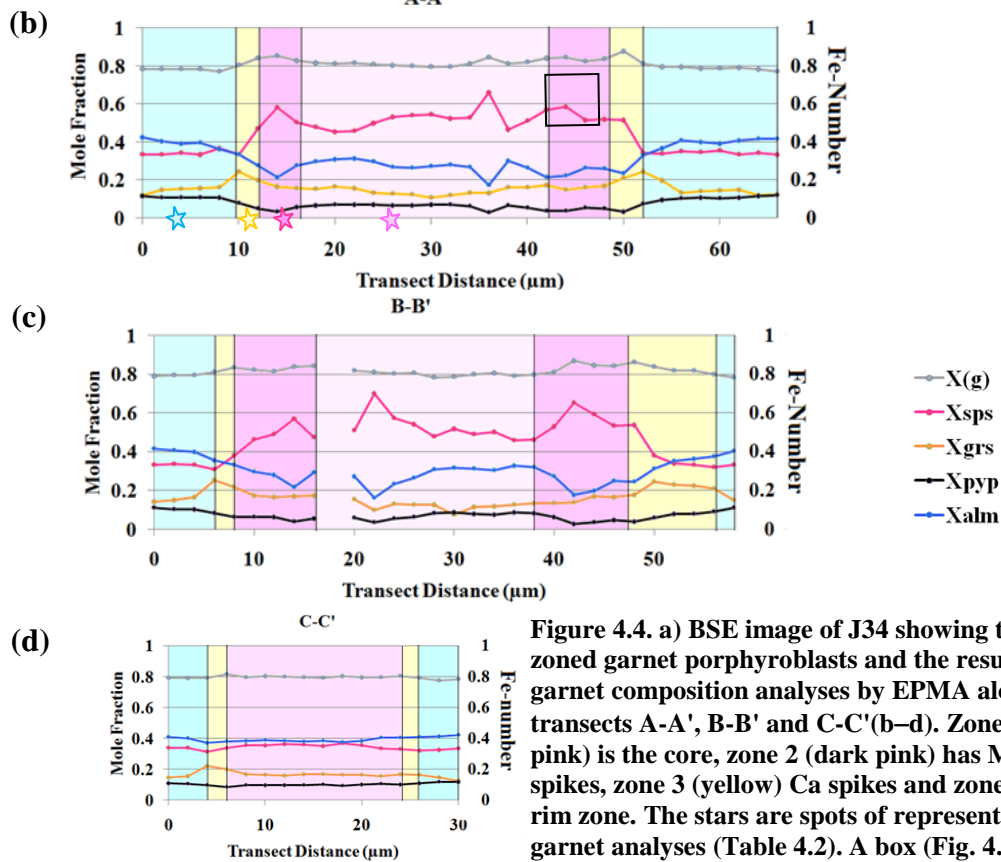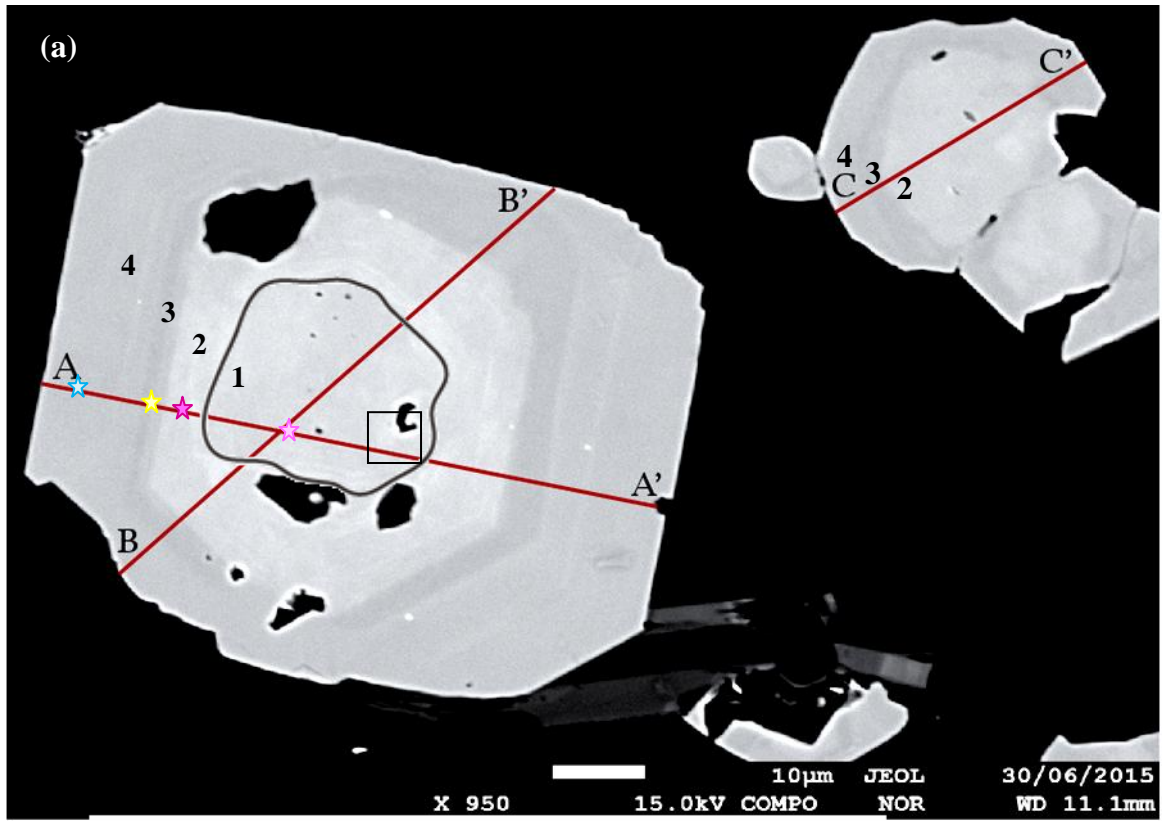
Figure 4.4. a) BSE image of J34 showing two zoned garnet porphyroblasts and the results of garnet composition analyses by EPMA along transects A-A', B-B' and C-C'(b–d). Zone 1 (light pink) is the core, zone 2 (dark pink) has Mn spikes, zone 3 (yellow) Ca spikes and zone 4 (blue) rim zone. The stars are spots of representative garnet analyses (Table 4.2). A box (Fig. 4.4a) is drawn around a bright spot in the core corresponding to the Mn-spike boxed in Fig. 4.4b.

The BSE image (Fig. 4.4a) shows that the garnets in sample J34 are compositionally zoned. The deep interior garnet growth zones are not exposed in every garnet slice, or some garnets do not preserve the inner zones. The most complete compositional zoning record is apparent in the largest garnet in Fig. 4.4a. The garnet in the BSE image has been divided into zones and numbered, based on greyscale brightness differences that reflect compositional changes. These zones (Fig. 4.4a) are therefore linked to the changing trends (Fig. 4.4b–d) in the garnet chemistry. The inmost core, zone 1 (pale pink, Fig.4.4b–c) contains a few scattered tiny inclusions and has an irregular margin along which quartz inclusions occur. Overlying zone 1 is a brighter zone 2 (dark pink, Fig. 4.4b–d) of irregular shape and thickness. The two zones are texturally discontinuous; there is no smooth transition to the brighter zone (2) but instead what appears to be a corrosion of the inmost core (1) boundary. Subsequent overgrowths (3–4) are more euhedral in form and show well-developed compositional zoning that is marked by sharp transitions to dark (3, yellow in Fig. 4.4b–d) and then medium-grey (4, blue in Fig. 4.4b–d) in the BSE image. The bright zone (2) is overgrown by a narrow dark zone (3), which is overgrown by the outermost zone (4). The outermost zone of the garnet tends to be thicker in the foliation direction, and thinner perpendicular to it. Quartz inclusions occur in the outer part of the bright zone (2) and in the narrow overlying dark zone (3), but not in the pale grey garnet rim. The compositional transects across the large garnet show the inner core (zone 1), where $X_{sps} \approx 0.45$–0.66, $X_{alm} \approx 0.28$, $X_{grs} \approx 0.13$; zone 2 has $X_{sps} \approx 0.34$–0.65, $X_{alm} \approx 0.30$, $X_{grs} \approx 0.16$; zone 3 has $X_{sps} \approx 0.36$, $X_{alm} \approx 0.35$, $X_{grs} \approx 0.21$; and zone 4 has $X_{sps} \approx 0.34$, $X_{alm} \approx 0.40$, $X_{grs} \approx 0.15$.

Overall, the garnet composition transects are bell-shaped (Hollister, 1966), with high Mn (expressed here as X_{sps}) in the cores, and low Mn in the rims. The cores have minor local variations of X_{sps} and corresponding changes in X_{alm} and X_{grs}. The Mn-spike in the core for transect A-A' (Fig. 4.4b) lines up with a light spot associated with the quartz inclusion which is right above the A-A' transect at 36 µm (boxed). For the core Mn-spike in transect B-B', there does not appear to be any light spot in the core that corresponds to this peak. With the exception of this, all the Mn-peaks correspond well to the bright zones in the BSE images. The bell-shaped overall pattern is interrupted by a local spike in X_{sps} and an associated

decrease in the X_{grs}, in zone 2. This correlates with a brighter zone in the BSE image, in areas immediately overlying the irregular and possibly corroded margin of the underlying garnet core (zone 1). Exterior to this, the X_{sps} content decreases sharply through zone 3, as the X_{grs} content increases. The persistent Ca spike $X_{grs} \approx$ 0.20–0.24 that occurs in zone 3 corresponds to a drop in the X_{sps} content. The X_{sps} and X_{grs} contents of the garnet stabilize in the outer parts of the garnet (zone 4).

Table 4.2. Representative EPMA garnet compositions for J34.

Oxide wt.%	Rim		Core	
	☆ Zone 4	☆Zone3	★Zone2	☆ Zone1
SiO_2	37.37	37.50	36.32	36.09
Al_2O_3	21.51	21.19	19.73	20.37
TiO_2	0.03	0.05	0.08	0.16
MgO	2.72	2.06	0.94	1.83
FeO_{total}	17.53	15.11	9.86	13.80
MnO	15.22	14.91	26.44	22.77
CaO	5.41	8.60	5.90	4.82
Cr_2O_3	0.00	0.03	0.04	0.00
Total	99.82	99.48	99.31	99.85
Normalised to 8 cations				
Si	2.984	2.997	2.964	2.918
Al	2.026	1.996	1.898	1.942
Ti	0.002	0.003	0.005	0.010
Mg	0.324	0.245	0.114	0.221
Fe_{total}	1.171	1.010	0.673	0.933
Mn	1.030	1.010	1.828	1.559
Ca	0.463	0.737	0.516	0.418
Cr	0.000	0.002	0.002	0.00
$x(g)$ =Fe/(Fe+Mg)	0.78	0.80	0.86	0.80
$m(g)=X_{sps}$	0.35	0.34	0.58	0.49
$z(g)=X_{grs}$	0.15	0.25	0.17	0.13
X_{pyp}	0.11	0.08	0.04	0.07
X_{alm}	0.39	0.34	0.22	0.31

Core content (zone 1): x(g) = 0.80, m(g) = 0.49, z(g) = 0.13 used later in Figs. 4.8a and 4.10a.
Rim content (zone 4): x(g) = 0.78, m(g) = 0.35, z(g) = 0.15 used later in Figs. 4.8b and 4.10b.
The stars correspond to Fig. 4.4a transect A-A'.

Fernandes, J.

The stars in Table 4.2 match the coloured stars on transect A-A', Fig. 4.4a. The next section combines measured mineral chemistry with $P-T$ pseudosections to provide a starting point to understand the metamorphic conditions the rock was subjected to.

Only the outer three growth zones are apparent (on the basis of brightness in the BSE image) in the exposed cuts of the smaller garnets (Fig. 4.4a). The compositional trends of the small garnet, in zones 2, 3 and 4 match the large garnet with a minor X_{grs} spike at 5 µm (zone 3) and compositional content $X_{sps} \approx 0.30$, $X_{alm} \approx 0.40$, $X_{grs} \approx 0.16$. Zone 2 is in the small and large garnet. The large and small garnet show dissimilar compositional trends (an effect of the slice of that garnet or may record a different part of the history) but have similar brightness in the BSE image.

Petrographic Forward Modelling

P−T pseudosection

The observed mineral assemblage in J34 is quartz, garnet, biotite, muscovite and chlorite with minor apatite, rutile and dolomite. An initial $P-T$ pseudosection (Fig. 4.5) for J34 was calculated based on the bulk rock composition and an assumption that the coexisting metamorphic fluid was pure H_2O, ignoring the carbonate (dolomite). This was done to provide a starting point for more appropriate pseudosection calculations involving a mixed H_2O-CO_2 fluid, as required by the presence of dolomite, and for considering the effects of variations in XCO_2. The pseudosection provides a broad constraint on the peak $P-T$ conditions > 5.5 kbar and 480−620°C in the absence of margarite (not identified), for a rock of this bulk composition metamorphosed in the presence of a pure H_2O fluid.

Fernandes, J.

Input bulk composition (mol %)

$SiO_2 = 92.87$, $TiO_2 = 0.13$, $Al_2O_3 = 2.10$, $FeO = 1.56$, $MnO = 0.77$, $MgO = 1.54$, $CaO = 0.61$, $Na_2O = 0.03$, $K_2O = 0.39$, $O = 0.035$.

J34 - All fields contain q and H2O
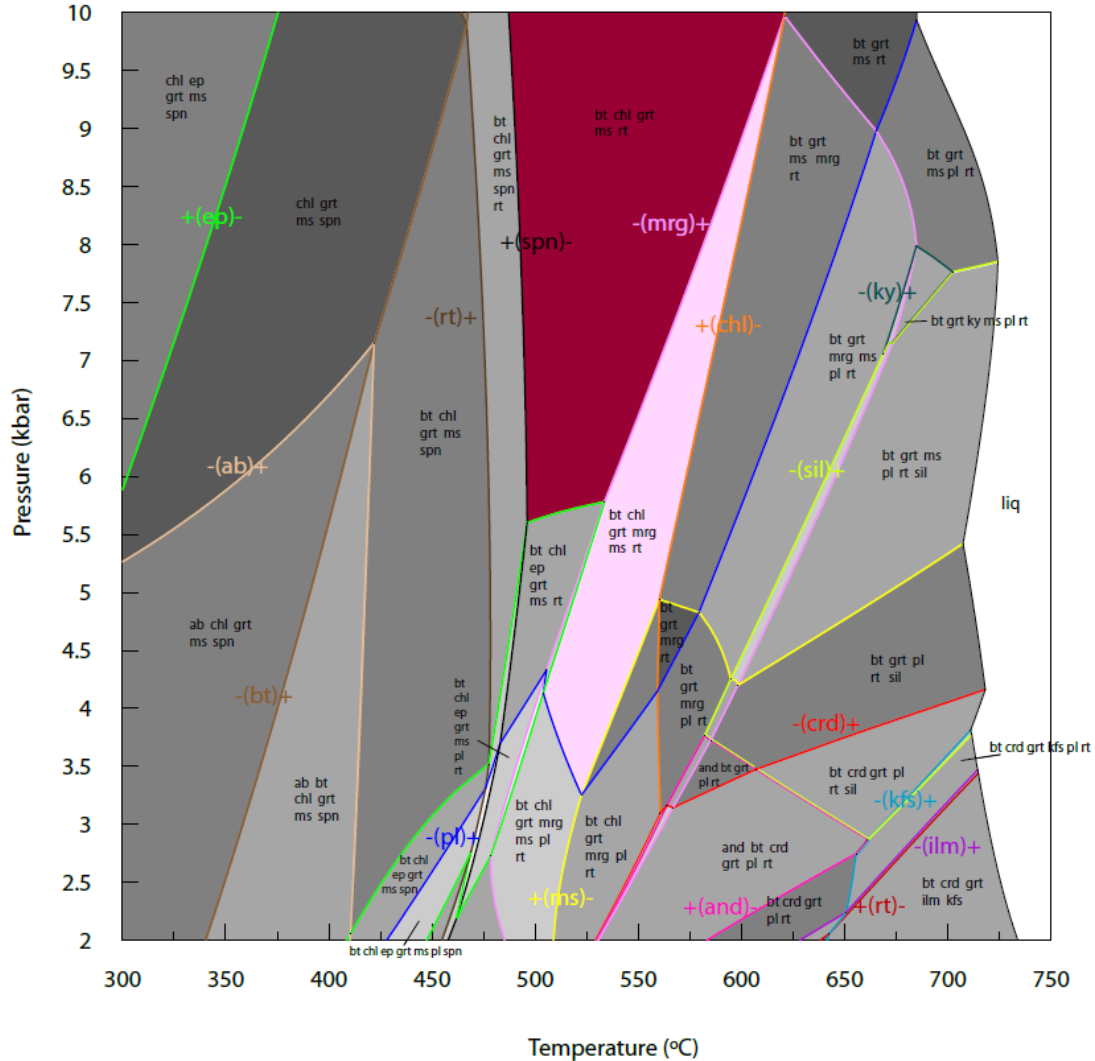
Figure 4.5. Initial *P–T* pseudosection results for J34, calculated for *X*H₂O = 1.0, using THERMOCALC. Dolomite (present in the rock) requires a mixed H₂O-CO₂ fluid, so cannot be shown here. Coloured fields show initial calculated *P-T* conditions for the remaining peak metamorphic assemblage bt+chl+grt+ms+rt+qtz (red), ± margarite (pink).

The pseudosections calculated in this study have coloured zero mode lines specific to the phase, forming field boundaries. These lines represent an incoming or outgoing phase, as demarcated by the + and − signs respectively.

Fernandes, J.

Contoured sections for the pure H₂O system

Fig. 4.6 shows contoured pseudosections for garnet mode, X_{sps}, $x(g)$ and X_{grs} produced using TCInvestigator v1.02 (Pearce *et al.*, 2015).

Fig. 4.6 (cont'd.)

Fernandes, J.

(c) *x(g)*
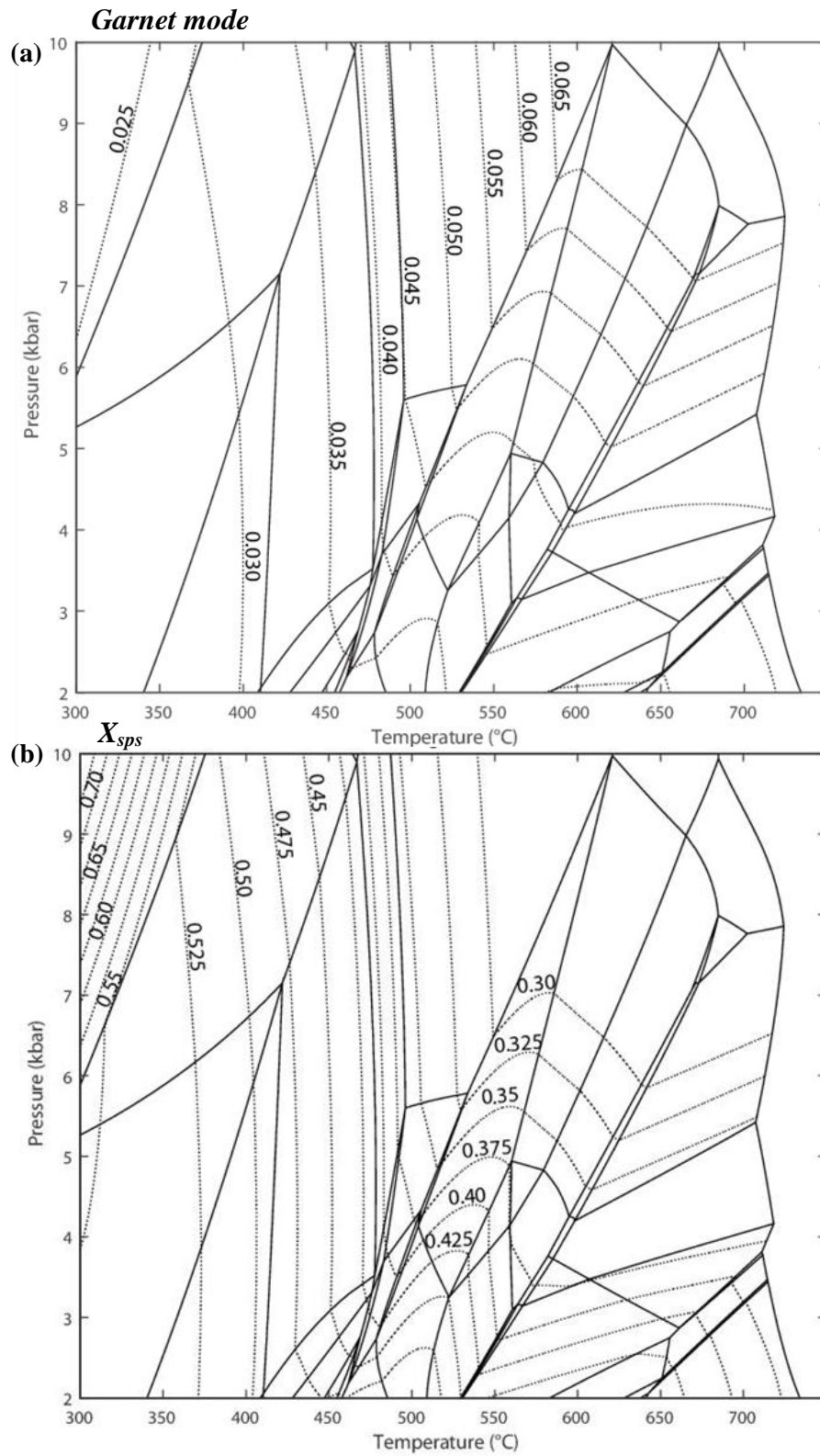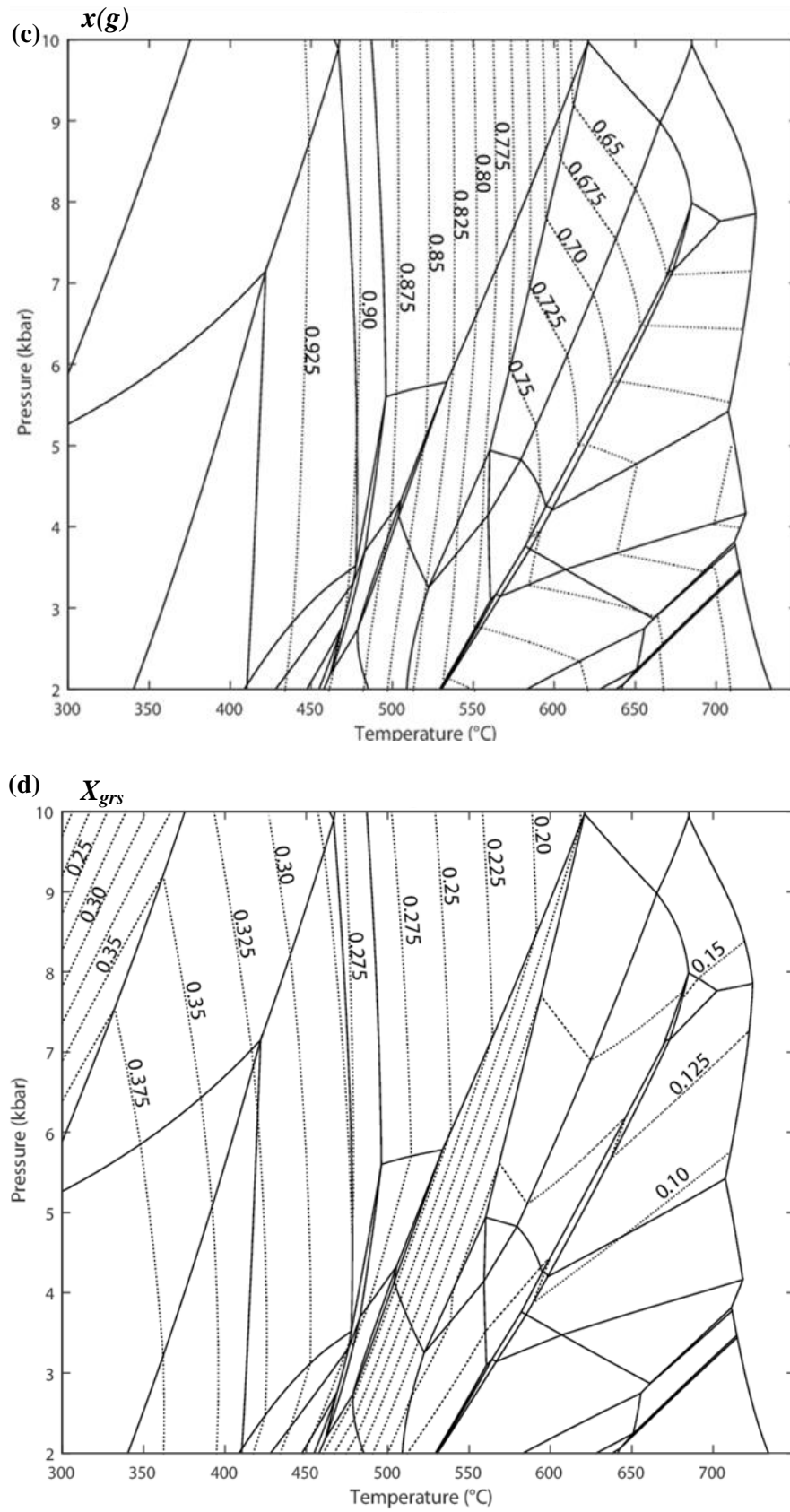
(d) X_{grs}

Figure 4.6. *P−T* pseudosection for J34 contoured for (a) garnet mode and garnet compositions (b) X_{sps}, (c) *x(g)*, and (d) X_{grs} all with contour interval of 0.025.

Fernandes, J.

(a) Core contours for a pure H₂O system

(b) Rim contours for a pure H₂O system
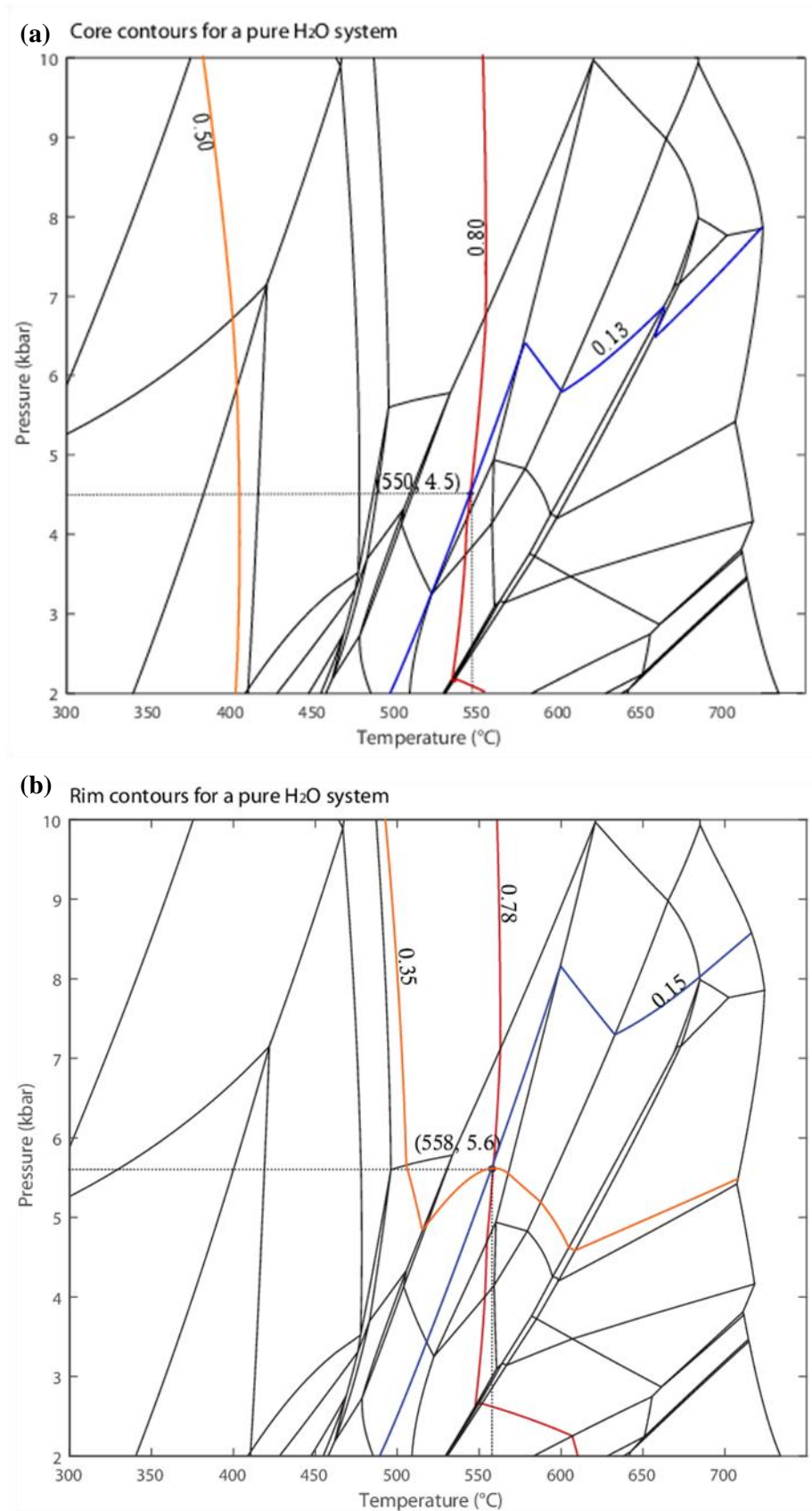
Figure 4.7. Garnet content of X_{sps} in orange, $x(g)$ in red and X_{grs} in blue in core (zone 1) and at rims (zone 4). See Fig. 4.4a, Table 4.2.

Fernandes, J.

Fig. 4.7 shows the calculated isopleths for the measured core and rim garnet compositions, calculated on the assumption that the metamorphic fluid was pure H_2O (values from Table 4.2, zone 4 for rim and zone 1 for the core). The contours X_{sps}, $x(g)$ and X_{grs} measured in the core (Fig. 4.7a) do not intersect. The $X_{sps} \approx 0.50$ plots at the low temperature end of the pseudosection while the other contours intersect at P ~4.5 kbar and T ~550 °C, in the chl-bt-ms-grt-rt-mrg-qtz field (pink, Fig. 4.5). The rim contours for X_{sps}, $x(g)$ and X_{grs} intersect at ~5.6 kbar and ~560°C (Fig. 4.7b), also in the chl-bt-ms-grt-rt-mrg-qtz field (Fig. 4.5).

The isopleth intersections on this initial diagram, in which dolomite cannot be considered, plot in a margarite-bearing field (pink, Fig. 4.5), rather than in the margarite-free field (red, Fig. 4.5), even though careful searching using EDS methods identified no margarite in the rock. This rock will be further investigated using a mixed fluid (H_2O-CO_2) system. The next section explores the effects of a mixed (H_2O-CO_2) fluid.

Peak field in a mixed fluid system

The peak assemblage observed in J34 is quartz, garnet, biotite, muscovite, apatite, chlorite, dolomite and rutile. Since dolomite is present in the rock, the coexisting metamorphic fluid must have contained some CO_2. Hence, mixed fluid calculations with an XCO_2 component are necessary to properly define a stability field for the assemblage. The absence of fluid inclusions makes it impossible to robustly constrain the XCO_2 value. It is, however, possible to obtain limiting P-T-XCO_2 constraints for the formation of the observed mineral assemblage, by exploring the calculated effects of XCO_2 on the stability of dolomite in the peak assemblage (Fig. 4.8).

Figure 4.8 shows the shift in the bt-chl-grt-ms-rt-qtz field dependent on the stability of calcite and dolomite fields, with the increase in XCO_2 content. The calculated stability of dolomite is strongly dependent on XCO_2 (Fig. 4.8). Calcite and dolomite co-exist in a very narrow field in the P–T pseudosection but generally do not co-exist.

Fig. 4.8 (cont'd)

Fernandes, J.

(b)

XCO₂ = 0.01

Peak assemblage
(without dolomite)

bt chl grt
ms rt

+(spn)-

-(mrg)+

-(cal)+

-(ep)+

+(dol)-

+(cal)-

(c)

XCO₂ = 0.1

Peak assemblage

bt
chl
dol
grt
ms
rt

+(dol)-

-(bt)+

+(cal)-

-(cal)+

+(dol)-

Fig. 4.8 (cont'd)

Fernandes, J.
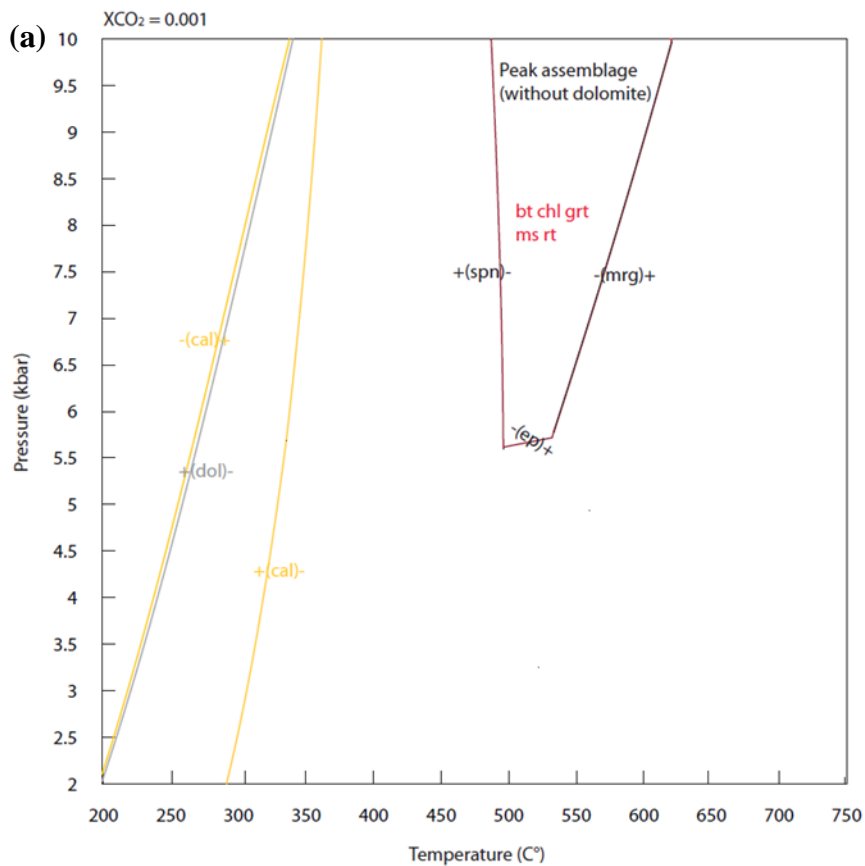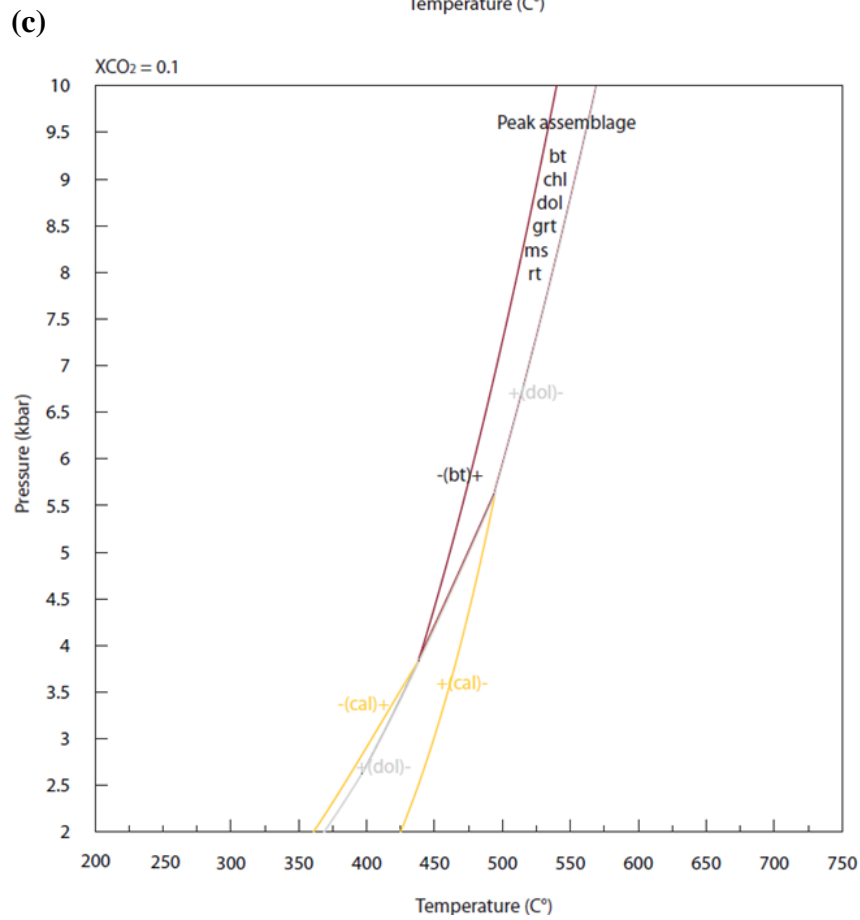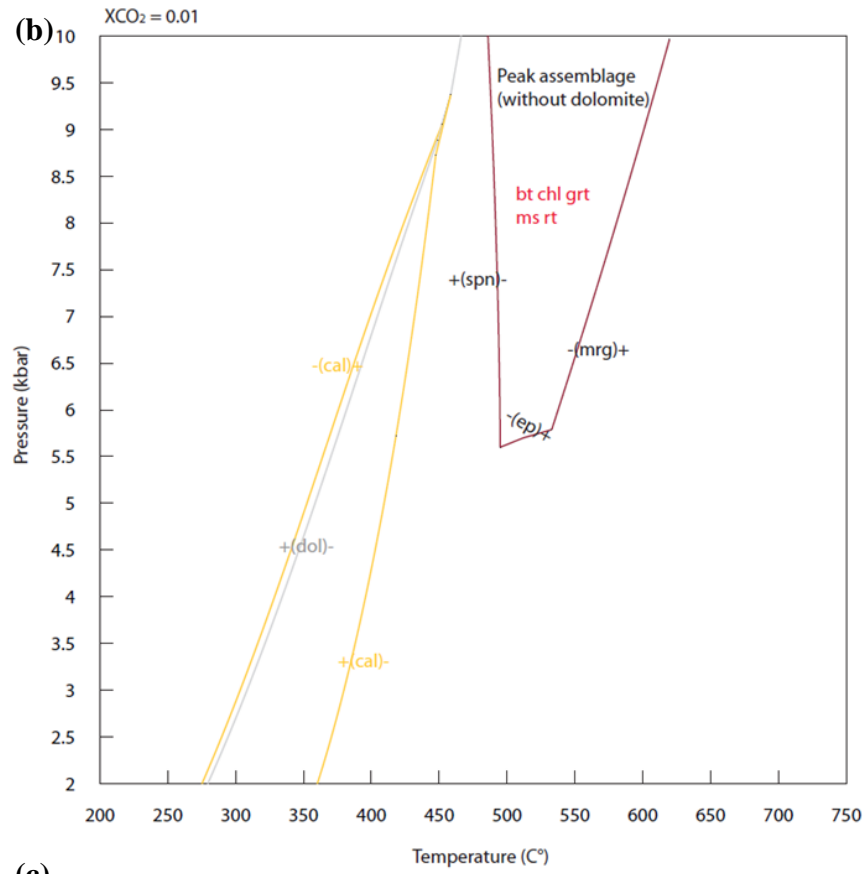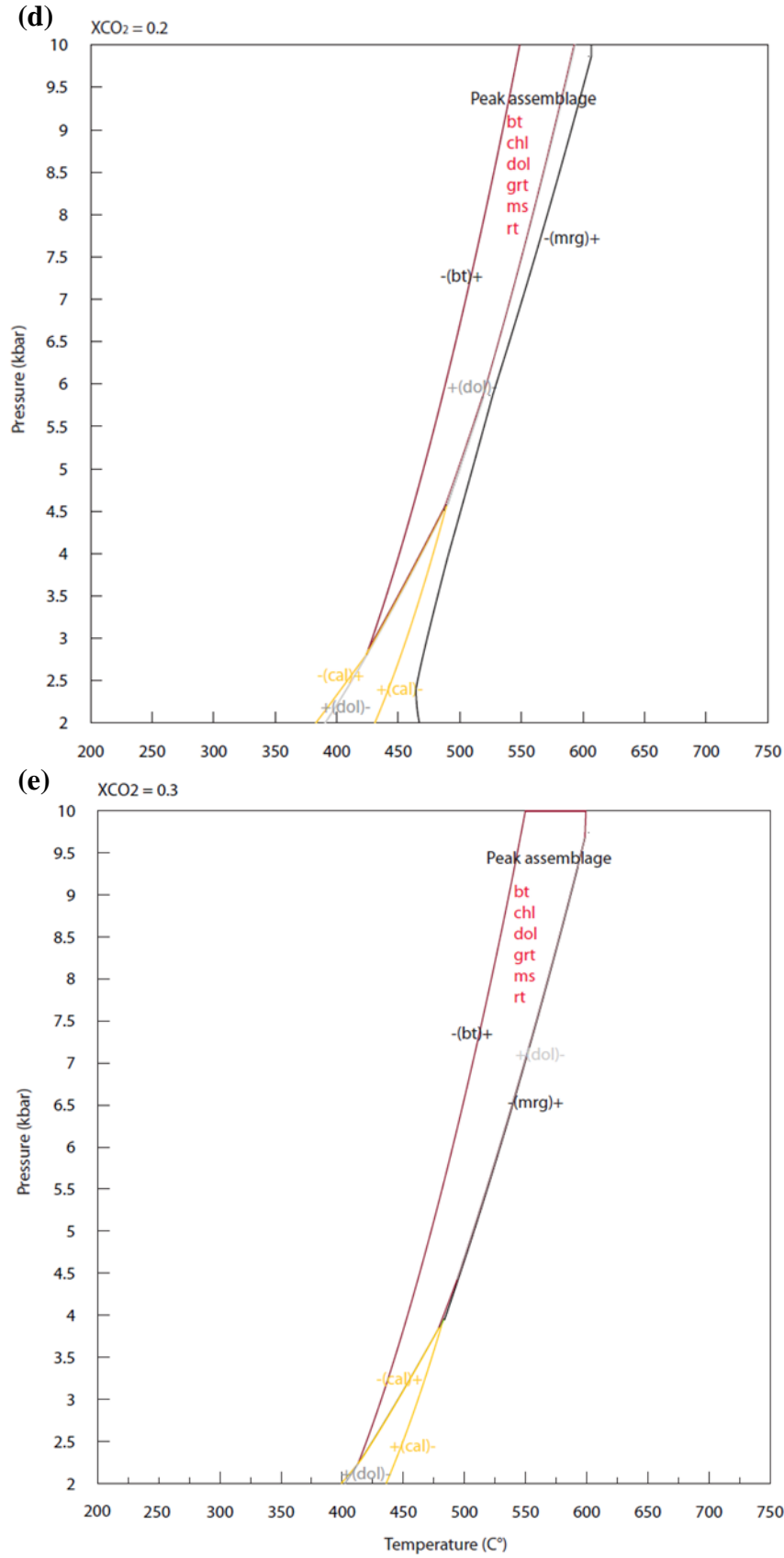
(d)   XCO₂ = 0.2

(e)   XCO2 = 0.3

Figure 4.8. Mixed fluid calculations showing a peak assemblage shift with carbonate modes a)
XCO_2 = 0.001, b) XCO_2 = 0.01, c) XCO_2 = 0.1, d) XCO_2 = 0.2 and e) XCO_2= 0.3.

Fernandes, J.

The calcite and dolomite stability fields typically take the form of an inverted 'Y', with dolomite stable to the low-*T* side, and calcite stable in a triangular region, located to the low-*P* side of the intersection of the calcite and dolomite zero-mode lines. With increasing *X*CO₂, the field where dolomite is stable expands to higher *T*'s, and the triangular field where calcite is stable shifts downward to lower *P*'s. The results of the *P*–*T* pseudosection calculations indicate that XCO_2 values 0.001, 0.01 are too low; dolomite would not be stable with the observed peak metamorphic mineral assemblage (Fig. 4.8a–b). A fluid with $XCO_2 \approx 0.1$ pushes the dolomite-in line up-*T* just enough to create a narrow peak field, where dolomite is stable, without margarite. This shows that $XCO_2 = 0.1$ is just sufficient to stabilise dolomite in the peak assemblage. At higher XCO_2, the region where dolomite can be stable expands further, to higher *T* (Fig 4.8c–d).
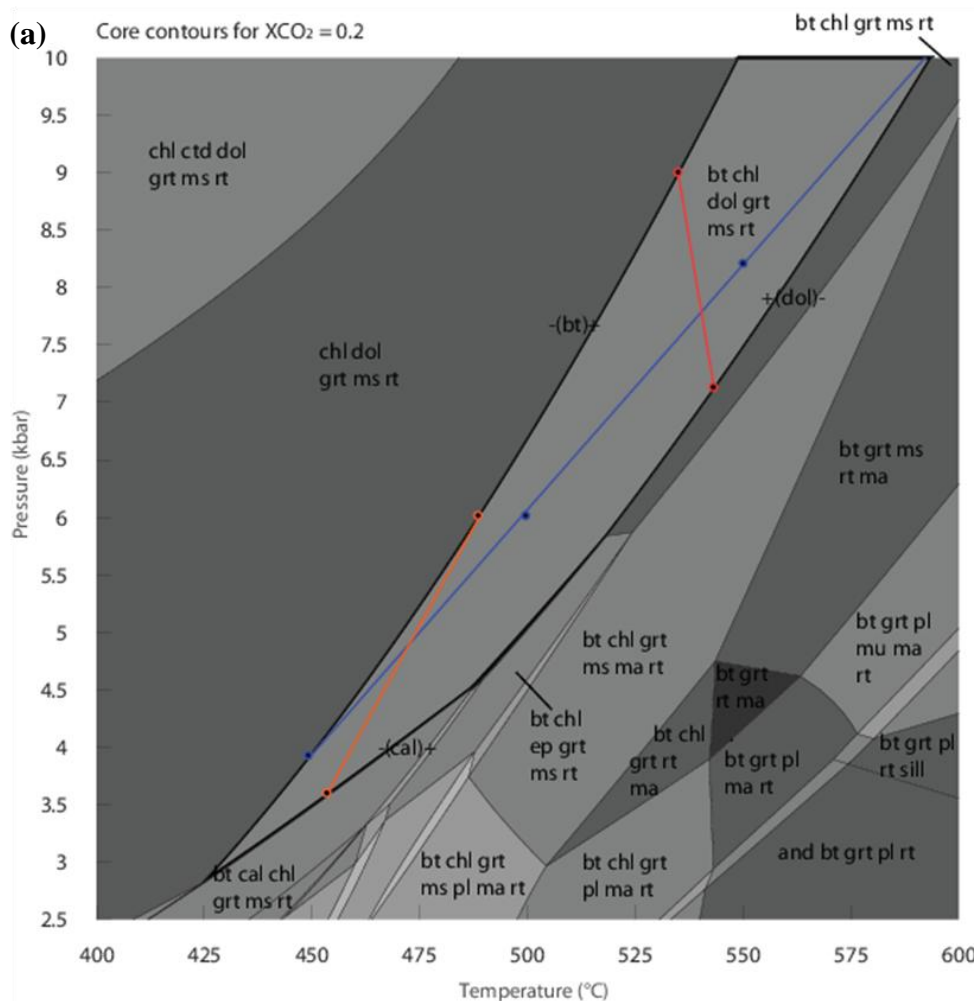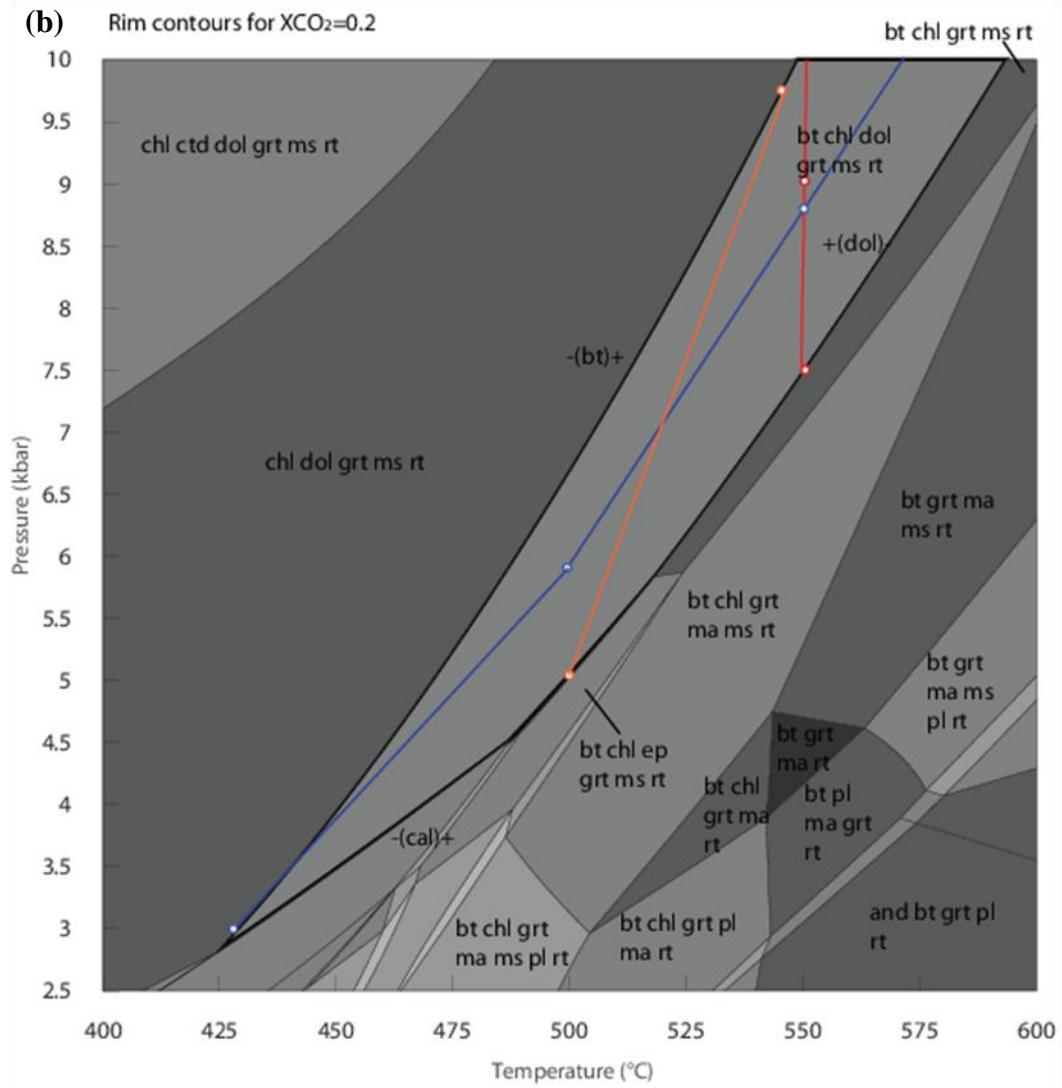
Figure 4.9. Contoured pseudosection A12E for *XCO*₂ = 0.2, *X*_sps in orange, *x(g)* in red and *X*_grs in blue, in core (zone 1) and at rims (zone 4). See Fig. 4.4, Table 4.2. The peak field has borders highlighted in black.

At an XCO_2 of 0.2 (Fig. 4.8d) the stability field for the observed peak metamorphic mineral assemblage (with dolomite, without margarite) has been fully exposed. On that basis, an XCO_2 of 0.2 was taken to represent an approximate XCO_2 for the development of the observed mineral assemblage.

The pseudosection (Fig. 4.9) for $XCO_2 = 0.2$, has been contoured to provide *P–T* constraints for garnet core (Fig. 4.9a) and rim (Fig. 4.9b). For both the cores and rims, the isopleths for X_{sps}, $x(g)$= Fe number, and X_{grs} (see Fig. 4.4, Table 4.2) pass through the stability field of interest. The isopleths do not intersect each other perfectly, but are consistent with garnet growth over a small temperature range, as

45

Fernandes, J.

pressures increased. While it might be possible to refine the *P-T-X*CO_2 estimates by further iterative calculations, the results obtained here are informative, and provide *P–T* constraints of ~475–535 °C/5–9 kbar for the garnet core (Fig. 4.9a), and 520–550 °C/7–10 kbar for the garnet rim (Fig. 4.9b).

Fernandes, J.

INTERPRETATION

Mixed fluid calculations

The pseudosection (mixed fluid) peak assemblage is qtz-chl-bt-ms-grt-rt-dol (Fig. 4.8c−e). The Ca locked up in the margarite (in the pure water system) may be used in stabilising dolomite in the mixed fluid calculations for $XCO_2 \geq 0.1$. On recalculation with $XCO_2 \geq 0.1$, dolomite is stabilised and the pseudosection predictions match the observed rock assemblage. Values of XCO_2 lower than 0.1 are not enough to stabilise dolomite in the peak field with the absence of calcite. With increasing XCO_2 content the calcite stability field slides up-*T* and down-*P* while the dolomite field expands to higher temperatures. The peak field bt-chl-grt-ms-rt-q extends into lower temperatures but becomes narrower with increasing XCO_2. This shows that the composition of a mixed H_2O-CO_2 fluid can exert a controlling effect on mineral assemblages and the extent of mineral assemblage stability fields. With an $XCO_2 = 0.001$ and 0.01 the stability field of the peak assemblage is not affected much. But with an $XCO_2 = 0.1$ and 0.2 the peak field changes in shape and *P*−*T* conditions (Fig. 4.8). The contours for $XCO_2 = 0.2$ provide *P*−*T* conditions of ~ 475−535 °C/5−7.7 kbar for the core, and 520−550 °C/>7 kbar in the rim.

The mixed fluid calculations (Fig. 4.8) show the extent to which the stability fields change with the introduction of a mixed fluid. In this case the presence of dolomite makes a substantial difference to the stability of the other phases. For sample J34, which contains dolomite, the initially calculated pure water system pseudosections are only a simplification of J34 and are not a suitable representation of the more complex system J34 actually evolved in. In the pure H_2O system, the peak field has *P*−*T* constraints 480−620 °C/5.5−10 kbar, whereas in the mixed fluid system with $XCO_2 = 0.2$ the *P*−*T* conditions are 425−600 °C/2.4−10 kbar. The estimated *T* conditions are not all that different, but calculations for a system involving a pure H_2O metamorphic fluid do not adequately describe the rock.

Fernandes, J.

Garnet growth and textures

An investigation of the rock texture can provide a clue to the mineral growth history. Changes in chemistry and inclusions in the garnet core separate it chemically and texturally from inclusion free zones 2, 3 and 4.

Textural similarities like absence of inclusions within zones 2–4 and smooth concentric zoning of zones 2–4 may indicate continuous growth zoning with no interruption to growth for zones 2–4. Inclusions are typically seen on zone boundaries but not within each zone. The core has an irregular zone of growth around it which is texturally different from the continuous zoning of zones 2, 3 and 4. Compositional discontinuity is reflected in compositional trends as Mn spikes around the core. This boundary between zone 1 and 2 are not smooth but corroded and may be explained by one of the following reasons:

(1) **Inherited core**: An inherited core can form a site suitable for nucleation of a garnet over it, at a later time. The presence of this separately nucleated core may be evidence for a polymetamorphic history.

(2) **Dissolution (resorption) releasing Mn back into the bulk rock chemistry and regrowth, between the core and zone 2**: Dissolution of a garnet core (Kohn & Spear 2000, Prakash *et al.*, 2007) and regrowth causes a compositional spike (usually Mn in garnet) in the newly grown zone after resorption. On dissolution components (other than Mn) may be used up by other minerals in the rock enriching the new forming garnet zone with Mn. Thus the Mn spikes in zone 2 are explainable by the effect of resorption. The presence of inclusions in the core and absence in the three outer zones could be interpreted as a representation of changing metamorphic conditions before and after resorption.

Some garnets appear unzoned. This could be explained by either, the effect of the thin section slice or lack of zoning detail in smaller garnets compared to larger garnets.

(1) **Effect of the thin section slice**: The garnet size and zonation depends on the cut through which the thin section was cut, if it was cut through the outer zones only

Fernandes, J.

evidence of those will be observed. This does not imply that the other zones were not recorded in this garnet, only that this cut is not representative of the complete garnet. (2) **Lack of much zoning detail in smaller garnets compared to larger garnets:** Assuming the cut is representative of the whole garnet, if the small garnet nucleated after the large garnet it preserves only a later metamorphic history as recorded in the compositional transect.

Garnet history

Zoning profiles that are continous and smooth are indicators of a single uninterrupted garnet growth event (St-Onge, 1987). The zoning profiles show evidence of Mn spikes indicating resorption of the garnet and regrowth this is supported by corroded zones around the core seen in the BSE image. Late stage textures that indicate a multistage history like cross cutting veins, crystal over growths, pseudomorphs (Toteu & Macaudiere, 1984; Cesare, 1999; Faryad & Hoinkes, 2004) are absent. However the presence of texturally different core and rim — a corroded core with a smoothly zoned rim, core with inclusions and inclusion free rims, point out a change in conditions during core and rim growth. Garnet resorption during the single prograde history can explain the texture and compositional trend observed. Diffusion in this sample is negligible since the rate of intragranular diffusion is slow in moderate grade rocks (Yardley, 1977; Zhang *et al.*, 2000) and the growth zoning is well-preserved in the outer parts of the garnet. With *P−T* conditions of 520–550°C/7–10 kbar, assuming the rock was exposed to these conditions for 5 Ma the diffusion of Ca and Mn = 0.01 μm, Fe = 0 and Mg = 0.03 μm, which is negligible (calculations based on Carlson, 2006). Hence, the compositions of the garnet in this rock have not been reset by difusion. In addition if the core is inherited, this may be evidence of a polymetamorphic record in this rock. If the core has undergone resorption then initial core nucleation occurs earlier than the resorption, and may also be evidence for polymetamorphism. It is possible that the coexisting metamorphic fluid content of the system varied and may have enhanced the observed resorption.

From the above investigation of J34, the most probable *P–T* conditions for garnet growth are ~475–535 °C/5–9 kbar for the garnet core (Fig. 4.9a), and 520–550 °C/7–10 kbar for the garnet rim (Fig. 4.9b).

Fernandes, J.

SAMPLE A12E (37661)

RESULTS

Mineral assemblages and textures

Thin-section petrography

Sample A12E (Fig. 4.10 a–l) is a fine grained rock composed of alternating bands of quartz and garnet, both interspersed with biotite and white mica. Minor minerals present are apatite, rutile and plagioclase. The garnet bands and mica (biotite and white mica) define a schistosity in the rock. The quartz grains grow up to ~265 µm. The rock has variably sized garnet crystals of sizes between <1 µm and 300 µm. The large garnets have grown isolated from other garnet in the quartz rich bands. The small garnets cluster together forming dense layers of fine garnet. In Fig. 4.10c, 4.12d and 4.14a a large garnet porphyroblast has broken and smaller garnets have formed curved bands around the garnet. Biotite is the abundant mica (Fig. 4.10e and f). The white mica is probably muscovite, but other white micas such as margarite (Ca-bearing) and paragonite (Na-bearing) cannot be ruled out by optical petrology alone. The mica composition is further examined using higher resolution µXRF and SEM-based composition maps below. Biotite (Fig. 4.10e and f) books grows to a maximum thickness of ~110 µm and ~720 µm in length but it can occur as smaller flakes that overlap to form bands. The white mica (Fig. 4.10f) occurs as fine flakes up to ~10–500 µm in length and <5–80 µm in thickness within the quartz bands as well as the biotite rich bands. Other minerals are chlorite (Fig. 4.10k and l), apatite (Fig. 4.10e and f), rutile (Fig. 4.10g and h) and plagioclase (Fig. 4.1i and j).

50

Fig. 4.10 (cont'd)

Fernandes, J.
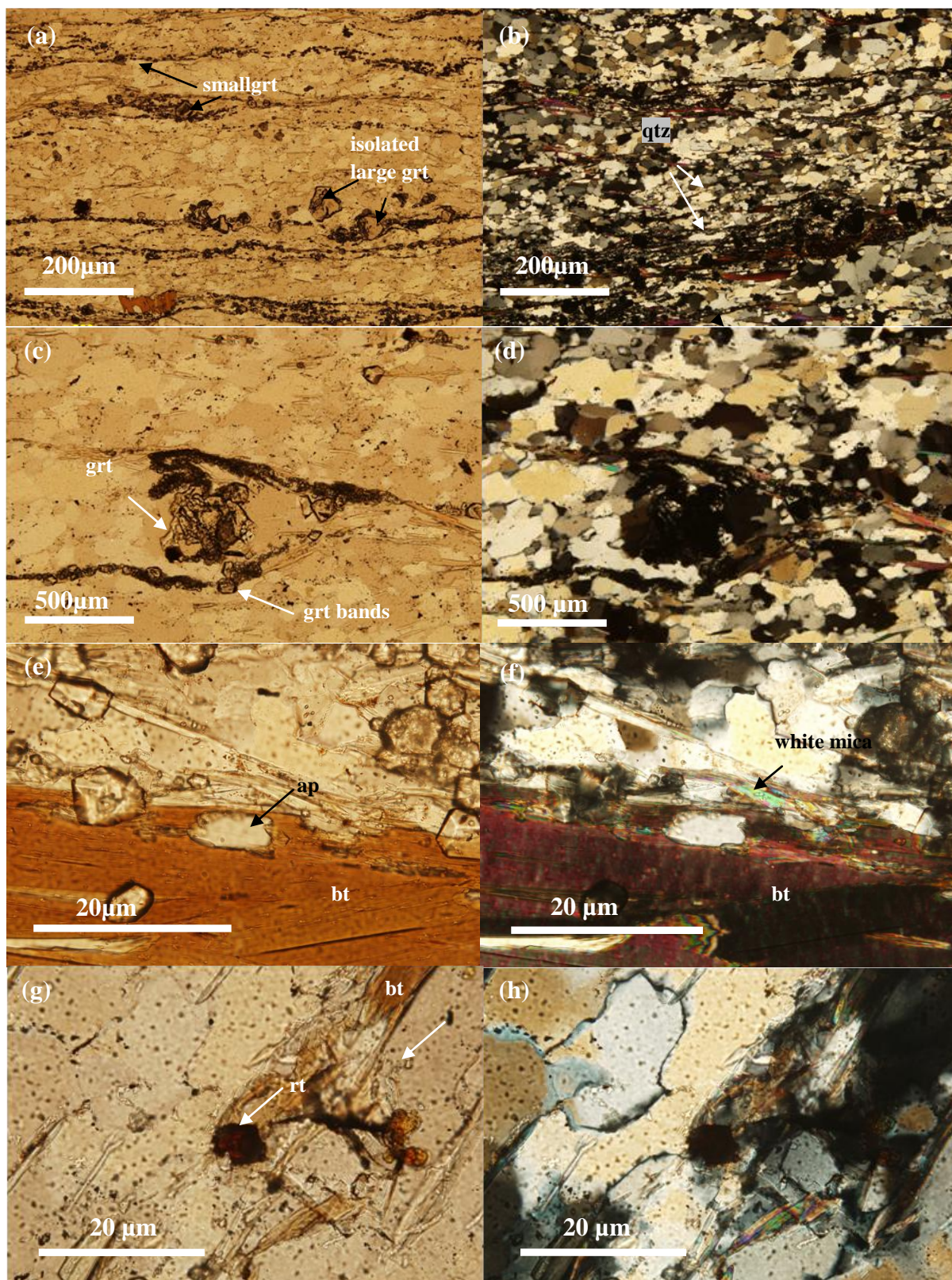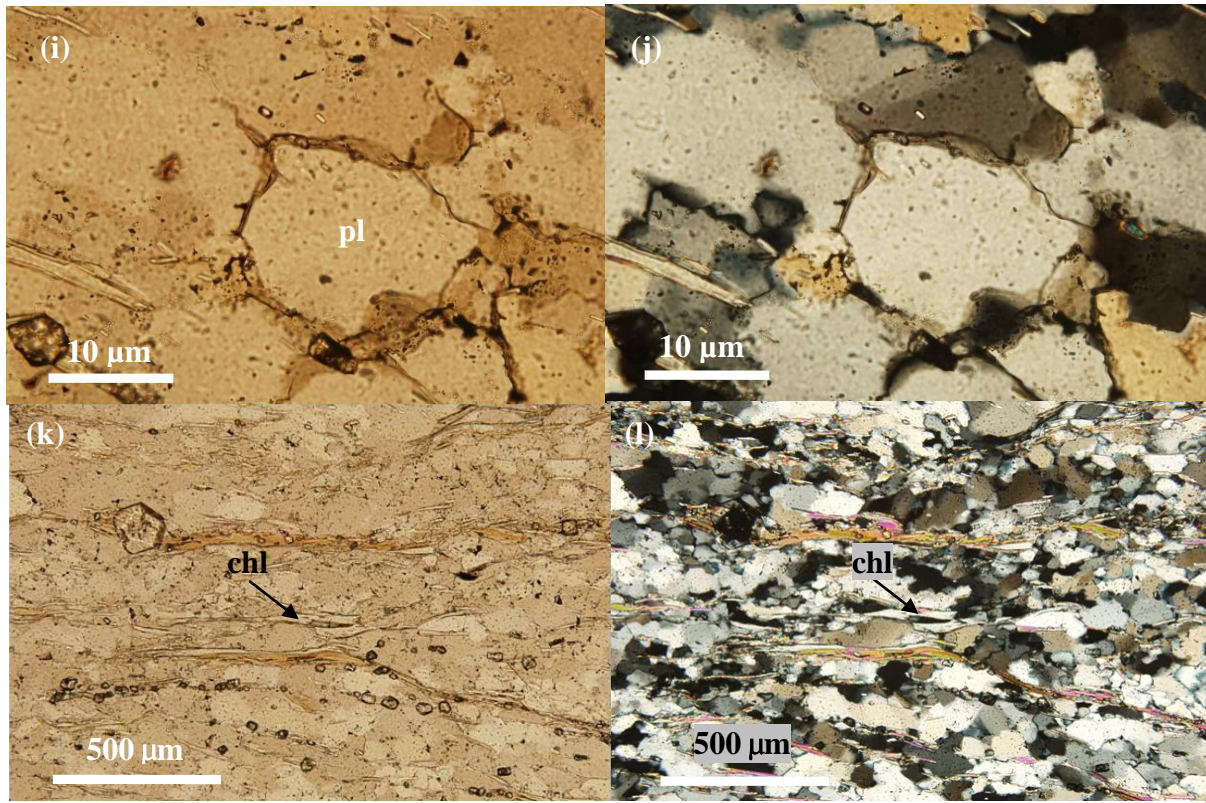
Figure 4.10. Thin section images for A12E a, c, e, g, i and k in plane polarised light and b, d, f, h, j and l in crossed polarised light. Panels a, b, c and d show the quartz rich rock with variably sized garnets forming layers. Panels e, f, g and h show close up views of the assemblage in the rock.

Micro X-ray fluorescence composition maps

The µXRF maps show the distribution of elements in the rock on the thin-section scale (Fig. 4.11). The siliceous rock is interspersed with mica (Fig. 4.11a) and narrow bands of Mn- and Fe- rich garnet (Fig. 4.11b). Compositional banding is not uniform; some bands are thicker and contain more garnet population than others.

Fernandes, J.
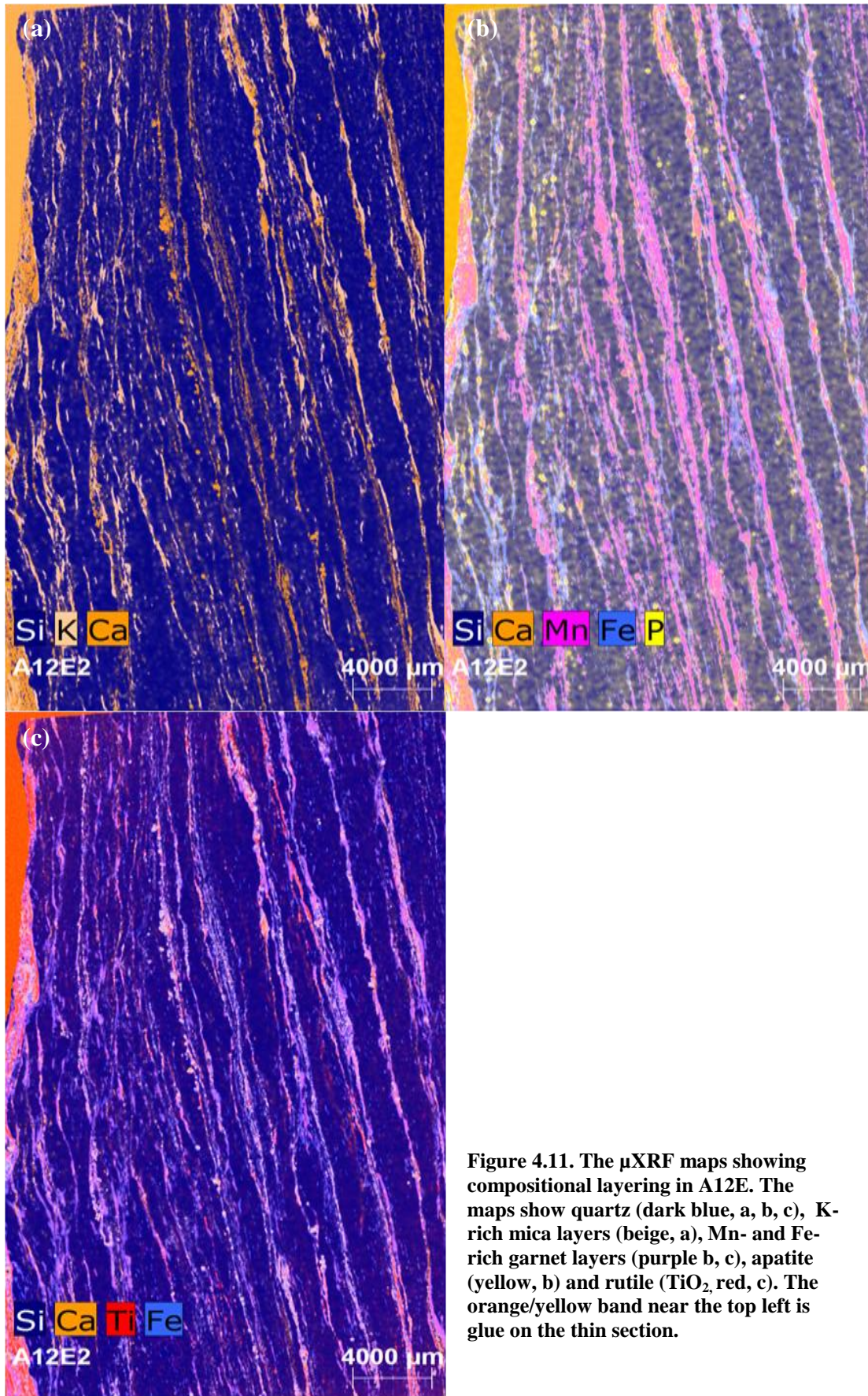
Figure 4.11. The µXRF maps showing compositional layering in A12E. The maps show quartz (dark blue, a, b, c), K-rich mica layers (beige, a), Mn- and Fe-rich garnet layers (purple b, c), apatite (yellow, b) and rutile (TiO_2, red, c). The orange/yellow band near the top left is glue on the thin section.

Fernandes, J.

Scanning Electron Microscopy based composition maps

Scanning Electron Microscopy based composition maps of sample A12E (Fig. 4.12) reveal textural and compositional complexity in the garnet growth record. The garnet ranges in diameter from 10–500 μm. Both the large and small garnet have Mn-rich (bright pink) cores and Fe-rich (blue) rims (Fig. 4.12a, b, c and d). Most garnet is zoned but some grains appear unzoned, with compositions similar the zoned garnet rims. The apparently-unzoned garnet may represent a slice of rim of a larger zoned garnet. Biotite is more abundant than muscovite (Fig. 4.12a, b, c and d) and occurs along with it (Fig. 4.12c and d). Plagioclase-rich layers can alternate with biotite-rich layers (Fig.4.12a, b, c and d). Apatite (Fig. 4.12a, c and d), chlorite (Fig. 4.12c and d) and rutile (Fig. 4.12a and c) are minor phases. The large garnet contains inclusions of chalcopyrite (Fig. 4.12a), apatite (Fig. 4.12a and c), biotite (Fig. 4.12b) and quartz (Fig. 4.12). A large garnet porphyroblast (Fig. 4.12d) is wrapped by laminae that contain biotite, plagioclase and abundant small garnet, in the dominant foliation.

In the large garnet (labelled "zoned garnet", Fig. 4.12a) the Mn-rich core (pink, Fig.4.12a) is overgrown by a Fe-rich rim, which contains numerous small Mn-rich areas, probably recording multiple sites of garnet nucleation. A few of the large garnets have been broken and pulled apart, presumably during development of the dominant foliation accompanying mylonitisation along the Alpine Fault.

Fernandes, J.

Fig. 4.12 (cont'd)

Fernandes, J.
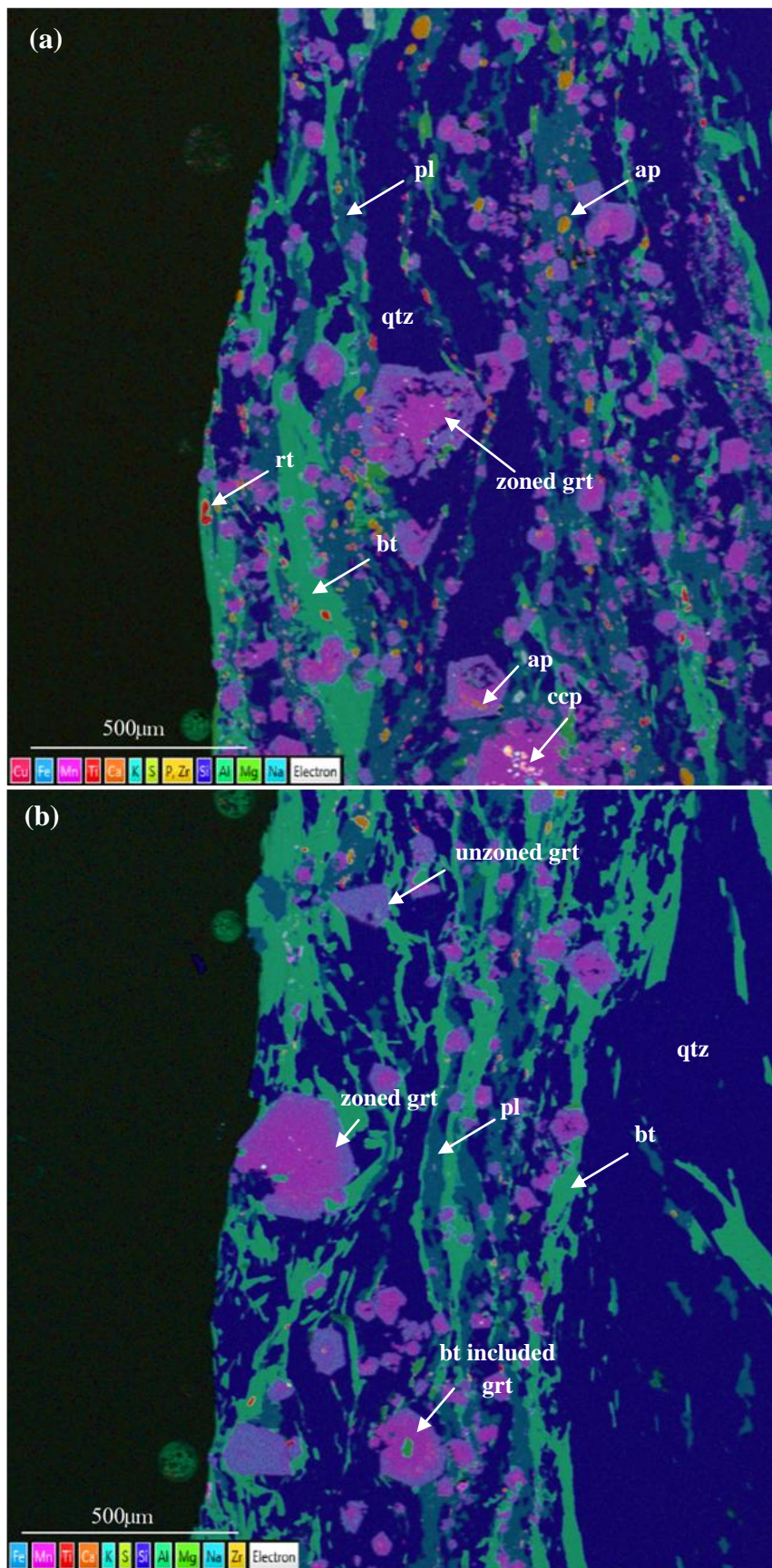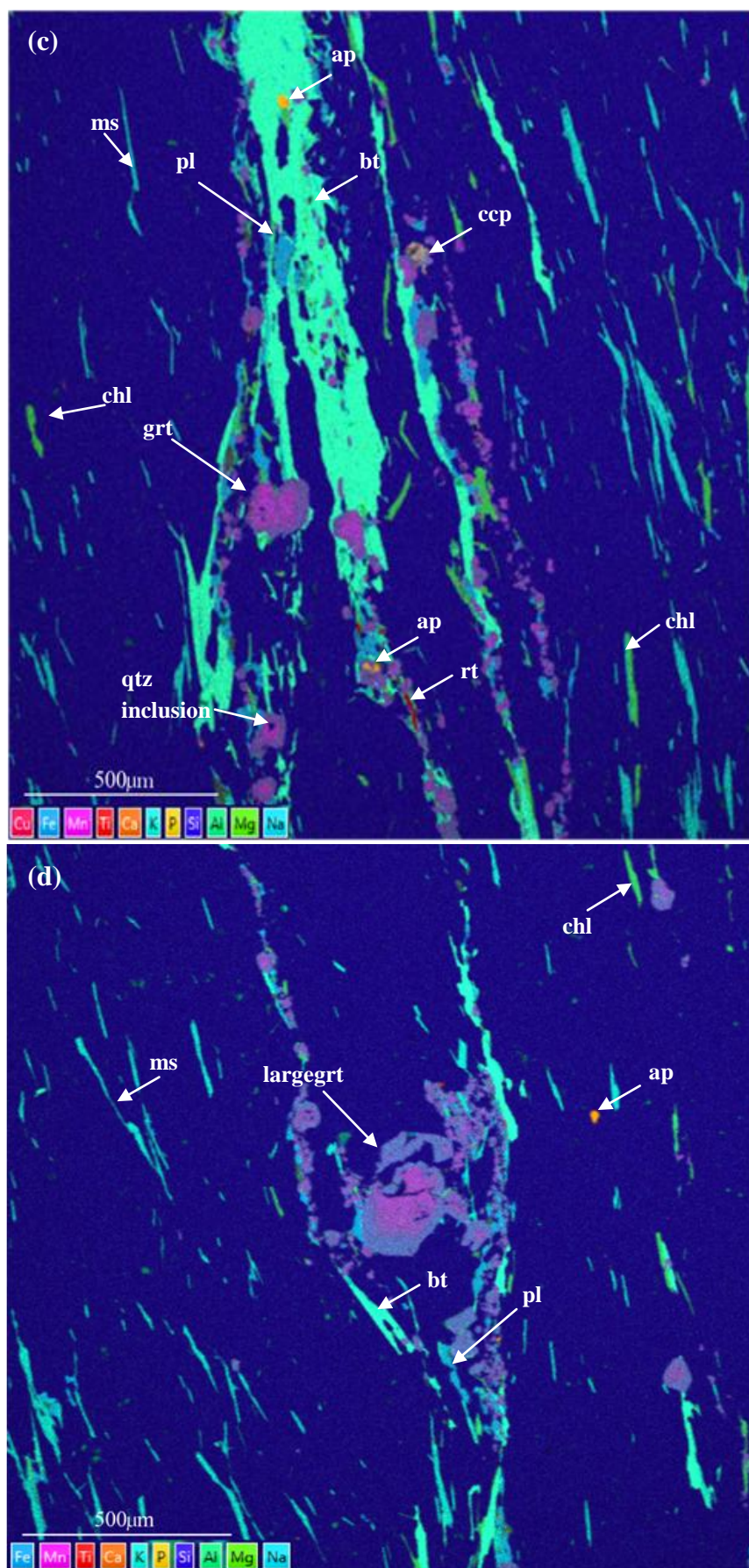
Figure 4.12. SEM-based composition maps of sample A12E. Figure 4.12 shows quartz, variably sized garnet zoned and unzoned (purple, a and b), biotite (bright green, a, b, c and d), muscovite (bluish green, c and d), plagioclase (pale blue, Fig. a, b, c and d), apatite (orange, a, c, d), chlorite (c and d) and rutile (red, a and c). Inclusions of chalcopyrite, quartz, biotite and apatite are present in the garnet (c).

Electron Probe Micro-Analysis

The results from EDS determined that the plagioclase identified by thin section petrography is oligoclase. Results of BSE imaging and garnet composition data collected along analytical transects are presented in Fig. 4.13a, 4.13b, 4.14a, 4.14b, 4.14c and 4.14d. Representative EPMA results for garnet in Fig. 4.13a are presented in Table 4.3.

Analytical results from transects K-K' (Fig. 4.13b), L-L' (Fig. 4.14b), M-M' (Fig. 4.14c) and N-N' (Fig. 4.14d) are presented in Figs (Fig. 4.13 and 4.14, respectively).
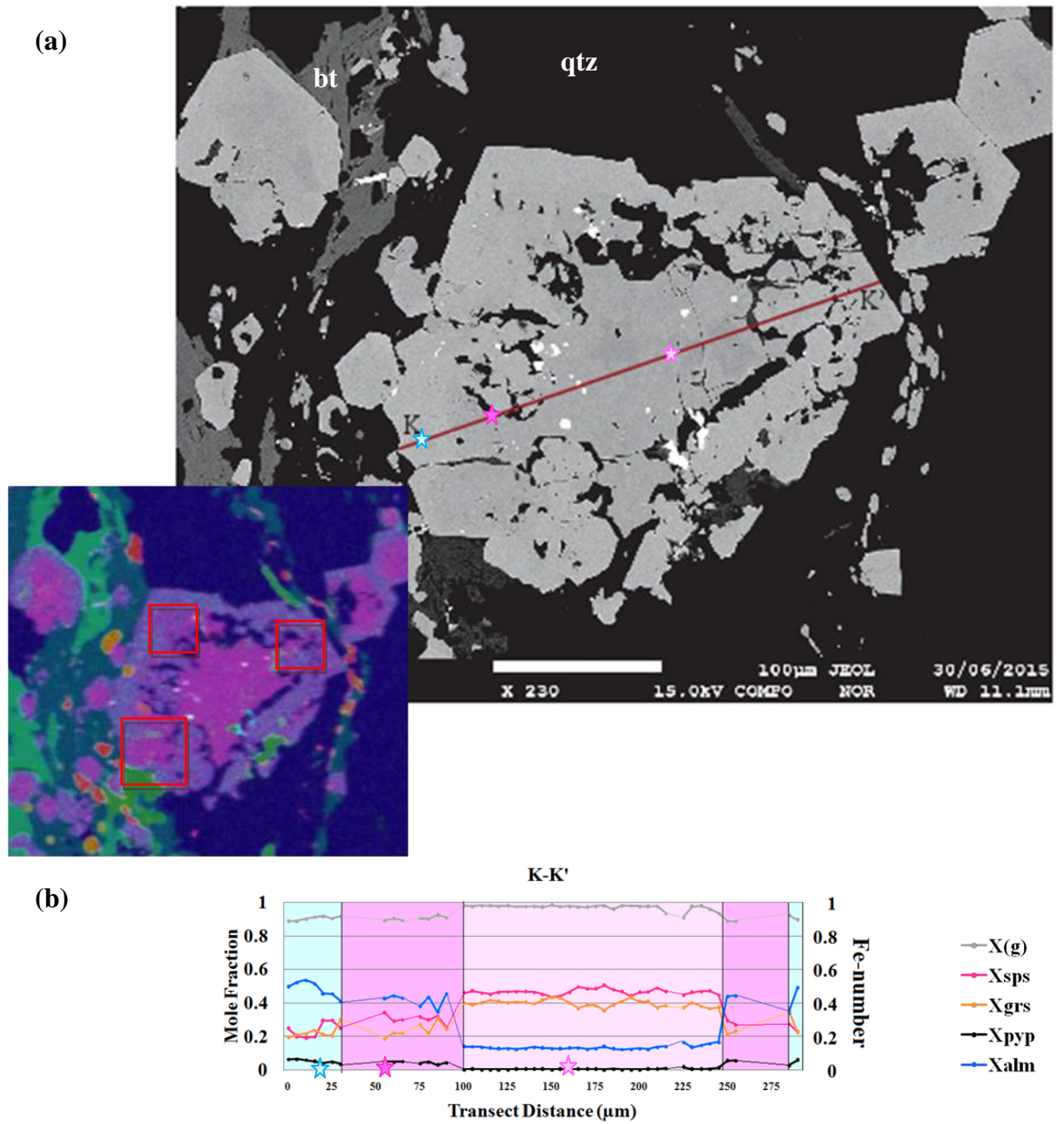
Figure 4.13. (a) Shows a BSE image of multiply nucleated garnet cores, inset SEM based composition image of the analysed garnet. The red boxes show multiple garnet nucleation sites. (b) The results of garnet compositions analyses by EPMA along transect K-K'. The stars are points of representative garnet analyses (Table 4.3).

Fernandes, J.

Although the compositional record from garnet transect K-K' is incomplete, it is possible to identify the inmost core, intermediate and rim zones from the compositional trends. The garnet is separable into the rim zone, an intermediate zone and the inner core. The composition of the rim (Fig. 4.13a, purple in inset garnet image, Fig. 4.13b light blue portion of the transect) is $X_{sps} \approx 0.19–0.30$, $X_{grs} \approx$ 0.19–0.35, $X_{alm} \approx 0.34–0.53$ and $X_{pyp} \approx 0.02–0.07$. Between the core and the rim is an intermediate Fe- and Mn-rich zone where $X_{sps} \approx 0.25–0.34$, $X_{grs} \approx 0.19–0.35$, $X_{alm} \approx$ 0.34–0.46 and $X_{pyp} \approx 0.03–0.05$. This zone is not as Mn-rich as the core. In the core Ca and Mn show a closely related inverse (increase or decrease in X_{grs} corresponds to a decrease or increase in X_{sps}, respectively) trend with $X_{sps} \approx 0.44–0.50$ and $X_{grs} \approx$ 0.36–0.43, $X_{alm} \approx 0.13–0.14$ and a negligible X_{pyp} content (≤ 0.01). The rim zone has high X_{alm} and relatively lower X_{sps} and X_{grs} than the core. The intermediate zone has high X_{alm} and X_{sps}, though X_{sps} is less than the inner core. Figure 4.13a inset shows multiple cores (red boxes, secondary cores) nucleated around the inner Mn-rich core. The Mn-rich intermediate zone therefore represents a zone of secondary garnet nucleation. The inner core has high X_{sps} and X_{grs} with almost constant X_{alm} and negligible X_{pyp}. The garnet therefore has a Mn-rich core, with less Mn-rich nuclei (Fig. 4.13a inset, red boxes) grown around it and a single rim. Thus the multiply nucleated garnets have coalesced into a single crystal.

Figure 4.14 shows a large broken garnet wrapped by layers of smaller garnet and mica. The zoning in the small and large garnet is marked by a distinct colour change and is concentric with the crystal edges (Fig.4.14a). The transect L-L' has garnet composition of $X_{sps} \approx 0.25–0.31$, $X_{grs} \approx 0.20–0.37$, $X_{alm} \approx 0.30–0.47$ and $X_{pyp} \approx$ 0.02–0.07 in the rim and $X_{sps} \approx 0.37–0.58$, $X_{grs} \approx 0.33–0.39$, $X_{alm} \approx 0.30–0.47$ and X_{pyp} $\approx 0.08–0.25$ in the core. Transect M-M' and N-N' have similar compositional trends, they preserve the inner core, a transition zone and the rim. The transition zone is unequal in width on either side of the core. The composition across M-M' is $X_{sps} \approx$ 0.25–0.33, $X_{grs} \approx 0.19–0.26$, $X_{alm} \approx 0.37–0.46$ and $X_{pyp} \approx 0.03–0.07$ across the rim; $X_{sps} \approx 0.28–0.33$, $X_{grs} \approx 0.22–0.34$, $X_{alm} \approx 0.35–0.40$ and $X_{pyp} \approx 0.03–0.05$ across the transition zone; and, $X_{sps} \approx 0.32–0.44$, $X_{grs} \approx 0.34–0.39$, $X_{alm} \approx 0.17–0.32$ and $X_{pyp} \approx$ 0.006–0.02 in the core.

Fernandes, J.

(a)

(b)

(c)

Fig. 4.14 (cont'd)

Fernandes, J.
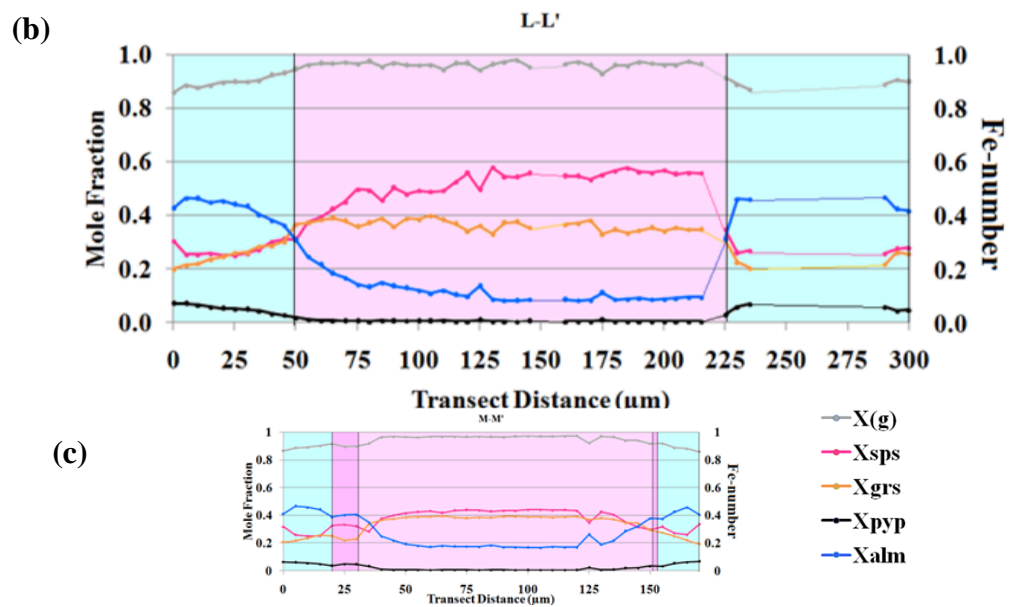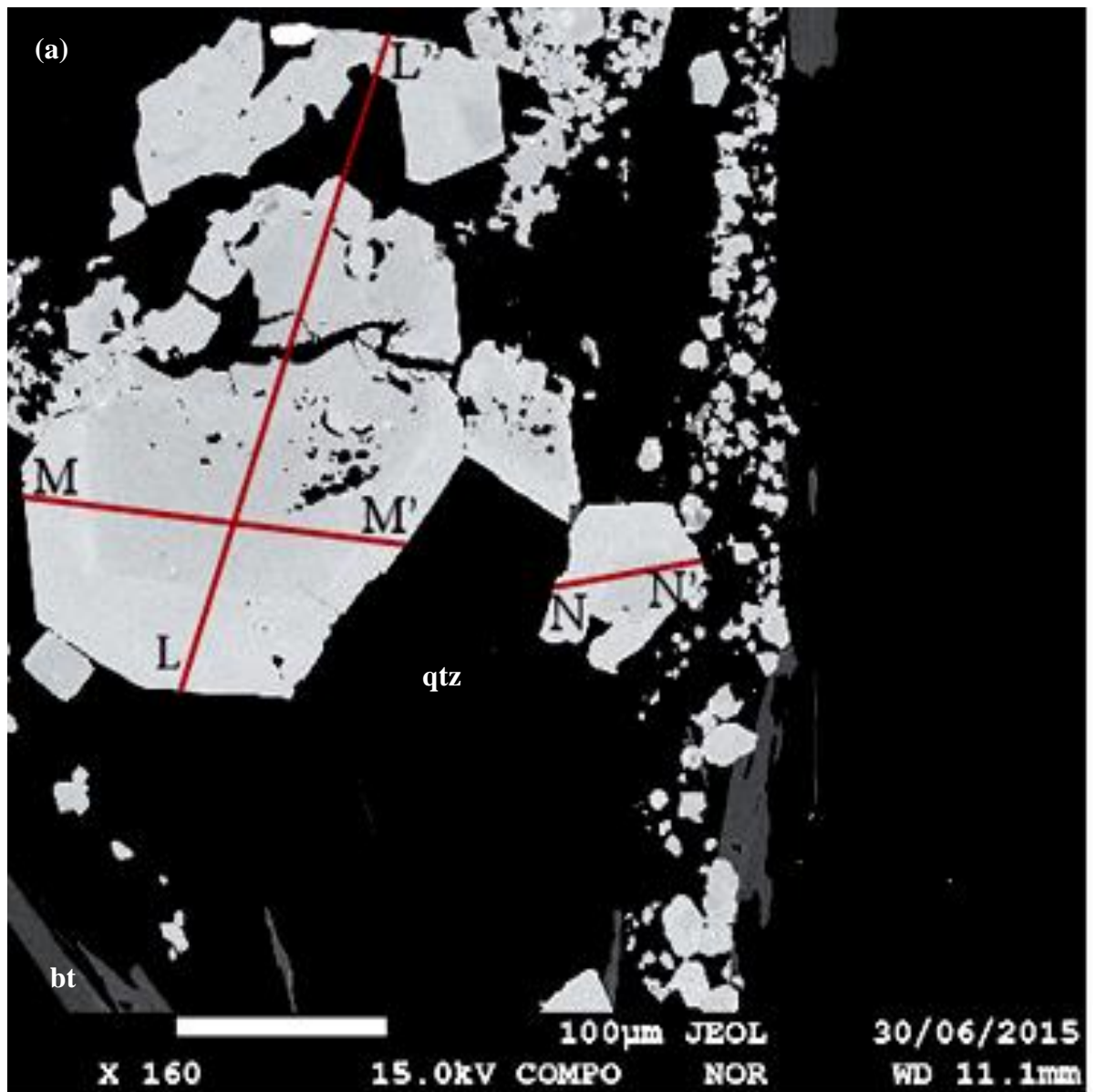
(d)
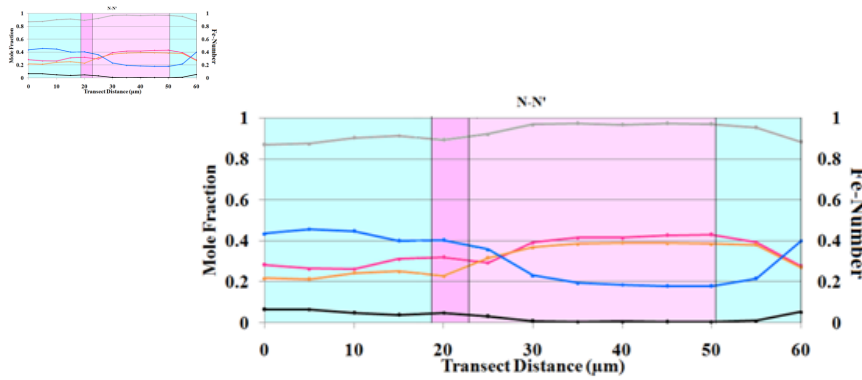
Figure 4.14. (a) Shows a BSE image of a large broken garnet and a garnet band grown around it and the results of garnet compositions analyses by EPMA are shown along (b) Transect L-L' across the broken garnet in the direction of extension, (c) Transect M-M' across the unbroken part of the large garnet and (d) Transect N-N' across the smaller garnet.

The composition across N-N' is $X_{sps} \approx 0.28{-}0.39$, $X_{grs} \approx 0.21{-}0.38$, $X_{alm} \approx 0.22{-}0.46$ and $X_{pyp} \approx 0.01{-}0.07$ across the rim; $X_{sps} \approx 0.32$, $X_{grs} \approx 0.23$, $X_{alm} \approx 0.40$ and $X_{pyp} \approx 0.05$ across the transition zone; and, $X_{sps} \approx 0.29{-}0.43$, $X_{grs} \approx 0.32{-}0.39$, $X_{alm} \approx 0.18{-}0.36$ and $X_{pyp} \approx 0.005{-}0.03$ in the core. Transects M-M' and N-N' show a consistent zoning pattern across both the two garnets. The compositional trends in the large and smaller garnet are similar (Fig. 4.14c and 4.14d), with cores of small garnet ($X_{sps} \approx 0.29{-}0.43$) equally Mn-rich as larger garnet ($X_{sps} \approx 0.32{-}0.44$). The stars in Table 4.3 match stars on transect K-K', Fig. 4.13a.

The next section combines measured mineral chemistry with $P{-}T$ pseudosections to provide a starting point for constraining the metamorphic conditions the rock was subjected to.

Fernandes, J.

Table 4.3. Representative EPMA garnet compositions for A12E.

Oxide wt%	☆ Rim	★ Secondary core	☆ Core
SiO_2	37.26	37.30	37.02
Al_2O_3	21.58	21.62	21.04
TiO_2	0.06	0.018	0.21
MgO	1.04	1.22	0.10
FeO_{total}	20.54	20.25	6.13
MnO	13.11	13.10	22.55
CaO	7.39	7.88	13.17
Cr_2O_3	0.03	0.00	0.00
Total	101.01	101.53	100.21

Normalised to 8 cations

Si	2.966	2.951	2.948
Al	2.025	2.017	1.975
Ti	0.003	0.001	0.012
Mg	0.123	0.144	0.012
Fe_{total}	1.367	1.34	0.408
Mn	0.884	1.878	1.521
Ca	0.630	0.668	0.124
Cr	0.002	0.000	0.000
$x(g)$ =Fe/(Fe+Mg)	0.91	0.90	0.97
$m(g)=X_{sps}$	0.29	0.29	0.50
$z(g)=X_{grs}$	0.21	0.22	0.37
X_{pyp}	0.04	0.05	0.00
X_{alm}	0.46	0.44	0.13

Core content: x(g) = 0.97, m(g) = 0.50, z(g) = 0.37 used in Fig.4.17a.
Rim content: x(g) = 0.91, m(g) = 0.29, z(g) = 0.21 used in Fig. 4.17b.
The stars correspond to Fig. 4.13a transect K-K'.

Fernandes, J.

Petrographic Forward Modelling

P–T pseudosection

A P–T pseudosection for A12E is presented (Fig. 4.15) with the peak assemblage ap-bt-chl-grt-ms-pl-rt-qtz (red), constrained by the albite-out, paragonite-out, sillimanite-out and chlorite-in lines. The predicted P–T conditions are based on the input bulk rock composition, and on the assumption that the coexisting fluid was pure H_2O.

Input bulk composition (mol %)

$SiO_2 = 92.48$, $TiO_2 = 0.14$, $Al_2O_3 = 2.41$, $FeO = 1.25$, $MnO = 0.56$, $MgO = 1.62$, $CaO = 0.57$, $Na_2O = 0.53$, $K_2O = 0.45$, $O = 0.045$.
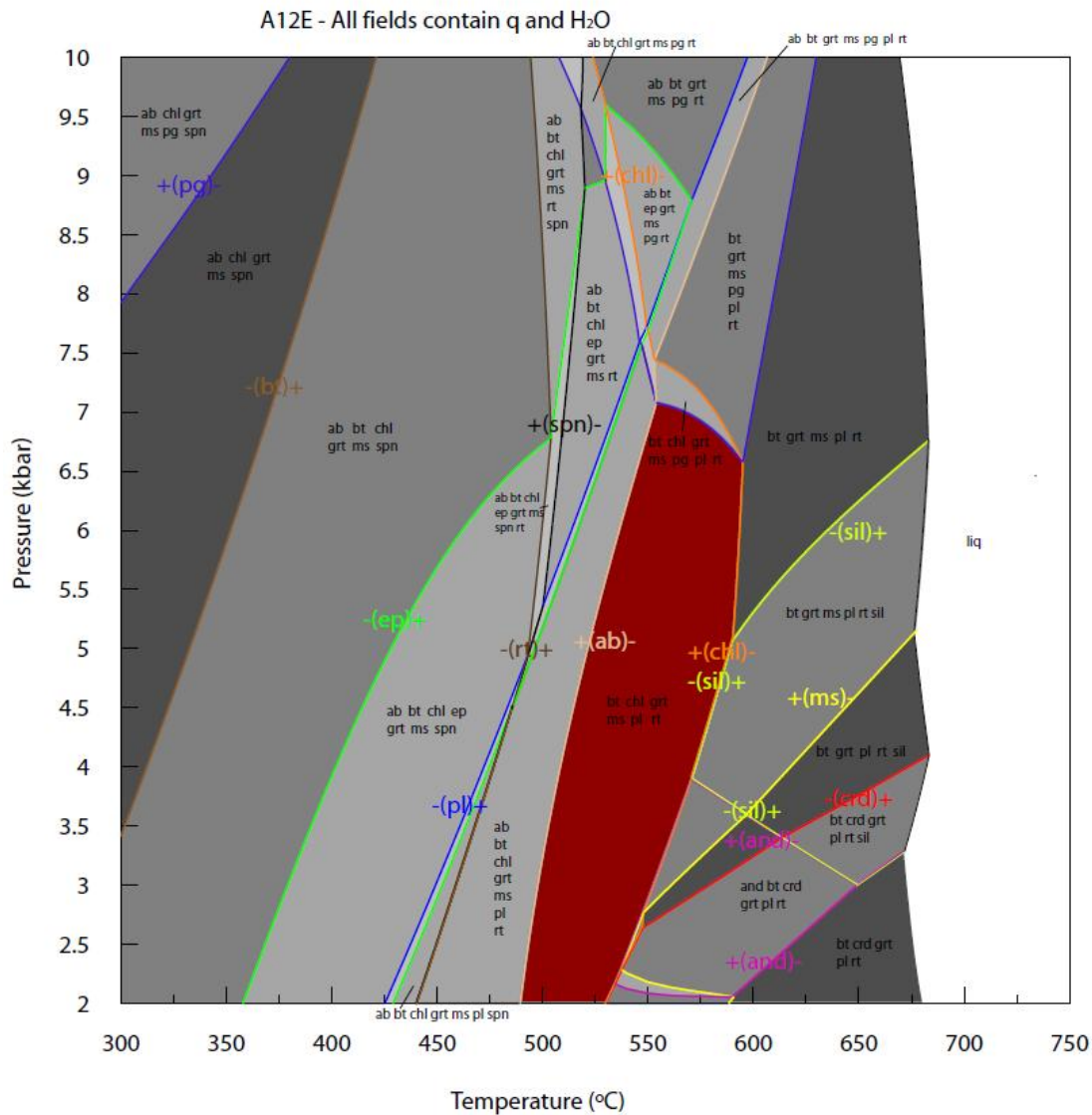
Figure 4.15. Results for calculations of the *P–T* pseudosection for A12E using THERMOCALC for *X*H_2O = 1.0. The peak assemblage bt-chl-grt-ms-rt-pl-q is highlighted in red.

Fernandes, J.

Contoured sections

Figure 4.16 shows contoured pseudosections for garnet mode, X_{sps}, $x(g)$ and X_{grs} produced using TCInvestigator v1.02 (Pearce *et al.*, 2015).

(a) **_Garnet mode_**

(b) X_{sps}

Fernandes, J.
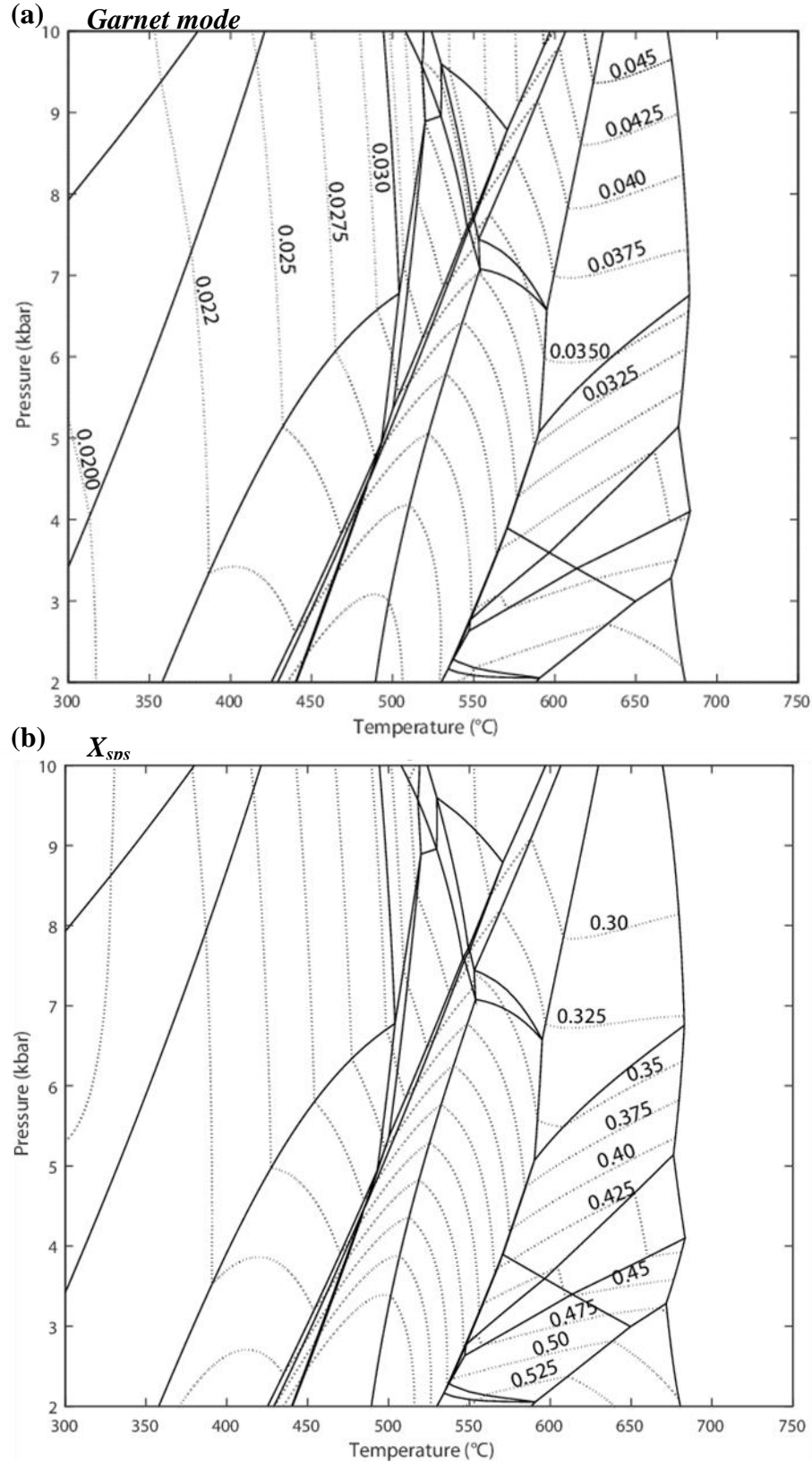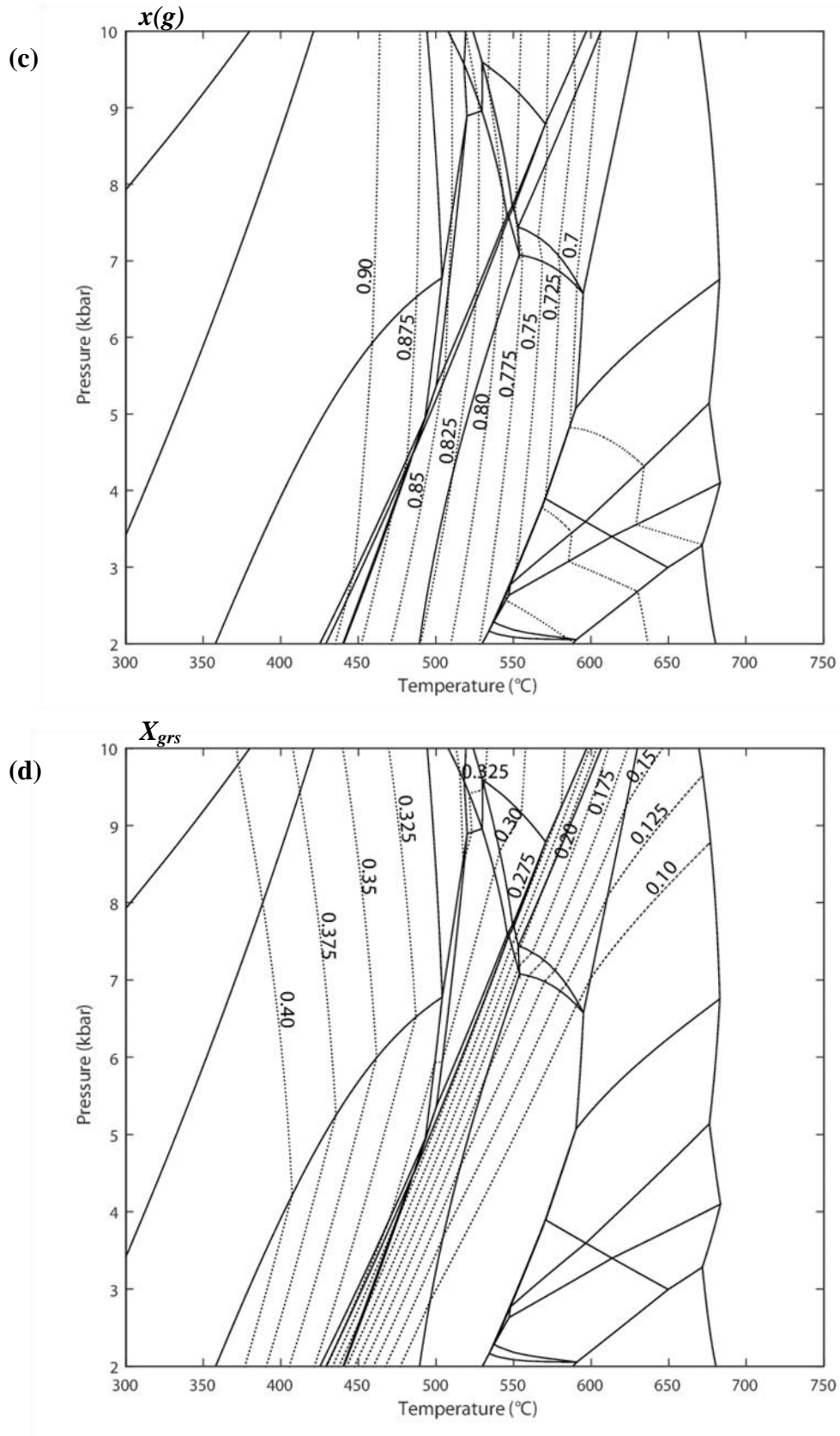
Figure 4.16. *P–T* **pseudosection for A12E contoured for (a) garnet mode, and garnet compositions (b)** X_{sps}**, (c)** *x(g)*, **(d)** X_{grs}**, all with contour interval of 0.025.**

Fernandes, J.

(a) *Core contours*

X(g) - red
Xgrs - blue
Xsps - orange

(b) *Rim contours*
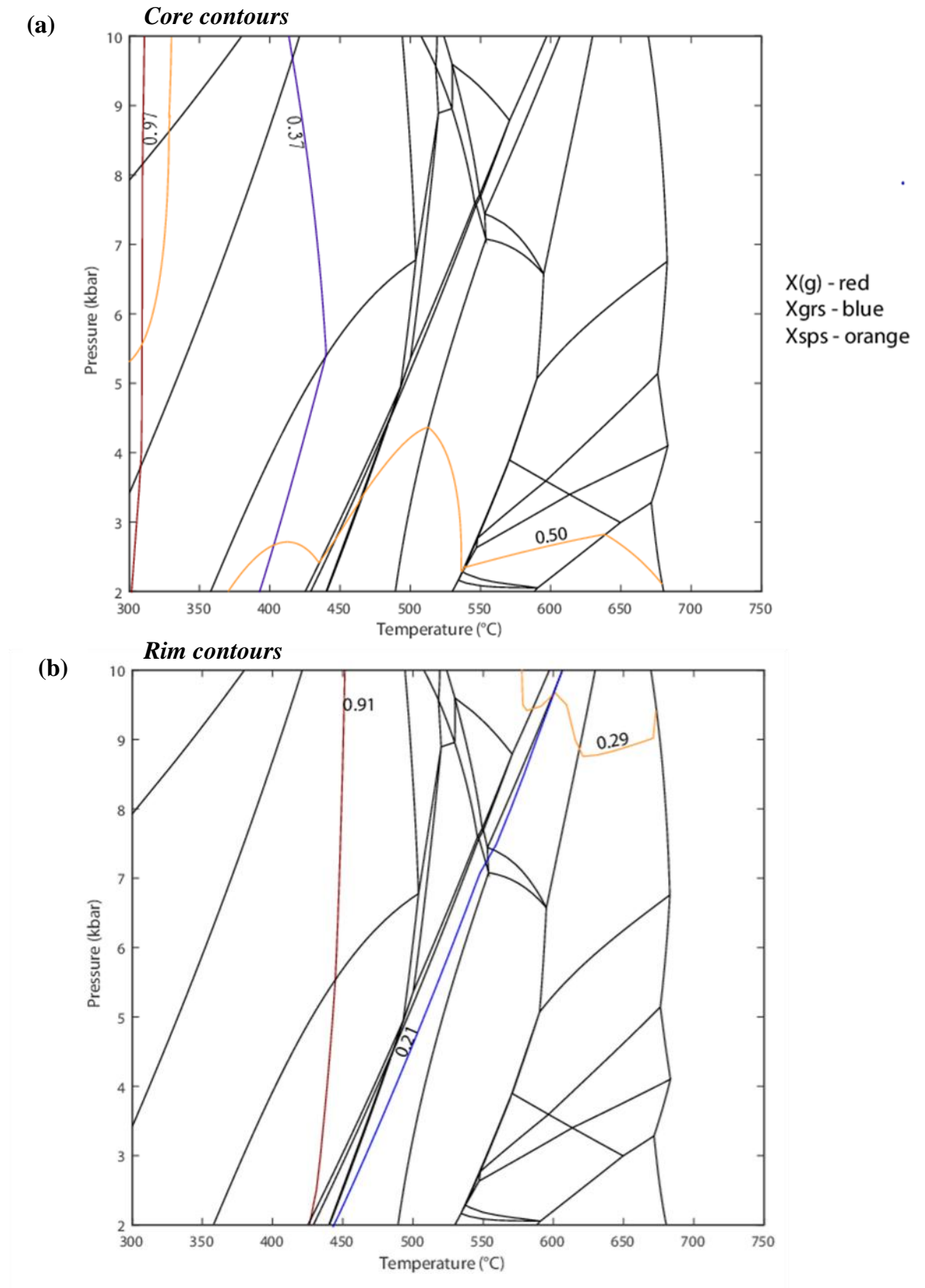
Figure 4.17. Garnet content of X_{sps} in orange, $x(g)$ in red and X_{grs} in blue (a) in core and (b) at rims.

Fernandes, J.

The peak field provides a broad constraint on the peak $P-T$ conditions (< 7.0 kbar and 490–595° C, Fig. 4.15). Figure 4.17 shows compositional contour intersections (values are from Table 4.3) for core and rim compositions of A12E. All the three contours $x(g)$, X_{sps} and X_{grs} do not intersect well enough to extract well defined $P-T$ conditions or a $P-T$ path with any certainty.
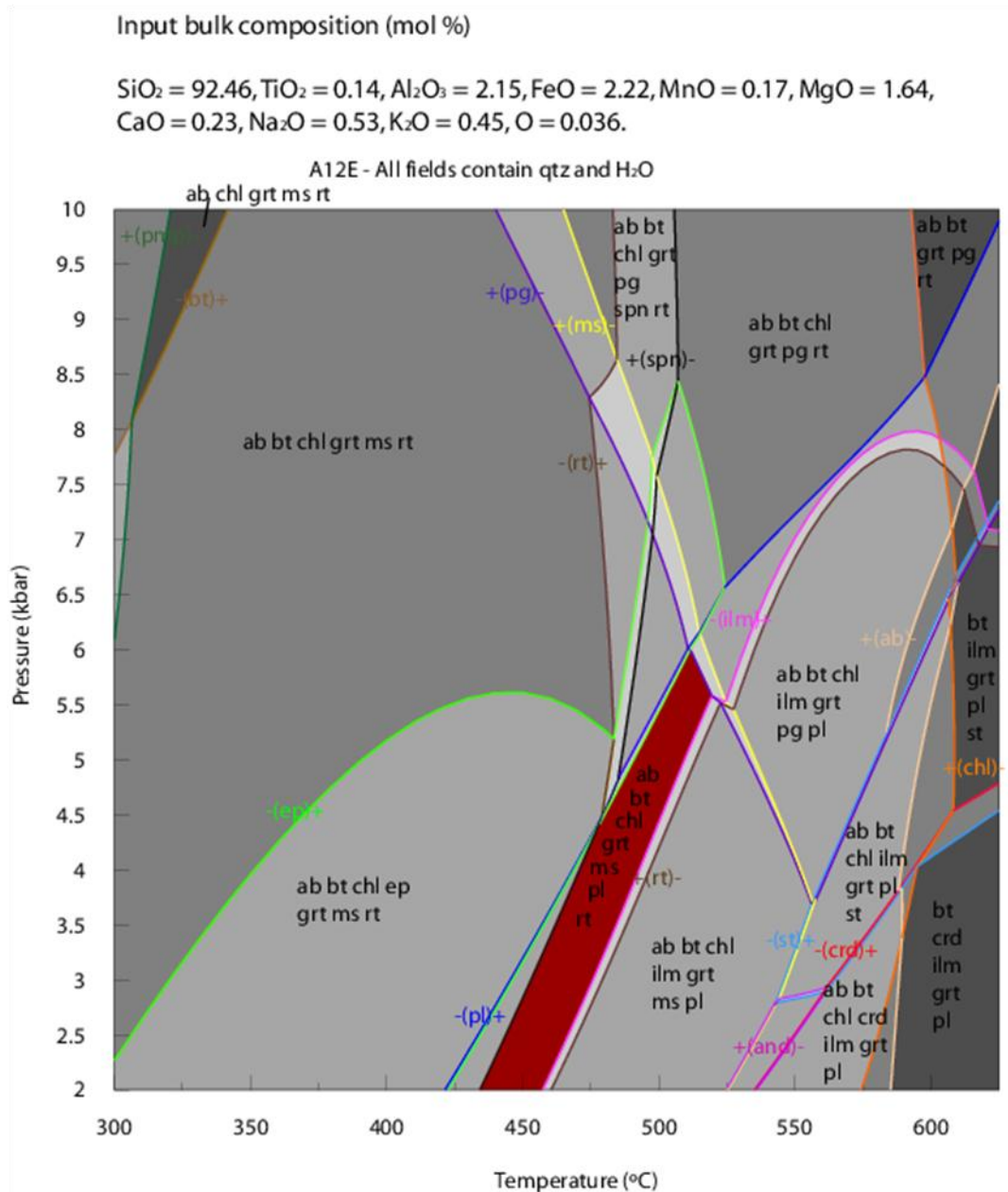
**Figure 4.18. Results for calculation of $P-T$ pseudosection for A12E using THERMOCALC,
with the garnet core composition removed from the bulk composition, for $XH_2O = 1.0$.
The closest matching assemblage is ab-bt-chl-grt-ms-pl-rt-q is highlighted in red.**

Fernandes, J.
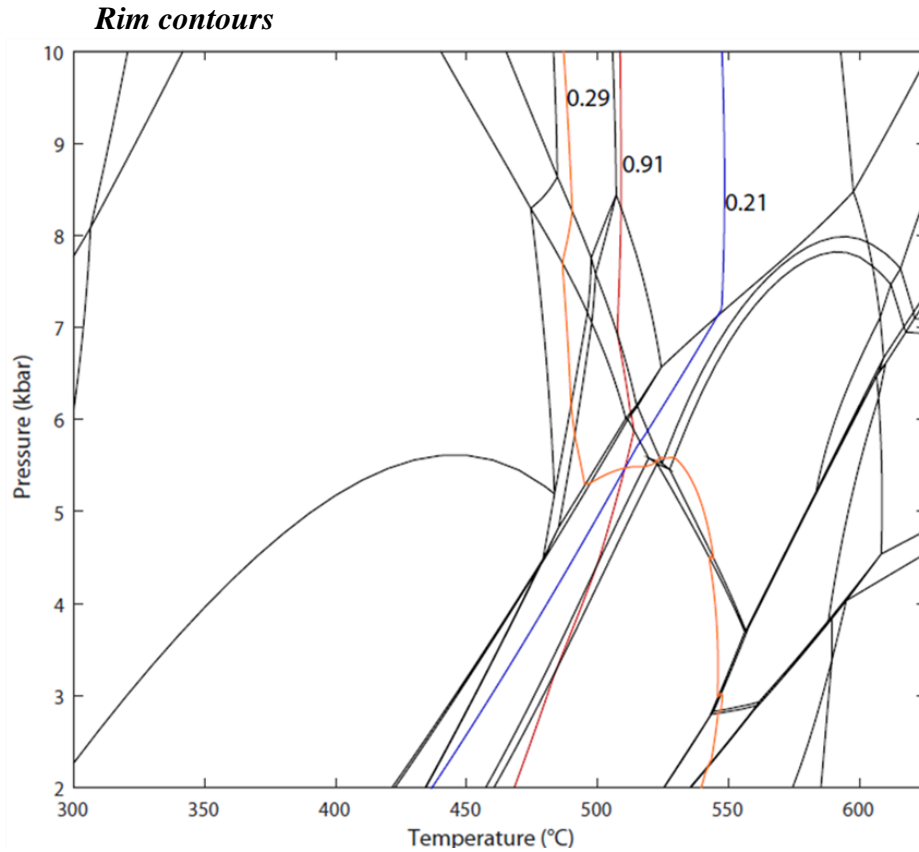
Rim contours

Figure 4.19. Contours for pseudosection without core in the bulk composition X_{sps} in orange, $x(g)$ in red and X_{grs} in blue(a) in core and (b) at rims.

For the texturally intricate and strongly zoned sample A12E, the bulk rock composition used for the thermodynamic forward modelling does not successfully represent the effective bulk composition in the parts of the rock containing the garnets studied here. In order to study the effects of garnet fractionation, calculations for sample A12E, without Mn-rich garnet cores in the bulk composition, have been carried out (Fig. 4.18) and composition contours for this pseudosection are presented in Fig. 4.19. An appropriate volume (Appendix 2) of the high Mn-garnet core components has been removed from the input bulk composition for the pseudosection (Fig. 4.18), to potentially obtain better constraints on the metamorphic conditions.

The closest matching assemblage to the observed rock assemblage in Fig. 4.18 is ab-bt-chl-grt-ms-pl-rt-q. The pseudosection predicts albite that is not observed in the rock. The $P–T$ constraints provided by this field are 430–530 °C and ≤ 6 kbar. The

Fernandes, J.

effect of fractionation of the field conditions push the field into slightly lower P–T conditions than the original prediction (< 7.0 kbar and 490–595 °C). The pseudosection without the core shows a perfect intersection providing rim (Fig 4.19) P–T estimates at 5.5 kbar and 510 °C.

Fernandes, J.

INTERPRETATION

Failure of the isopleths to constrain metamorphic conditions

Fractionation issues or suboptimal a-x models?

The initially calculated pseudosection (Fig. 4.15) provides only broad $P-T$ constraints. It predicts the observed rock assemblage, but fails to provide reliable $P-T$ constraints from garnet component contours.

The reason for the contour mismatch might be due to fractionation of elements by the garnet cores. Evidence for fractionation is in the strongly zoned garnet texture, the Mn-rich cores have locked up Mn in the garnet cores, fractionating it (Mn) out of the bulk composition. The bulk composition is more Mn rich than, and unrepresentative of the actual rock composition. This effect of fractionation has been considered, by removal of the garnet core content from the bulk composition and recalculation of the pseudosection (Fig. 4.18). The rim isopleths now intersect perfectly (Fig. 4.19), showing that the recalculated pseudosection (Fig. 4.18) is representative of the effective bulk composition. Hence, on the consideration of fractionation, the isopleths are able to provide $P-T$ conditions for the rim. The effects of fractionation only slightly affect the boundaries of the predicted assemblage field, but are able to provide tight constraints for rim contours.

On removal of the core composition (Fig. 4.18), the predicted peak assemblage is ab-bt-chl-grt-ms-pl-rt-q. Albite is stable in the identified peak assemblage, but does not appear in the rock. The identified plagioclase is the Ca-bearing, but especially Na-rich oligoclase. The problem is that the bulk composition for A12E has a high Na content (Table 4.0) that stabilizes the albite to in the peak field, causing the field mismatch.

Alternatively, it may be possible that the $a-x$ models fail to provide a good $P-T$ conditions for the core and rim, at the Mn content of this sample (core = 0.50, rim = 0.29; Fig. 4.17).

Since the recalculated pseudosection provides a precise, much improved, rim $P-T$ constraint of ~5.5 kbar and 510 °C (Fig. 4.19b). This shows that fractionation of the

Fernandes, J.

cores has definitely had an effect on the Mn budget in the bulk composition of the rock.

Mechanism for garnet nucleation

Sample A12E provides spectacular textural evidence for growth and nucleation processes. The two major controlling mechanisms are diffusion controlled nucleation and growth (DCNG) and interface controlled nucleation and growth (ICNG) (Ague & Carlson, 2013). ICNG is controlled mainly by rate of interface reaction. This process assumes an equal availability of growth material spatially. Due to the uniform availability of nutrients, nucleation centres are randomly spaced and are not influenced by pre-existing growth sites to grow off. If the growth mechanism is interface reaction or heat flow the size should be independent of the degree of isolation (Carlson & Denison, 1992). For nucleation by diffusion the garnet size is related to degree of isolation. Larger single garnet will grow to its size in isolation where it is free of competing crystals, whereas smaller nucleated garnet will occur with a number of similarly tiny garnets all competing for the same limited nutrients. The sizes of garnet in A12E are dependent on their spatial relationship with other garnet, where large garnet occur in isolation while small garnet occur as bands (Fig. 4.10a). The crystals are different sizes, large garnets grow at the expense of the smaller crystals and eventually the smaller garnet may coalesce, forming a single large garnet (Fig. 4.13a; Spear & Daniel, 1998). Therefore, the mechanism for nucleation and growth of garnet is diffusion controlled.

The nucleation sites in the phyllosilicate heterogeneous layers were more numerous, probably because elements necessary for garnet growth were available here, and because these layers may have been a location of higher deformational strain with higher energy that contributed to nucleation (Bell *et al.*, 1986; Spear & Daniel, 2001), compared to quartz layers. Several garnet nuclei grow as replacements over high chlorite and micas, which are more likely to overcome nucleation barriers than nucleation in the quartz bands (Bell *et al.*, 1986). Clustering of multiple nuclei require inhomogeneities in specific sites that favour nucleation (chlorite and mica rich bands, Spear & Daniel, 1998). Hence, there are more numerous nucleation sites in the phyllosilicate bands than in the quartz bands.

Fernandes, J.

Garnet growth zoning

The garnet in this rock shows that both large and small garnet are zoned (pink cores and blue rims, Fig. 4.13a and 4.14a). Diffusion is a function of the temperature that affected the rock during metamorphism (Zheng *et al*., 2002; Giletti, 2006). With *P–T* conditions of 5.5 kbar and 510 °C, assuming the rock was exposed to these conditions for 5 Ma the diffusion of Ca and Mn = 0.1 μm, Fe = 0 and Mg = 0.2 μm, which is negligible (calculations based on Carlson, 2006). Since both small and large garnet preserve zoning and have Mn-rich cores, temperatures were not high enough to reset the rock by diffusion and erase the early compositional zoning.

Some garnet appears unzoned (Fig. 4.12a). The apparently-unzoned garnet may have been sliced through the rim, rather than through the center. Alternatively, the garnet nucleated at a later time during the growth of other garnet rims and is unzoned. But since both, the small and large garnet generations preserve zoning (Mn-rich core) it is unlikely that any garnet is unzoned. Therefore, this must be an effect of slicing through a garnet rim (not representative of the compositional zoning) in making the thin section.

Garnet history

The garnet grains in Sample A12E, have textures that are useful for understanding their growth history. There appear to be two types of garnet based on size, the larger distinctly zoned garnets that have inclusions (Fig. 4.12a, 4.12d, 4.13a and 4.13d) and the smaller zoned garnets that are around the larger garnet or in bands (Fig. 4.10a). The relative timing of their growth is explored below.

The large and small garnets in A12E preserve compositional zones (Fig. 4.10a and b). Thin-section textures show that the large garnet occurs in isolation within the quartz layers while the small garnets occur as clusters. If the garnets grew at the same time and under similar conditions of *P–T* and chemistry, they will preserve a similar zoning pattern. This possibility assumes that the effective bulk composition for both the garnet were the same. However, the thin-sections (Fig. 4.10 and Fig. 4.12) show that the large and small garnet had different local growth conditions; larger garnet grew in isolation and the small garnet grew as clusters competing for nutrients. Figures 4.12 and 4.13a show a Mn-rich inner core, with smaller less Mn-

Fernandes, J.

rich cores that have nucleated around it, indicating that they grew under different compositions (lower in Mn content) at separate times.

Compositionally the abrupt change in zones (Fig. 4.13b) preserved indicates a gap in the garnet growth history, with early garnet core forming under conditions different from that at which the later garnet nucleated.

Arguing for an inherited core

The garnet image (Fig. 4.13a) shows multiple nuclei with a single rim grown around it. The inset SEM image shows the Mn-rich cores, and blue Fe-rich rims. The red boxes show secondary cores that have grown around the inner core. Analysing the compositional transect K-K' (Fig. 4.13b) in combination with the SEM compositional image (Fig.4.13a inset or Fig. 4.13a), it is clear that the inner core and the outer cores have different compositions. The SEM images show that the outer cores are less bright pink than the inner Mn-rich bright pink core. The composition of the inner core is $X_{sps} \approx 0.44–0.47$, $X_{grs} \approx 0.36–0.43$, $X_{alm} \approx 0.12–0.14$ and $X_{pyp} \approx 0.002–0.009$ whereas the secondary cores are $X_{sps} \approx 0.27–0.33$, $X_{grs} \approx 0.19–0.30$, $X_{alm} \approx 0.34–0.45$ and $X_{pyp} \approx 0.04–0.06$. Clearly the inner core has higher X_{sps} and X_{grs} contents than the secondary cores, while the secondary cores have higher X_{alm} and X_{pyp} contents. Characteristic growth profiles of garnet have an Mn bell shape (high Mn in the core, decreasing rimwards) and an increase in X_{alm} and X_{pyp} from core to rim (Tuccillo *et al*., 1990; Yardley, 1977).

On taking into consideration the effects of fractionation the rim has *P–T* conditions of ~510 °C/5.5 kbar (4.19a). Core nucleation occurred at sites where the local bulk composition differed (probably more Mn-rich), perhaps significantly, from the overall bulk rock composition and so it was not possible to obtain *P–T* conditions from the core. The inner core grew at a location when the effective bulk composition was probably significantly more Mn-rich, which suggests an early history for the core. Therefore the core is interpreted to be inherited from an early event and the rim grows under different conditions in a later event. The early low temperature core may have nucleated during the Otago metamorphism in the Jurassic (Adams& Robinson, 1993; Adams & Graham, 1997; Jugum *et al*., 2013) or during an early stage of the Alpine metamorphism in the Cretaceous (Grapes, 1995; Mortimer, 2000;

Fernandes, J.

Mortimer & Cooper, 2004; Vry *et al.*, 2004). The high *P/T* Otago metamorphism involved temperatures ~350–450 °C (greenschist facies, garnet-biotite zone, Yardley, 1982; Jamieson & Craw, 1987; Hay & Craw, 1993; Mortimer, 2000) and $X_{sps} = 0.54$ (garnet zone, White, 1996). Sample A12E has core $X_{sps} = 0.5$ (Table. 4.3); and may represent early core growth from the Otago event.

Hence metachert A12E preserves a polymetamorphic history within its garnet textures. The garnet grew in two distinct stages; the cores nucleated early, in Mn-rich bulk composition; and, the cores started growing at a later time, in a bulk composition less Mn-rich than the cores. The peak *P–T* conditions were 510 °C / 5.5 kbar.

Summary

A tight *P–T* constraint is only possible for the rim, not the core, since the garnet core composition contours *x(g)*, X_{grs} and X_{sps} do not all intersect. Removal of material contained in the cores of the large garnets from the effective bulk composition allows the rim *P–T* conditions to be tightly constrained. The *P–T* results obtained here for the rim (~510 °C/~5.5 kbar, Fig. 4.19b) provide a much tighter constraint on the metamorphic conditions, compared to results of previous traditional *P–T* results for this sample area (420–600 °C/5.9–13 kbar; Pepper, 2000). From the predicted metamorphic conditions, the core nucleation and rim formation occurred during separate metamorphic events; the core probably in the Jurassic and the rim in the Cretaceous. Fractionation has affected the effective bulk composition of this sample and has been dealt with appropriately; work on this sample exemplifies the use of pseudosections to constrain *P–T* conditions, after proper evaluation of a rock even with a complex history.

Fernandes, J.

SAMPLE AMS01 (VUW 43156)

RESULTS

Mineral assemblages and textures

Thin-section petrography

Photomicrographs show the mineral assemblage of sample AMS01 in Fig. 4.20. AMS01 is a fine grained metachert composed of layers of quartz and layers of garnet (Fig. 4.20a and b), both interleaved with mica. Quartz ranges in size from 30–700 µm and garnets grow up to 400 µm in diameter. The mica (Fig. 4.20c and d) includes both biotite that occurs as flakes up to 500 µm long, and muscovite up to 2 mm long and 40 µm thick. Chlorite occurs intergrown with the micas (Fig. 4.20c and d), plagioclase grains are large up to 1mm, and apatite and rutile (Fig. 4.20 g and h) occur as accessory minerals. Figures 4.20c and d show plagioclase porphyroblasts bordered by the micas, muscovite and biotite, around the top and a garnet band that has curved around the bottom of the plagioclase grain. Figures 4.20e and f, show larger (up to 400 µm) garnets grown in isolation of each other as well as garnets that comprise a band. The observed assemblage by microscopy is ap-bt-chl-grt-ms-pl-rt-q.

There is no µXRF or SEM mapping available for this sample, so this section is followed by EPMA of garnet.
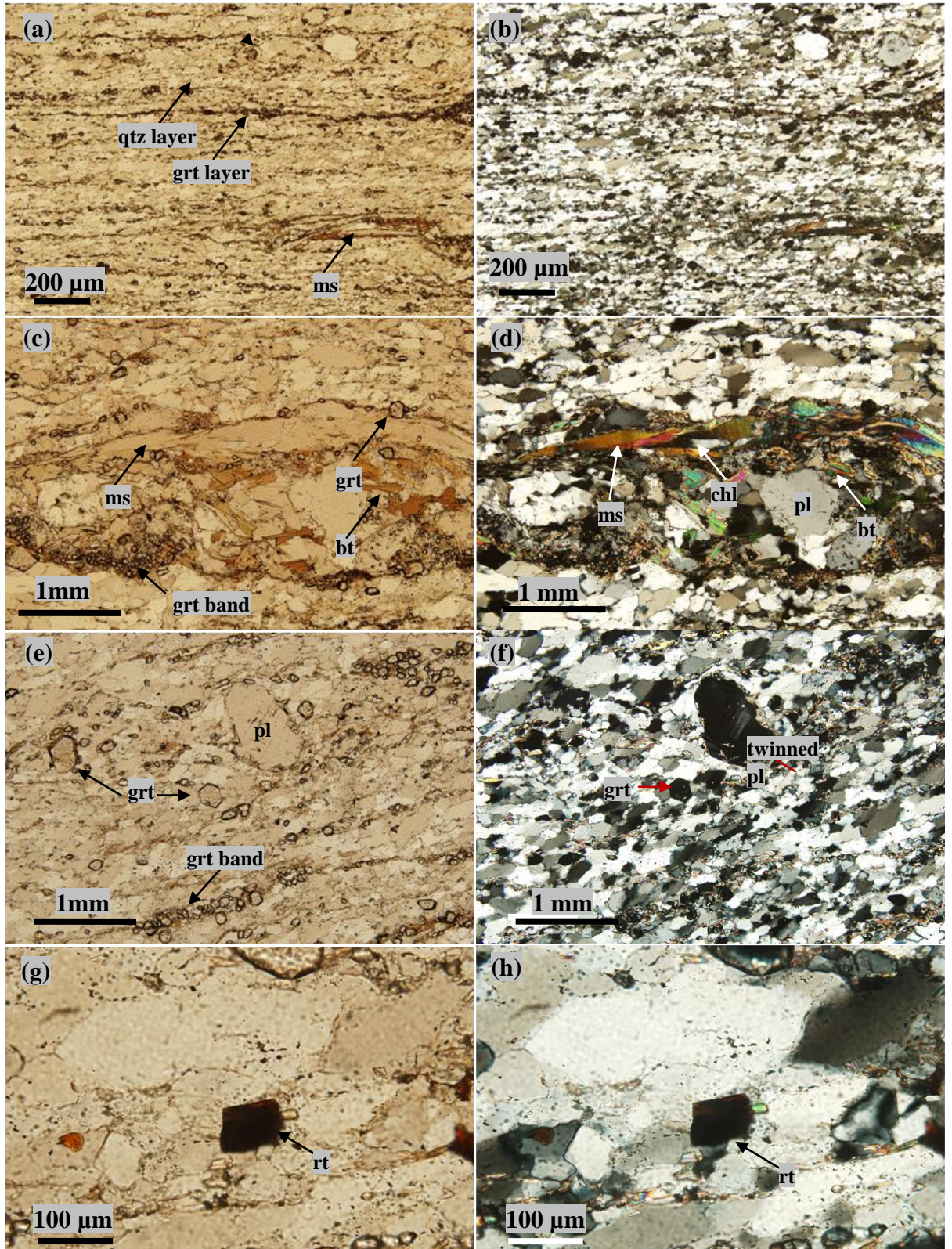
Figure 4.20. Thin section of AMS01showing a, c, e and g in plane illumination and b, d, f and h in crossed polarised illumination. Figure 4.20a and b show the fine grained nature of the rock. Panels c, d, e and f show the rock assemblage.

Fernandes, J.

Electron Probe Micro-Analysis (EPMA)

Energy dispersive spectroscopy identified epidote, oligoclase, and albite, in addition to quartz, garnet, muscovite, biotite, apatite, rutile and chlorite as the peak assemblage. Figure 4.21a shows a subtly zoned garnet crystal ~100 μm in diameter, within the quartz matrix. Garnet analyses were obtained using WDS methods. The representative results are presented in Table 4.4 and Fig. 4.21a and 4.21b. Transects are divided into core (pink), transition zone (yellow) and rim (blue) (Fig. 4.21b). The transition zone (lighter grey than core in Fig. 4.21a) is an intermediate zone between the core and rim and shows an X_{grs} depression (Fig. 4.21b and 4.21c). Apart from this depression of X_{grs} values the garnets are nearly compositionally level. Although the BSE images show zonation of the garnet, this is not reflected in their chemistry (Fig. 4.21a and b). The garnets have Fe rich compositions from core to rim demonstrated by the high X_{alm} values (Fig. 4.21b and c).

In the D1-D1' transect (Fig. 4.21b), the core has composition $X_{alm} \approx 0.42–0.44$, $X_{sps} \approx 0.28–0.31$, $X_{grs} \approx 0.19–0.21$ and $X_{pyp} \approx 0.07$ (Fig.4.21b); the transition zone has $X_{alm} \approx 0.43–0.44$, $X_{sps} \approx 0.30–0.31$, $X_{grs} \approx 0.14–0.20$ and $X_{pyp} \approx 0.07–0.08$, and the rim has $X_{alm} \approx 0.42–0.44$, $X_{sps} \approx 0.29–0.33$, $X_{grs} \approx 0.18–0.20$ and $X_{pyp} \approx 0.06–0.10$. Transect E1-E1' (Fig. 4.21a) across the same garnet shows similar compositional patterns as D1-D1'. The transects have Fe- and Mn-rich cores, with $X_{alm} \approx 0.42–0.44$, $X_{sps} \approx 0.28–0.30$, $X_{grs} \approx 0.19–0.21$ and $X_{pyp} \approx 0.07$. The transition zone has $X_{alm} \approx 0.43–0.46$, $X_{sps} \approx 0.28–0.32$, $X_{grs} \approx 0.13–0.21$ and $X_{pyp} \approx 0.07–0.09$ and the rim has $X_{alm} \approx 0.41–0.45$, $X_{sps} \approx 0.28–0.34$, $X_{grs} \approx 0.16–0.21$ and $X_{pyp} \approx 0.06–0.08$. The main compositional variation is the Ca depression to $X_{grs} \approx 0.13–0.14$. The Ca low is balanced by corresponding Mn and Fe elevations to $X_{sps} \approx 0.31–033$ and $X_{alm} \approx 0.46$. Representative values for zones of transect D1-D1' are presented in Table 4.4.

Fernandes, J.
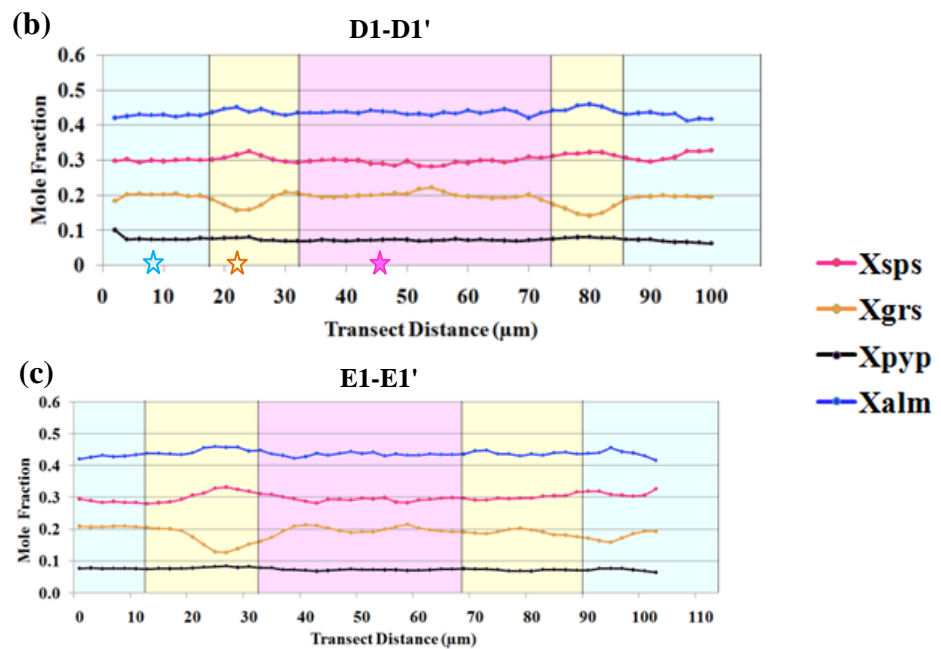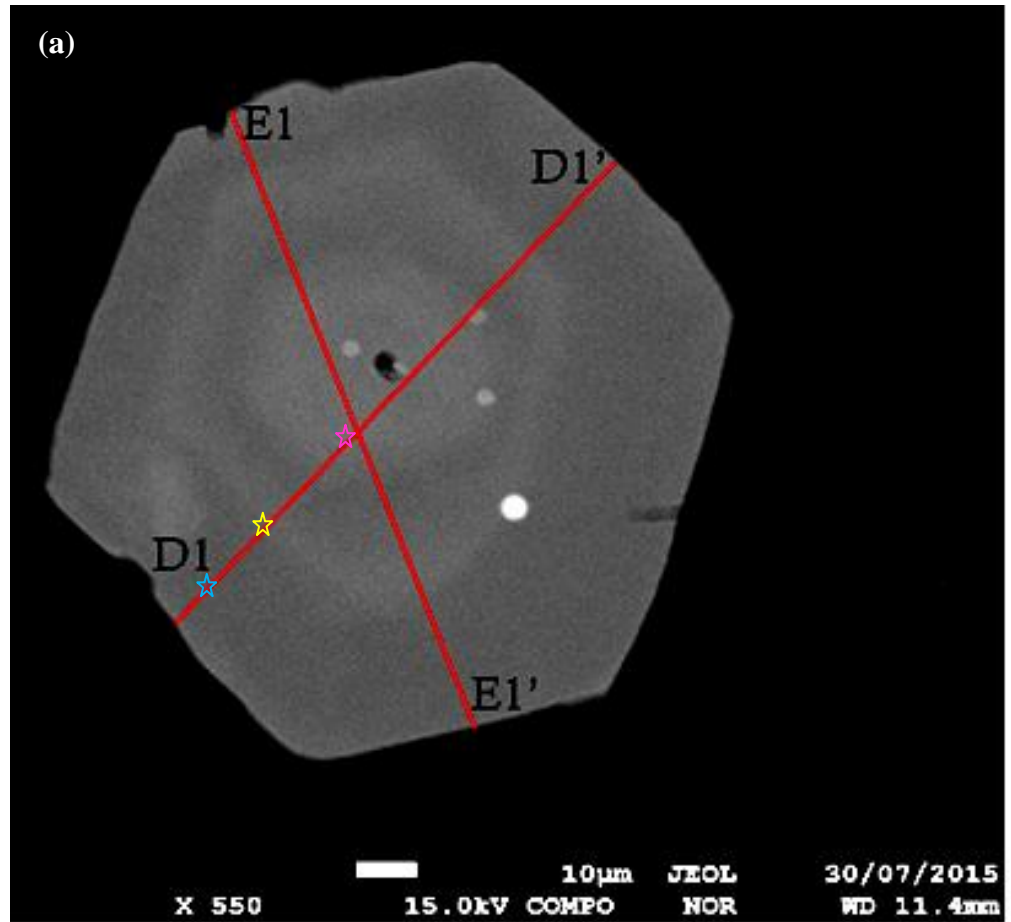
Figure 4.21. BSE image of AMS01 showing concentrically zoned garnet. The results of garnet composition data from EPMA along transects D1-D1' and E1-E1' are presented. The stars in Fig. 4.20a and b correspond to values from Table 4.4.

Fernandes, J.

Table 4.4. Representative EPMA garnet compositions for AMS01.

Oxide wt%

	☆ Rim	☆Transition	★Core
SiO_2	36.95	37.09	36.25
Al_2O_3	21.15	21.20	19.89
TiO_2	0.02	0.01	0.20
MgO	1.86	1.99	1.87
FeO_{total}	19.63	20.57	20.41
MnO	13.39	14.17	13.32
CaO	7.21	5.58	7.32
Cr_2O_3	0.00	0.02	0.02
Total	100.21	100.64	99.28

Normalised to 8 cations

Si	2.95	2.96	2.93
Al	1.99	1.99	1.90
Ti	0.00	0.00	0.01
Mg	0.22	0.24	0.23
Fe_{total}	1.31	1.37	1.38
Mn	0.91	0.96	0.91
Ca	0.62	0.48	0.63
Cr	0.000	0.00	0.00

x(g)			
=Fe/(Fe+Mg)	0.86	0.85	0.86
m(g)=X_{sps}	0.30	0.31	0.29
z(g)=X_{grs}	0.20	0.16	0.20
X_{pyp}	0.07	0.08	0.07
X_{alm}	0.43	0.45	0.44

Rim content: x(g) = 0.86, m(g) = 0.30, z(g) = 0.20 used in Fig.4.24a.
Core contents: x(g) = 0.86, m(g) = 0.29, z(g) = 0.20 used in Fig.4.24b.
The stars correspond to Fig. 4.21a transect D1-D1'

Fernandes, J.

Petrographic Forward Modelling

P–T pseudosection

Input bulk composition (mol %)

$SiO_2 = 93.61$, $TiO_2 = 0.10$, $Al_2O_3 = 1.91$, $FeO = 1.15$, $MnO = 0.77$, $MgO = 1.06$,
$CaO = 0.67$, $Na_2O = 0.42$, $K_2O = 0.30$, $O = 0.08$.

**Figure 4.22. Results for AMS01 *P–T* pseudosection calculations with *X*H₂O = 1.0, using
THERMOCALC. The matching field to the peak assemblage ab-bt-chl-ep-grt-ms-pl-rt-q is
highlighted (red).**

Fernandes, J.

Figure. 4.22 shows a *P–T* pseudosection for AMS01, within which lies the peak assemblage field (red), bordered by the pl-out, ep-out and spn-in lines. The observed peak assemblage q-ab-bt-chl-ep-grt-ms-pl-rt is predicted by the pseudosection. The *P–T* conditions that match the peak assemblage form a thin field extending from 2–8.7 kbar and 440–575 °C. The following section uses garnet composition contours in combination with real rock data in an attempt to more tightly constrain the core and rim conditions.

Contoured sections

Figure 4.23 shows contoured pseudosections for AMS01 garnet mode, X_{sps}, $x(g)$ and X_{grs} produced using TCInvestigator v1.02 (Pearce *et al.*, 2015). Figure 4.24 shows core and rim compositions of AMS01 (values from Table 4.4). The composition contours do not all intersect and do not further constrain the *P–T* conditions for this sample with any certainty, mainly due to the large mismatch between the isopleths for X_{sps} and the other garnet composition isopleths. The $x(g)$ contour provides a temperature > 475 °C. The X_{grs} and $x(g)$ contours intersect in both core (3.5 kbar and 475 °C, Fig. 4.24a) and rim (3 kbar and 475 °C, Fig. 4.24b), but the X_{sps} contour does not intersect either of them. The X_{grs} and $x(g)$ contour intersections for the core is 0.5 kbar greater than the rim, suggesting that the cores and rims grew under similar conditions.

Fernandes, J.

Garnet mode

(a)

(b) X_{sps}

Fig. 4.23 (cont'd)

Fernandes, J.

(c) *x(g)*
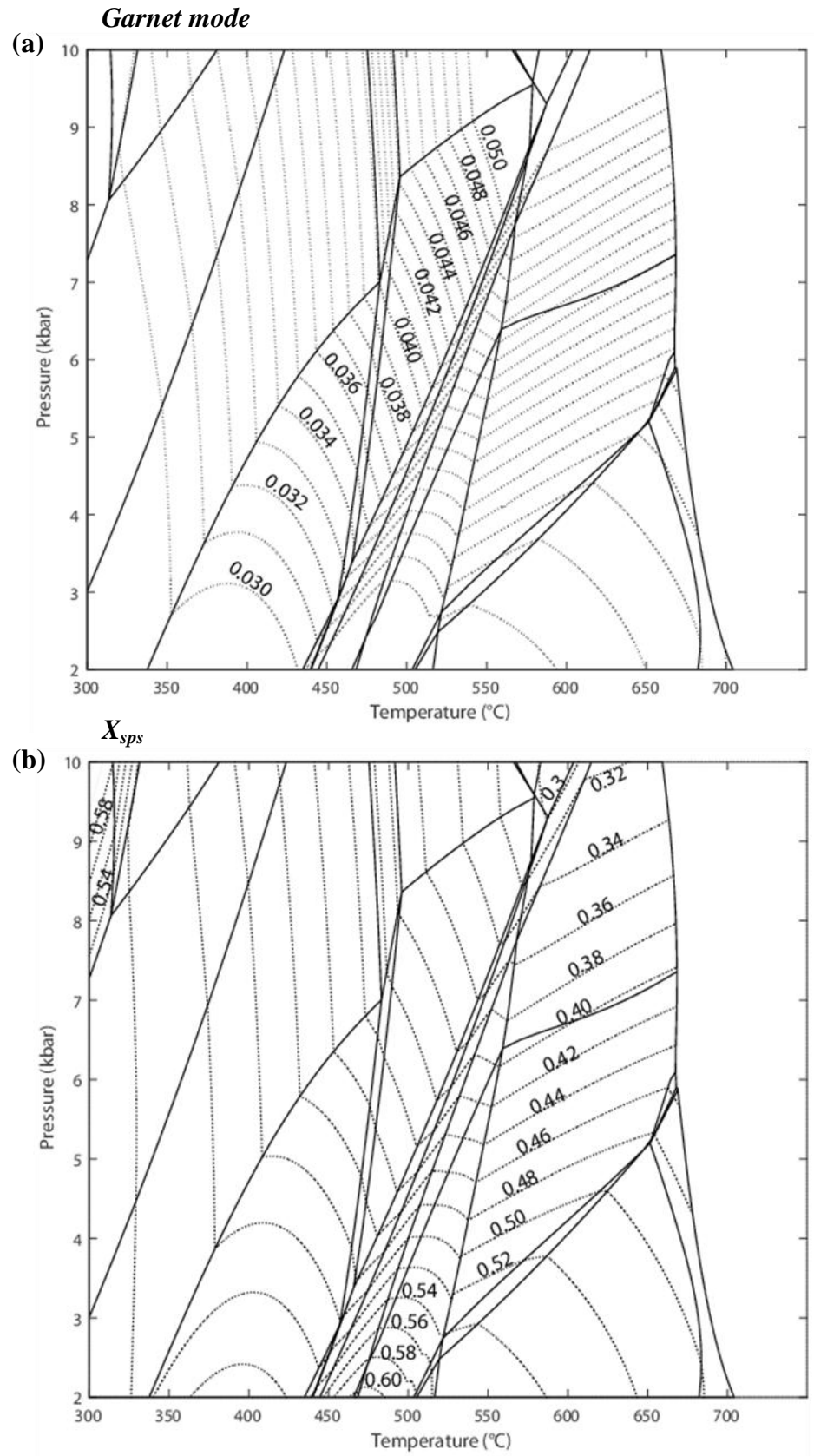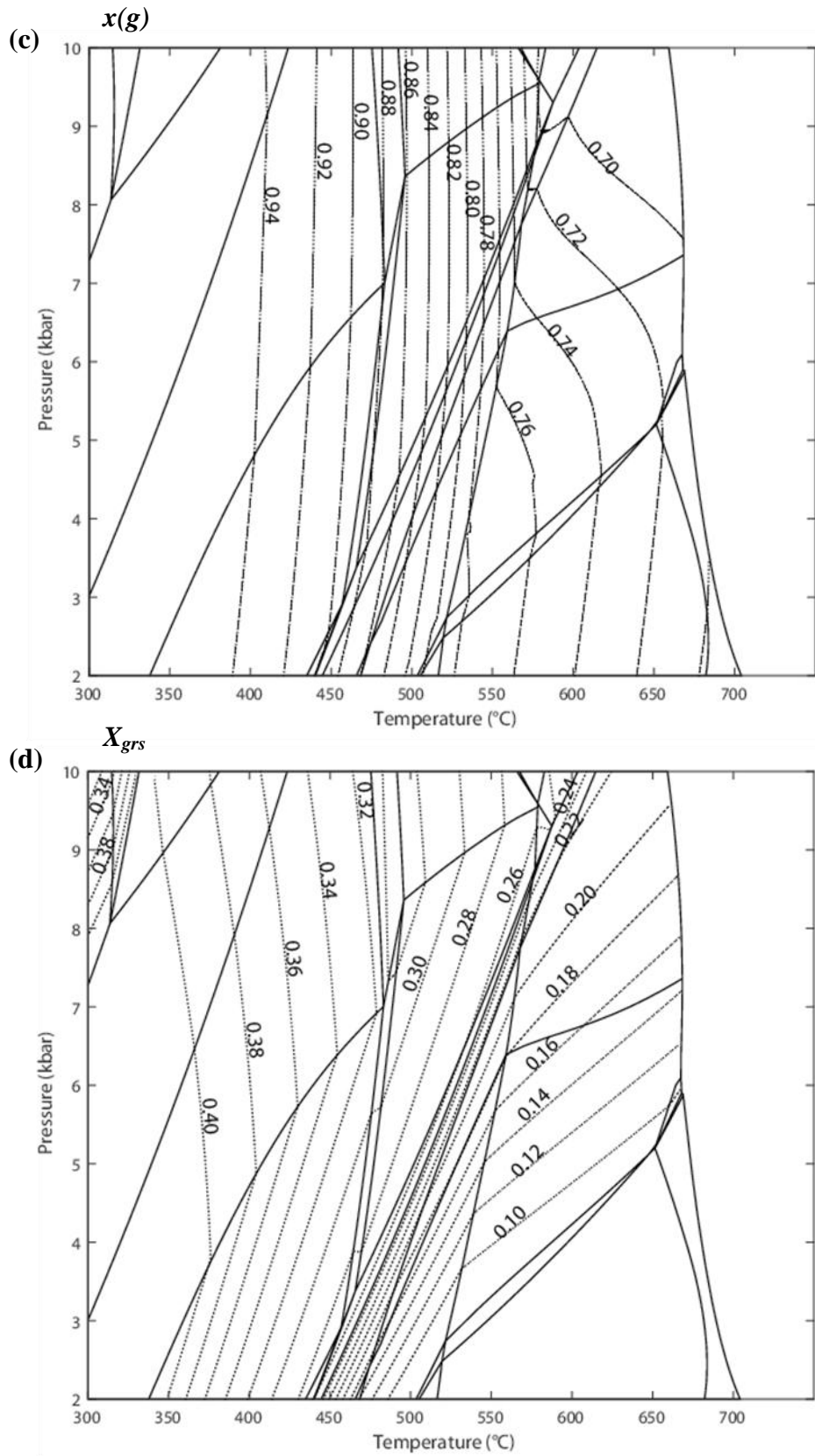
(d) X_{grs}

Figure 4.23. *P–T* **pseudosection for AMS01 contoured for (a) garnet mode, and garnet compositions (b)** X_{sps}**, (c)** *x(g)***, and (d)** X_{grs}**.**

Fernandes, J.

(a) *Core contours*

(b) *Rim contours*
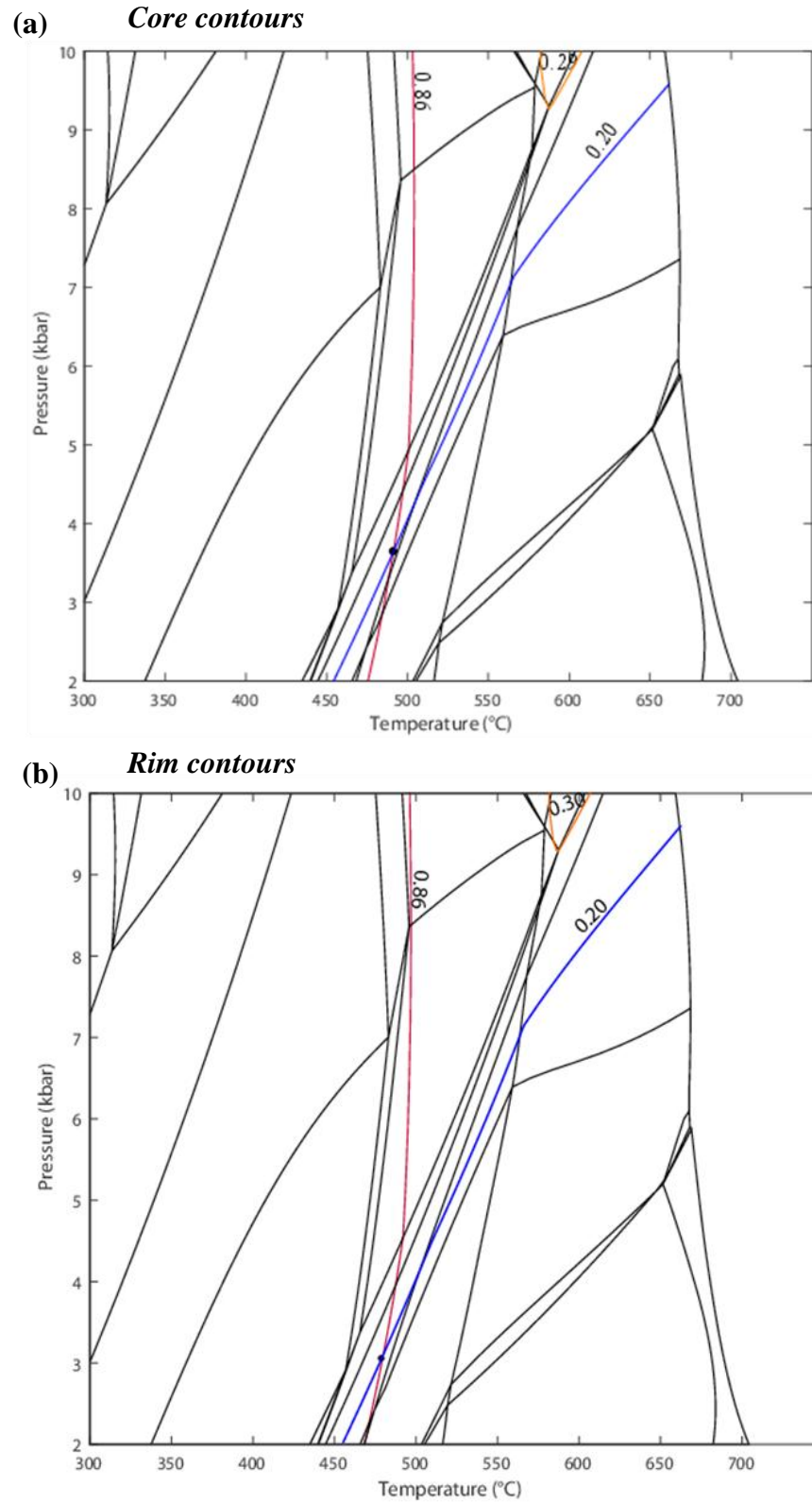
Figure 4.24. Garnet content of X_{sps} in orange, $x(g)$ in red and X_{grs} in blue (a) in core and (b) at rims.

INTERPRETATION

The observed peak assemblage (ab-ap-bt-chl-ep-grt-ms-pl-rt-q) is present on the pseudosection (Fig. 4.22), with *P-T* conditions ranging from 2–8.7 kbar and 440–575 °C.

Garnet X_{sps} contour mismatch

The garnet contours X_{sps}, X_{grs} and $x(g)$ do not all intersect (Fig. 4.24a and b). The X_{sps} contour does not intersect X_{grs} or $x(g)$ contour.

The mismatch of the contours may be explained as follows:

(1) **Bulk composition issues**: The bulk composition used for pseudosection calculations for did not mimic the effective bulk composition of the locality in which the analysed garnet was, hence the isopleths failed to constrain $P-T$ conditions.

(2) **Reaction overstepping:** The X_{grs} and $x(g)$ contours intersect, in the ab-bt-chl-grt-ms-pl-rt-q field ~10 °C up-*T* from the peak field (ab-bt-chl-ep-grt-ms-pl-rt-q). It is possible that the garnet nucleation could have been hindered by sluggish kinetics (Rubie, 1998), resulting in some amount of reaction overstepping.

(3) **Mn *a-x* modelling not optimised**: It is observed that for this sample, X_{sps} contours (X_{sps} = 0.29–0.30, Fig. 4.24) fail to appropriately help constrain $P-T$ conditions, in the rim and the core (Fig. 4.24). It may be possible that the activity models for Mn-bearing minerals like garnet still need refining.

Garnet growth

Garnet preserves in its textures evidence to understanding its growth mechanism, as discussed previously for sample A12E. The garnets are numerous and have minor compositional variation. Some garnets are larger and occur in isolation from the clusters of little garnets, free of competing crystals (Fig. 4.10e and f). The little garnets occur as bands, probably limited in their growth by competing nuclei. Garnet texture of this type suggests that the growth mechanism for the garnet was diffusion controlled (Carlson & Denison, 1992; Ague & Carlson, 2013).

Fernandes, J.

Garnet history

Clues to the metamorphic history of AMS01 are preserved in the rock texture and the garnet compositional zoning. The presence of the Ca depression to $X_{grs} \approx 0.13{-}0.16$ in the transition zones suggest a temporary reduction in the availability of Ca in the supply of nutrients. There is no textural evidence for disequilibrium such as the presence of retrogression, a fluid phase, corroded rims, microstructural discontinuities or compositional variation (Koons *et al*., 1987; Ernest & Frost, 1988; White *et al*., 2008). This suggests that the garnet had no interruptions to its growth. This evidence is consistent with a single episode of garnet growth, over almost similar temperature conditions and a narrow range of pressure conditions. Hence, the garnets within AMS01 are inferred to preserve evidence from a single metamorphic event.

Fernandes, J.

SAMPLE J36 (28701)

RESULTS

Mineral assemblages and textures

Thin-section petrography

Images representative of Sample J36 show a fine grained rock that is mainly composed of quartz and garnet that occur as distinct bands that have been folded (Fig. 4.25a, b, c, d, e and f). Quartz ranges in size from 100–800 µm. The garnets are mostly small, < 150 µm in diameter. Locally, clusters of rutile surround garnet in the densely populated bands of tiny garnet (Fig. 4.25a, b; see also Fig. 4.26a, 4.28a). Both biotite (Fig. 4.25e and f) and a white mica (Fig. 4.25g and h) define a foliation. The biotite books are up to 40 µm thick and 360 µm long. The white mica occurs less abundantly with a maximum thickness of 10 µm and 80 µm in length, within the quartz matrix (Fig. 4.25c). Minor minerals, primarily rutile (Fig. 4.25a and b), chlorite (Fig. 4.25g and h) and apatite (Fig. 4.25i and j), are present in the rock. Pyrite is identified as a trace mineral by SEM based composition maps (blue green, Fig. 4.27c).

Fernandes, J.

Fig. 4.25 (contd.)

Fernandes, J.
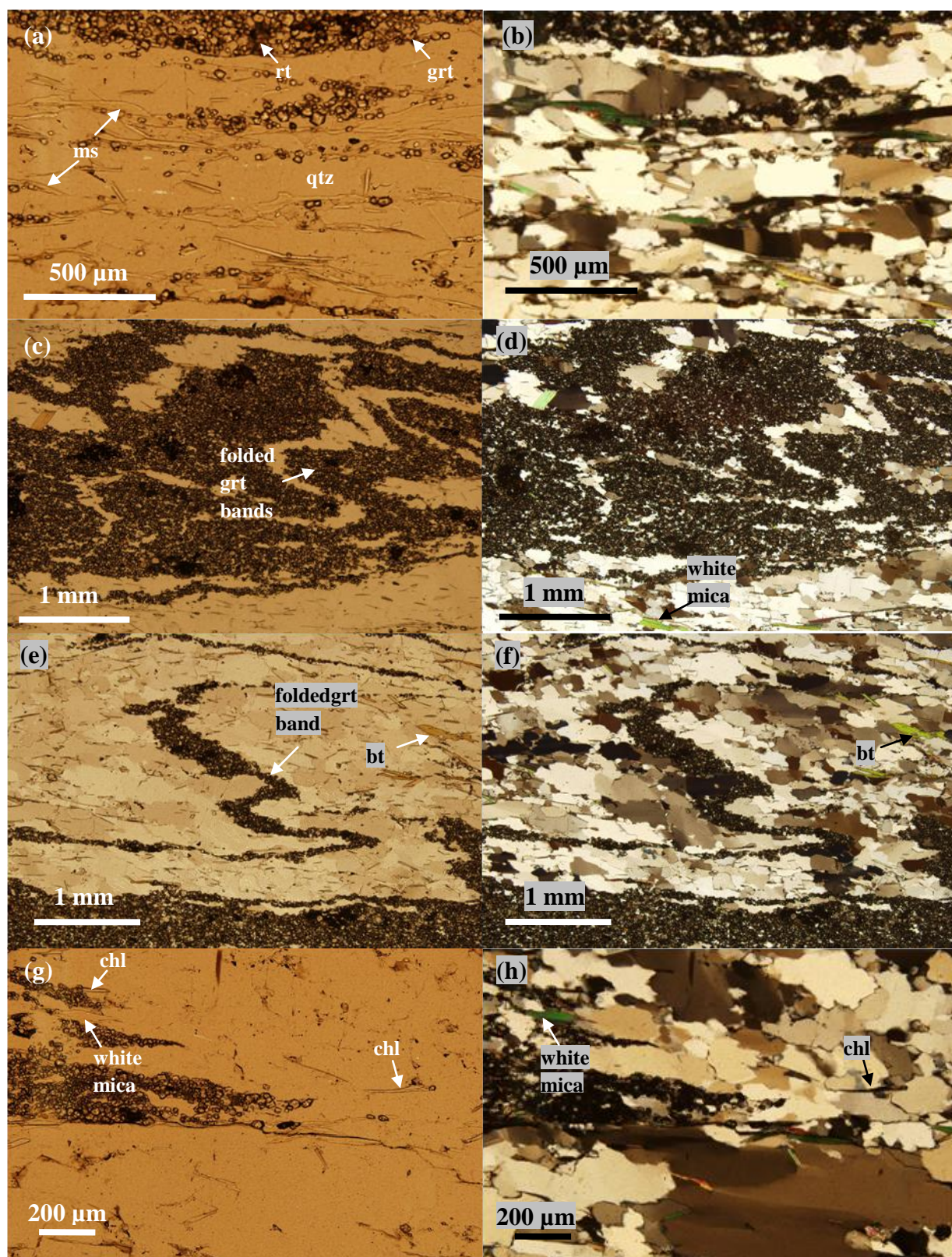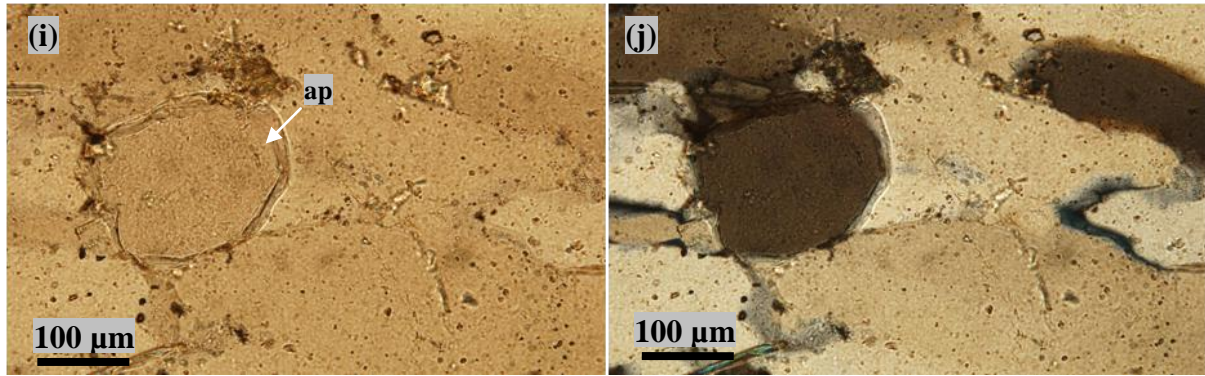
Figure 4.25. Representative photomicrographs of sample J36 (panels a, c, e, g and i: plane polarized illumination; panels b, d, f, h and j: cross-polarized illumination). Panels a, b c, d, e & f show the fine grain size of garnet and quartz that occur as folded bands. Panel 1a–j shows the labelled rock assemblage.

Micro X-ray fluorescence composition maps

The µXRF maps show the distribution of elements in the rock on the thin-section scale (Fig. 4.26). Minerals can be identified by using µXRF maps in combination with mineral formulae (Table 4.1).

The thin section shows evidence for folding in the garnet and quartz bands (Fig. 4.26a, b and c). Figure 4.26 shows that the thin section is fine grained, tightly folded, mainly comprised of quartz and densely populated garnet bands. Clumps of rutile (Fig. 4.26a, red) occur in the garnet-rich bands, and have been involved together with garnet in the folding (red in Fig. 4.26b). The scattered micas are aligned to form a weak axial-planar foliation. Minor apatite (Fig. 4.26c, yellow) is scattered throughout the rock.

Fernandes, J.
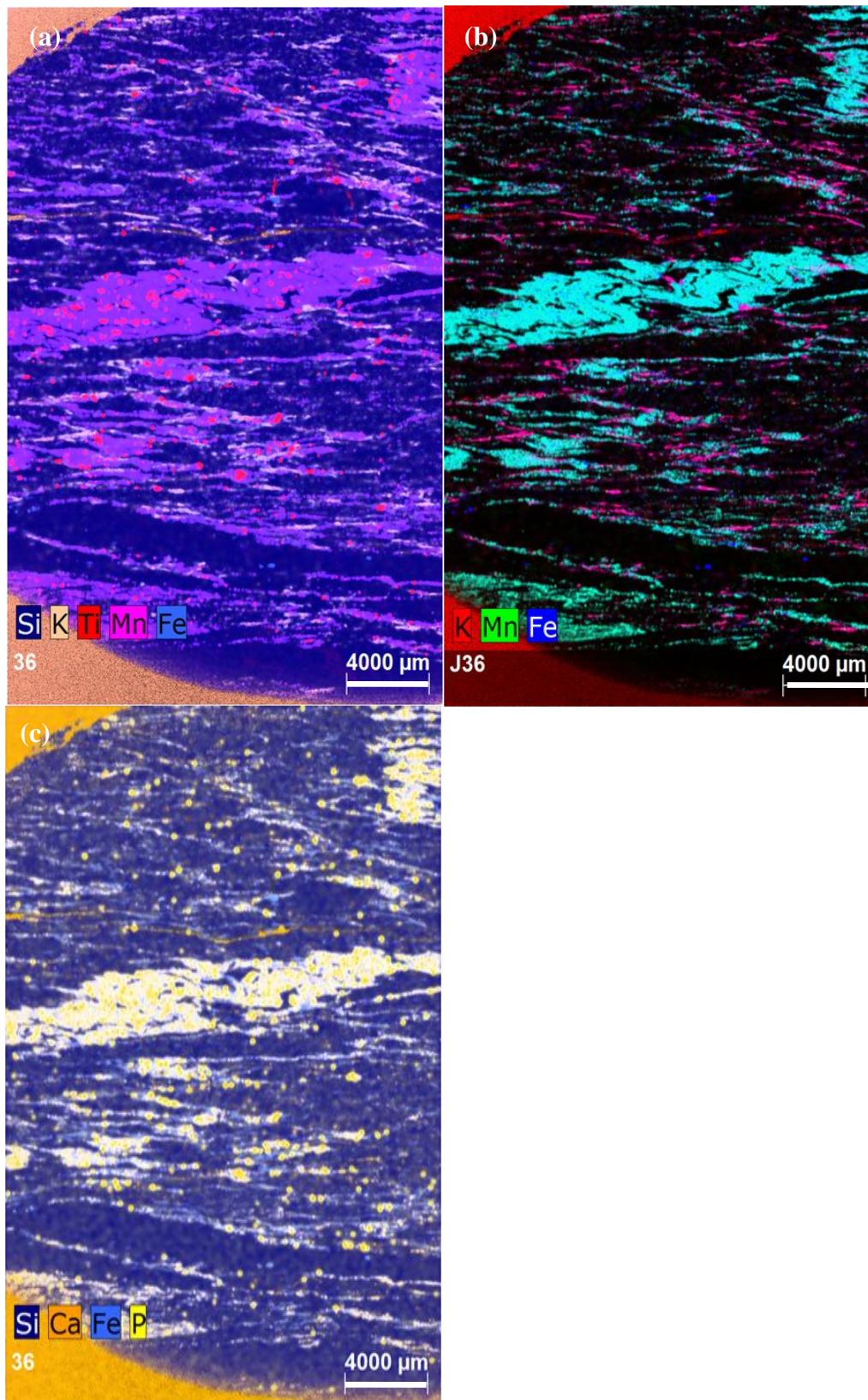
Figure 4.26. XRF maps showing compositional layering and folding in J36. (a) Mn and Fe-rich garnet layers (purple) with associated rutile (red). (b) K-rich layers showing mica (red) and Mn-rich layers indicating garnet (green). (c) Apatite (yellow) occurs throughout the thin section.

Scanning Electron Microscopy (SEM)-based composition maps
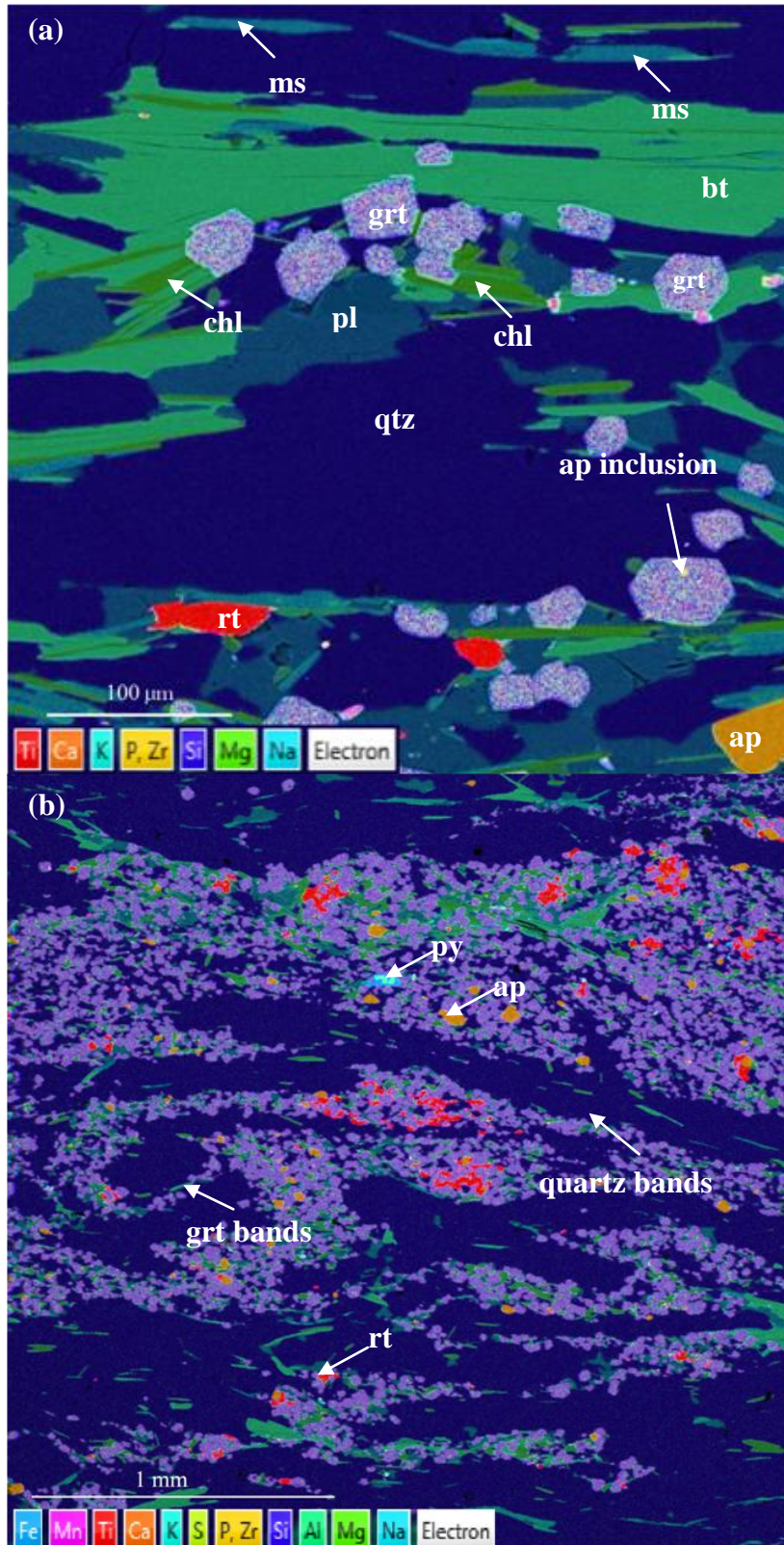
Figure 4.27. SEM composition maps of J36 show mineral — quartz (dark blue) and biotite (dull green), chlorite (bright green), muscovite (blue-green), apatite (orange), plagioclase (dull blue) accessory rutile (red) and trace pyrite (blue-green) a) Close-up view and b) shows the evidence of folding in the rock.

Fernandes, J.

The garnets are numerous, well formed, and occur as densely populated bands (Fig. 4.27a and b). The close-up SEM-based element composition maps (Fig. 4.27) confirm the observations gained from the thin-section petrography and µXRF maps, and in addition show that this rock contains plagioclase feldspar (Fig. 4.27a). Pyrite occurs as a trace mineral (Fig. 4.27c).

Electron Probe Micro-Analysis

Energy dispersive spectroscopy (EDS) results confirmed the assemblage present. The plagioclase was identified as oligoclase and the white mica was confirmed to be muscovite. Other white micas were looked for, in particular, the Ca-mica margarite, which was not found. The BSE image (Fig. 4.28a) shows that the garnets are subtly zoned and contain inclusions of quartz and rutile. Clumps of rutile grow around the garnet within the garnet bands (Fig. 4.28a).

Garnet analyses were obtained using WDS methods. The representative results are presented in Table 4.5 and Fig. 4.28a and b. Although the BSE images clearly show that the garnets are zoned, in terms of the chemistry, the EPMA data show that the zoning is subtle; the garnets are very nearly compositionally level.

The garnets have Fe rich compositions from core to rim demonstrated by the high X_{alm} values (Fig. 4.28b and c). Transect U-U' (Fig. 4.28b) has a core, a transition zone and a rim. The transition zone is the zone between the core and the rim, which appears as a lighter shade (yellow star, Fig. 4.28a) than the core on the BSE image, it has higher X_{grs} values than the core. In the U-U' transect (Fig. 4.28b), the core has composition $X_{alm} \approx 0.42–0.43$, $X_{sps} \approx 0.30–0.31$, $X_{grs} \approx 0.14–0.15$ and $X_{pyp} \approx 0.12$ (Fig. 4.28b); the transition zone has $X_{alm} \approx 0.41–0.44$, $X_{sps} \approx 0.29–0.31$, $X_{grs} \approx 0.14–0.18$ and $X_{pyp} \approx 0.11–0.12$ and rim has $X_{alm} \approx 0.40–0.42$, $X_{sps} \approx 0.29–0.34$, $X_{grs} \approx 0.15–0.20$ and $X_{pyp} \approx 0.09–0.11$. Transect T-T' (Fig. 4.28a) is across two juxtaposed garnets that show similar compositional zoning patterns (Fig. 4.28c). They have Fe- and Mn-rich cores, with $X_{alm} \approx 0.40–0.43$, $X_{sps} \approx 0.29–0.32$. The X_{alm} and X_{sps} decrease towards the rim, where $X_{sps} \approx 0.28–0.30$ and $X_{alm} \approx 0.40–0.42$. Grossular content in the core is $X_{grs} \approx 0.15–0.19$ and increases in the rim to 0.18–0.21. Pyrope (X_{pyp}) varies in content between 0.10–0.12 throughout the transect. The main compositional variation is in the Ca content of the garnet, with X_{grs} minimum in the core increasing slightly near the outer margin of the core region, varies in the transition zone and has a X_{grs} high of 0.18–0.2 in the rim. The variation in X_{grs} is balanced by changes in the proportions of the other garnet components, mainly X_{alm} and X_{sps}.

Fernandes, J.
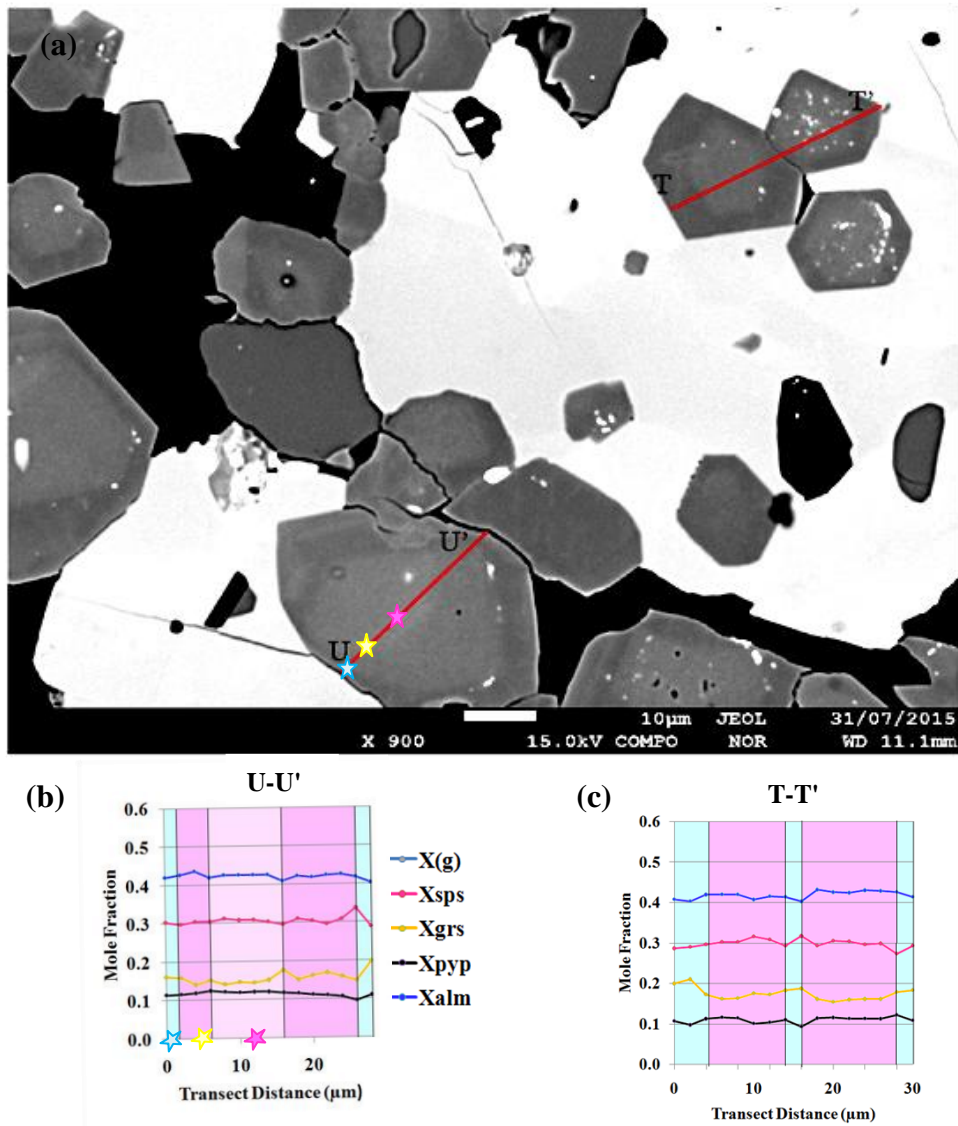
Figure 4.28. BSE image of J36 showing zoned garnet and the results of garnet composition analyses by EPMA along transects T-T' and U-U' are presented. (a) BSE Image, (b) Transect U-U' shows three zones, a core (pink), transition zone (dark pink) and a rim (blue). (c) Transect T-T' is across two garnets zoned into core (pink) and rim (blue). The stars correspond to representative EPMA values from Table 4.5.

The garnets have a Ca high of 0.18−0.20 towards very outmost parts of the garnet. They are mainly Fe-rich and show slightly elevated compositions for Fe and Mn components in the core that decrease in the rim.

Petrographic Forward Modelling

P-T pseudosection

Input bulk composition (mol %)

$SiO_2 = 89.23$, $TiO_2 = 0.37$, $Al_2O_3 = 3.11$, $FeO = 2.47$, $MnO = 1.49$, $MgO = 2.13$, $CaO = 0.87$, $Na_2O = 0.03$, $K_2O = 0.31$, $O = 0.02$.

J36 - All fields contain qtz and H_2O
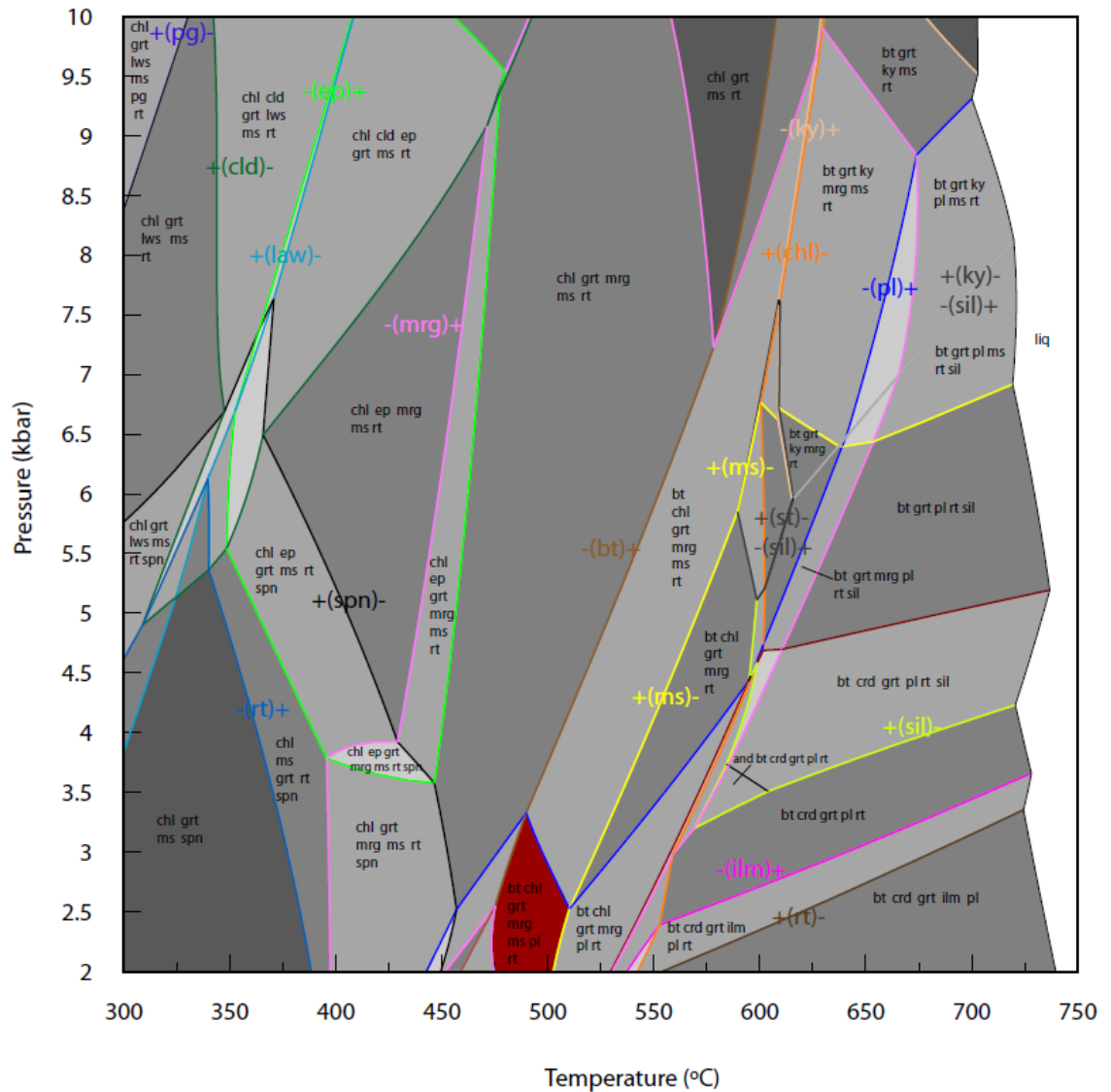
Figure 4.29. Results for J36 *P−T* pseudosection calculations with $XH_2O = 1.0$, using THERMOCALC. The closest matching field to the peak assemblage bt-chl-grt-ms-mrg-pl-rt-qtz is highlighted (red).

Fernandes, J.

The P–T pseudosection for J36 is presented in Fig. 4.29. The peak assemblage field that most closely corresponds to the observed assemblage shaded in red (grt-bt-chl-ms-mrg-pl-rt). There is no field on the pseudosection that exactly matches the observed rock assemblage. The absence of margarite in the observed assemblage and its presence in the pseudosection will be discussed later (See '*Peak field mismatch*' under 'INTERPRETATIONS' below). The plagioclase-in line does not progress smoothly up through the diagram, as it does in the pseudosection for A12E but instead zigzags before progressing up-P at relatively high-T. The closest matching field (red on Fig. 4.29) provides P–T conditions of ≤ 3.4 kbar and 475–510 °C. The following section uses garnet composition contours in combination with real rock data in an attempt to more tightly constrain the core and rim conditions.

Contoured sections

Fig. 4.30 shows contoured pseudosections for J36 garnet mode, X_{sps}, $x(g)$ and X_{grs} produced using TCInvestigator v1.02 (Pearce *et al.*, 2015).

Figure 4.31 shows core and rim compositions of J36 (values from Table 4.5). The intersection of composition contours does not lie in the bt-chl-grt-mrg-ms-rt-pl field (red, Fig. 4.29) but in the bt-chl-grt-mrg-ms-rt field. The X_{sps}, X_{grs} and $x(g)$ contour intersections for both the cores and the rims are at effectively the same P–T conditions at 563–583°C/5.8–6.7 kbar, and 560–575 °C/6–6.7 kbar, respectively in the bt-chl-grt-ms-mrg-rt-qtz field. The mismatched mineral is plagioclase.

Fernandes, J.
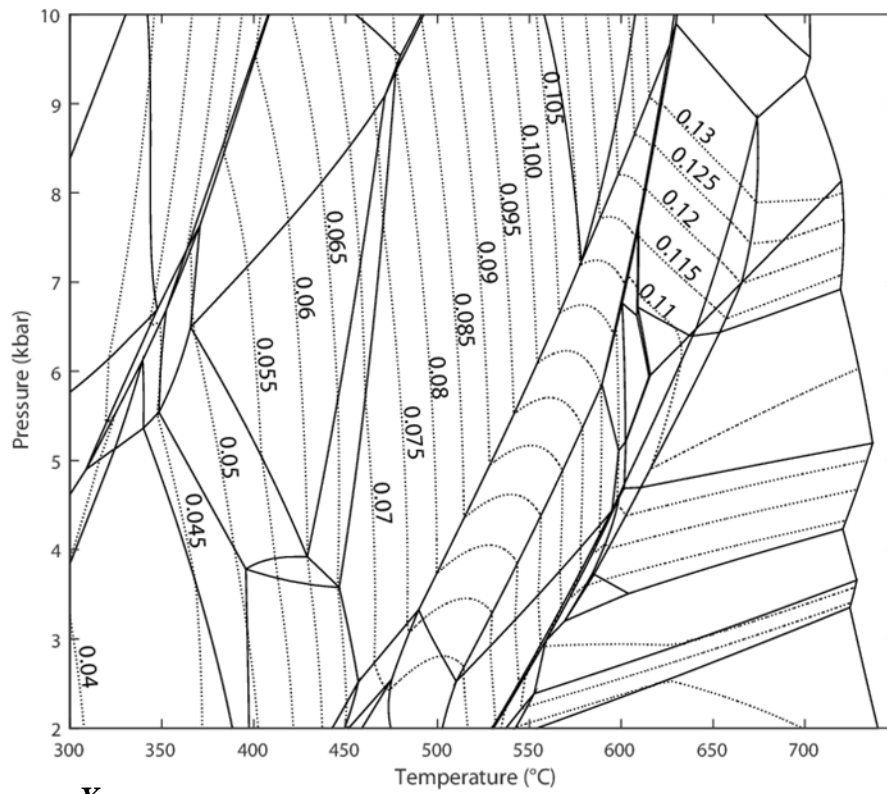
(a) *Garnet mode*

(b) X_{sps}

Fig. 4.30 (cont'd)

Fernandes, J.
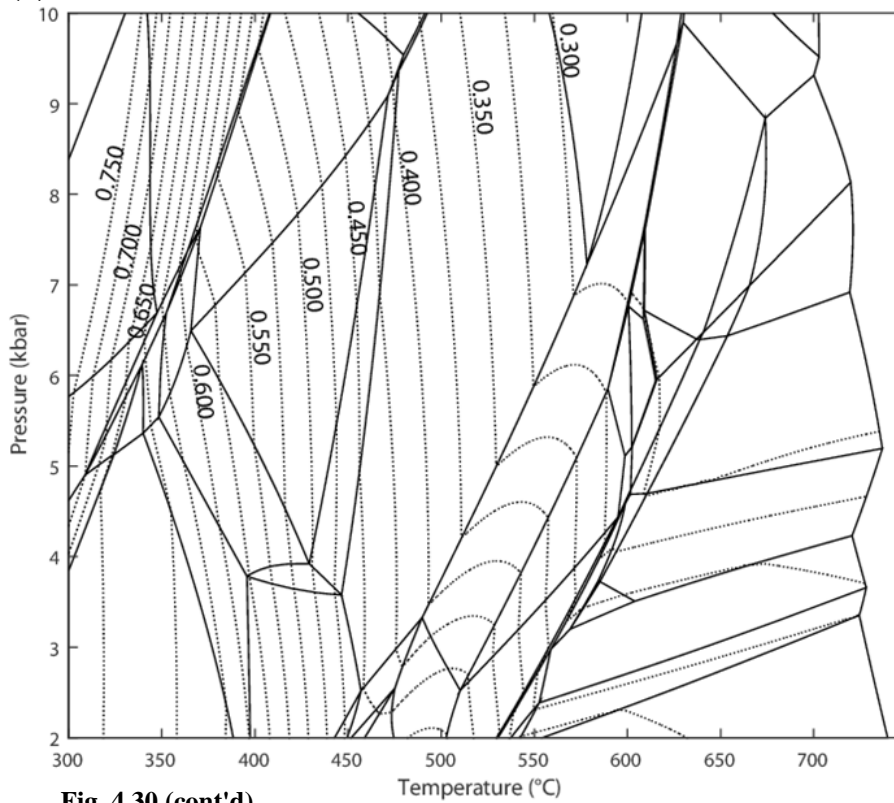
(c) x(g)
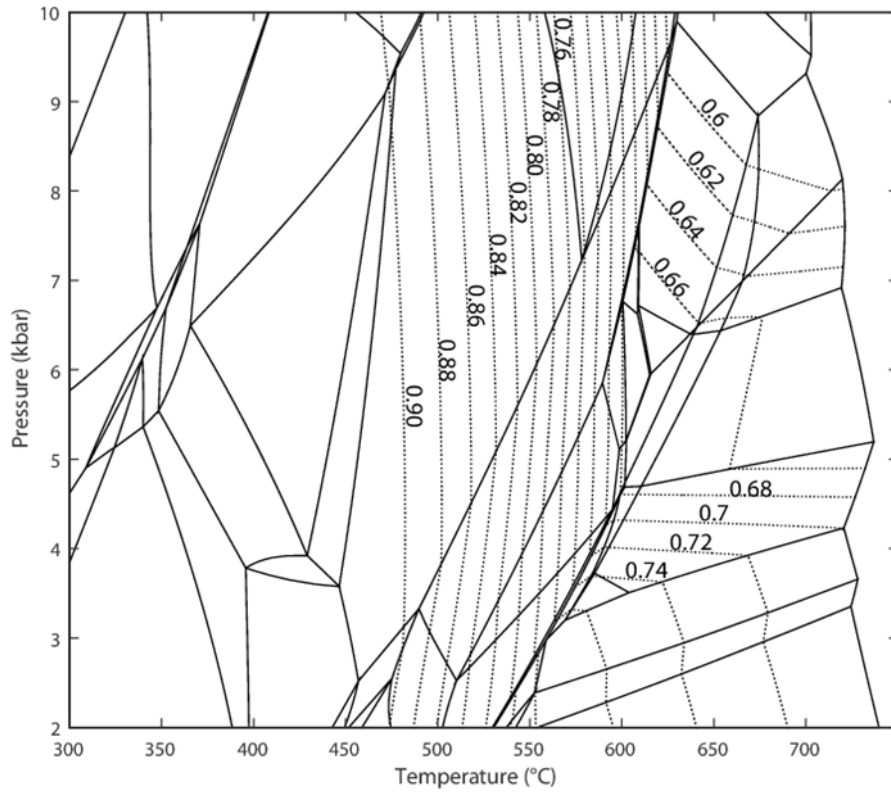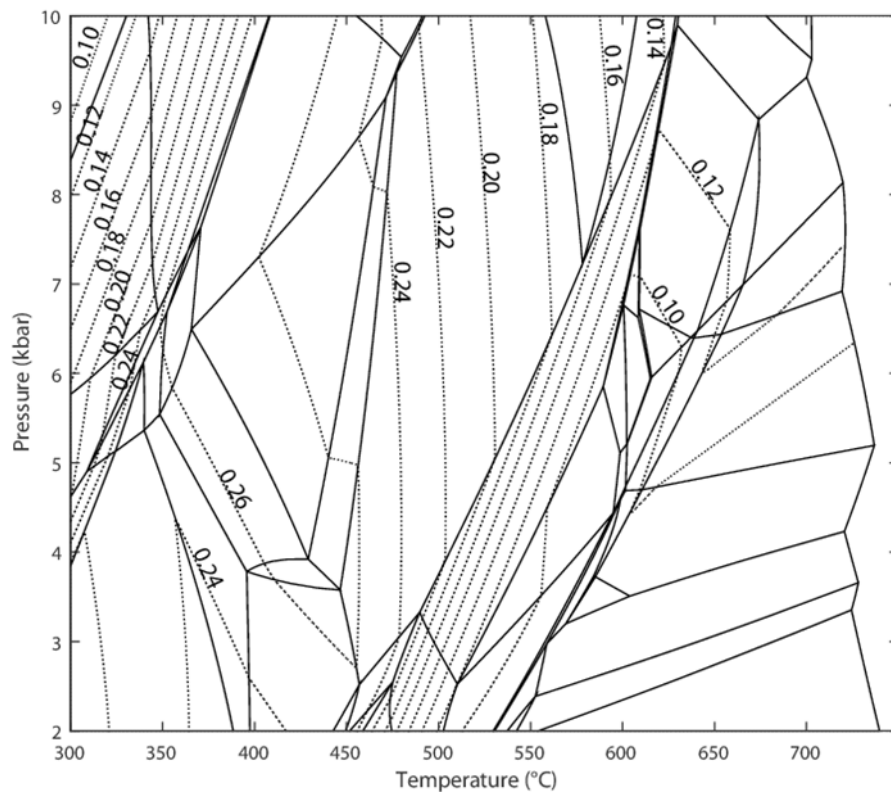
(d) Xgrs

Figure 4.30. *P–T* **pseudosection for J36 contoured for (a) garnet mode, and garnet compositions (b)**
X_{sps}, (c) $x(g)$, and (d) $X_{grs.}$

Fernandes, J.

(a)

Core contours

(b)

Rim contours
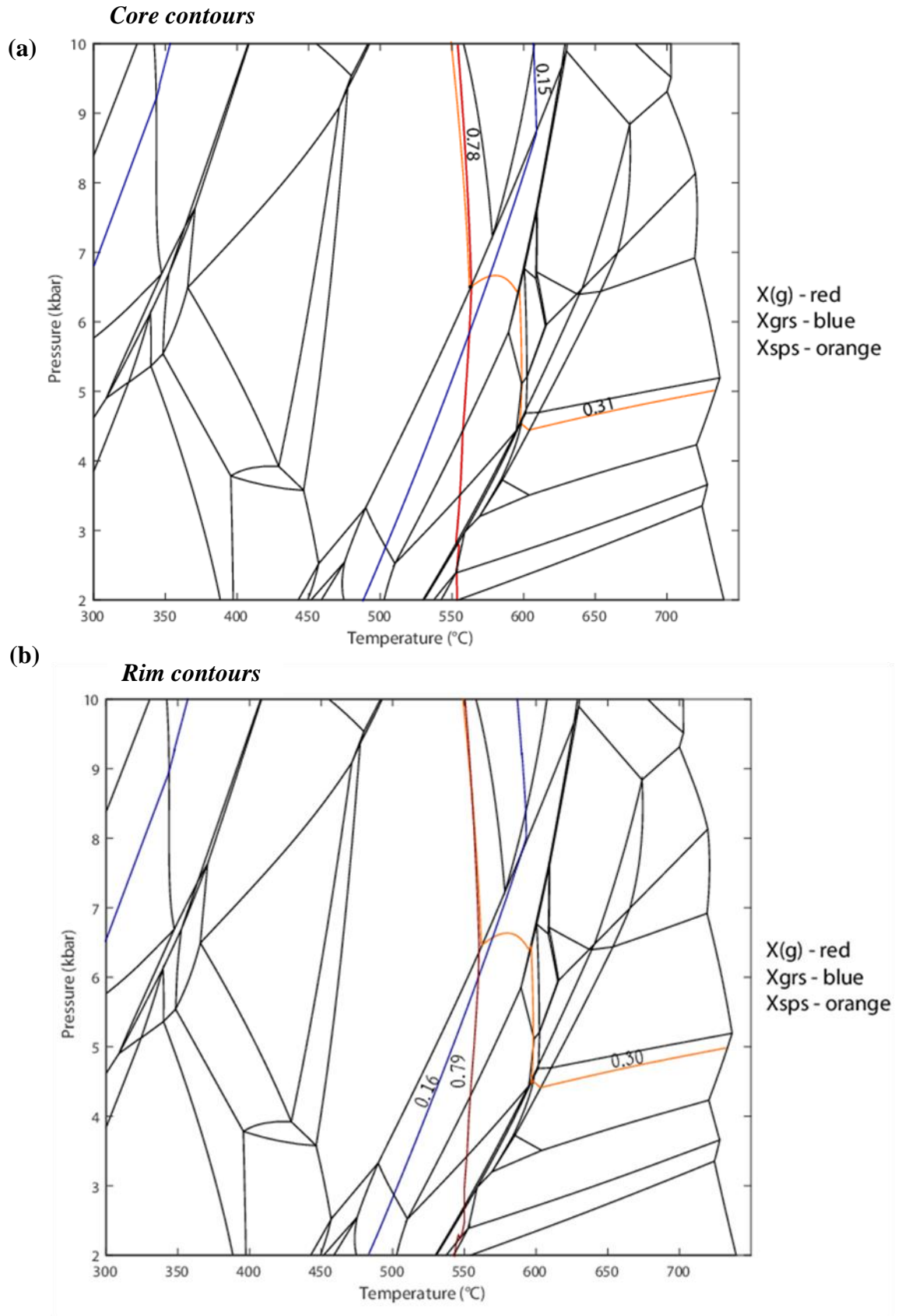
Figure 4.31. Garnet content of X_{sps} in orange, $x(g)$ in red and X_{grs} in blue (a) in core and (b) at rims.

Fernandes, J.

Table 4.5. Representative EPMA garnet compositions for J36.

oxide wt%.	☆Rim	☆Transition	★ Core
SiO_2	37.07	36.33	36.60
Al_2O_3	21.03	20.69	20.75
TiO_2	1.05	0.73	0.61
MgO	3.01	3.24	3.17
FeO_{total}	19.61	19.53	20.02
MnO	13.97	13.99	14.30
CaO	5.87	5.52	5.38
Cr_2O_3	0.00	0.02	0.03
Total	101.61	100.06	100.87

Normalised to 8 cations

Si	2.917	2.900	2.902
Al	1.951	1.947	1.939
Ti	0.062	0.044	0.036
Mg	0.353	0.386	0.375
Fe_{total}	1.290	1.304	1.327
Mn	0.931	0.946	0.961
Ca	0.495	0.472	0.457
Cr	0.000	0.001	0.002
$x(g)$	0.79	0.77	0.78
=Fe/(Fe+Mg)			
$m(g)=X_{sps}$	0.30	0.30	0.31
$z(g)=X_{grs}$	0.16	0.15	0.15
X_{pyp}	0.11	0.12	0.12
X_{alm}	0.42	0.42	0.43

Rim content: x(g) = 0.79, m(g) = 0.30, z(g) = 0.16 used in Fig. 4.32a.
Core contents: x(g) = 0.78, m(g) = 0.31, z(g) = 0.15 used in Fig. 4.32b.
The stars match Fig. 4.28a transect U-U'.

Fernandes, J.

INTERPRETATION

Peak field mismatch

The observed assemblage is qtz-ap-bt-chl-grt-pl-ms-rt. Apatite was taken out from the bulk composition and so it is not modelled into the predicted assemblage. The closest matching pseudosection assemblage is qtz-bt-chl-grt-pl-ms-mrg-rt, which is located at low *P*–*T* conditions, in the vicinity of <3.8 kbar and 475–510 °C. The intersection of both the core and rim composition contours is located at higher *P*–*T* conditions near 6 kbar and 520 °C, in the field qtz-bt-chl-grt-mrg-ms-rt. The contours intersect in a field that is predicted to contain margarite and be oligoclase (plagioclase) absent.

Either, margarite is present in tiny proportions in the rock and is undetected, or it is absent in the rock and incorrectly modelled in the pseudosection.

(1) As the predicted amounts of margarite are very small (0.5–3.5 mode %, Fig. 4.32), it is conceivable that margarite might remain undetected in the rock despite careful, and unsuccessful, searching using EDS methods.

Alternatively, (2) The predicted presence of margarite throughout much of the *P*–*T* pseudosection might be spurious - an unforeseen outcome of selections made in the lead-up to the pseudosection calculations. White *et al*. (2014b) mentions that the presence of margarite in pseudosections has been accompanied by only relatively few cases of real rock occurrences. In these cases margarite occurs as a replacement mineral. He concluded that the stability of margarite represents either: a geologically unlikely combination of CaO and Na_2O contents modelled into the pseudosection; or, an inaccuracy in the *a-x* relations. Oligoclase is present in the rock, but is not present in the modelled pseudosection. Partitioning more Ca into plagioclase, rather than into margarite, would reduce, or completely remove, the stability field of margarite on the *P*–*T* pseudosection. The zigzag in the plagioclase line reduces the extent of the stability field of the identified best fit peak assemblage (red, Fig. 4.29). The diminished field (red, Fig. 4.29) provides *P*–*T* constraints that are inaccurate for the rock, limited by the effect of Ca-partitioning between margarite and plagioclase. A

Fernandes, J.

change in field positions would alter the positions of stability field boundaries involving plagioclase, as well as the positions of garnet composition isopleths.
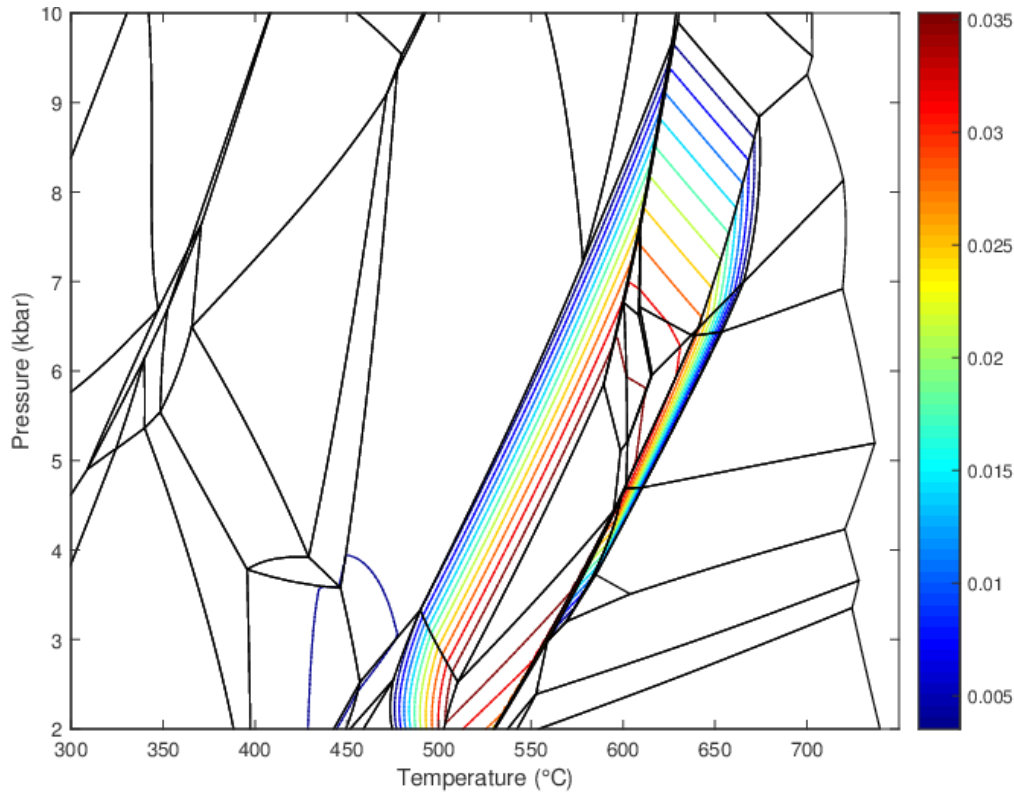
Figure 4.32. Contoured pseudosection for margarite mode. The mode of margarite varies between 0.5% and 3.5%.

Garnet history

The garnets in J36 are all tiny, subtly zoned, occur clustered in deformed bands and show little change in chemical composition from core to rim. Compositional contours (Fig. 4.31a) indicate that they nucleated at temperatures ~563–583°C. The rock is texturally well equilibrated, and shows no signs of polymetamorphism e.g. retrogression and regrowth of garnet, microstructural or chemical discontinuities between garnet growth zones, or multiple generations of garnet (Edmund and Atherthon, 1971; Karabinos, 1984; Gaidies *et al.*, 2006; Majka *et al.*, 2015). The available evidence is consistent with a single episode of garnet growth, over a narrow range of *P–T* conditions. At a later time the rock was subjected to intense small-scale folding. The absence of retrogression may indicate that this folding took place at conditions similar to those at which the garnet grew, or indicates the absence of fluid during the phase of folding.

Fernandes, J.

SAMPLE J35 (28062)

RESULTS

Mineral assemblages and textures

   Thin-section petrography

Sample J35 (Fig 4.33) is comprised mainly of quartz, plagioclase, garnet, hornblende, magnetite, apatite, ilmenite, carbonate and epidote. Representative photomicrographs of this sample are presented in Figure 4.34a–j.
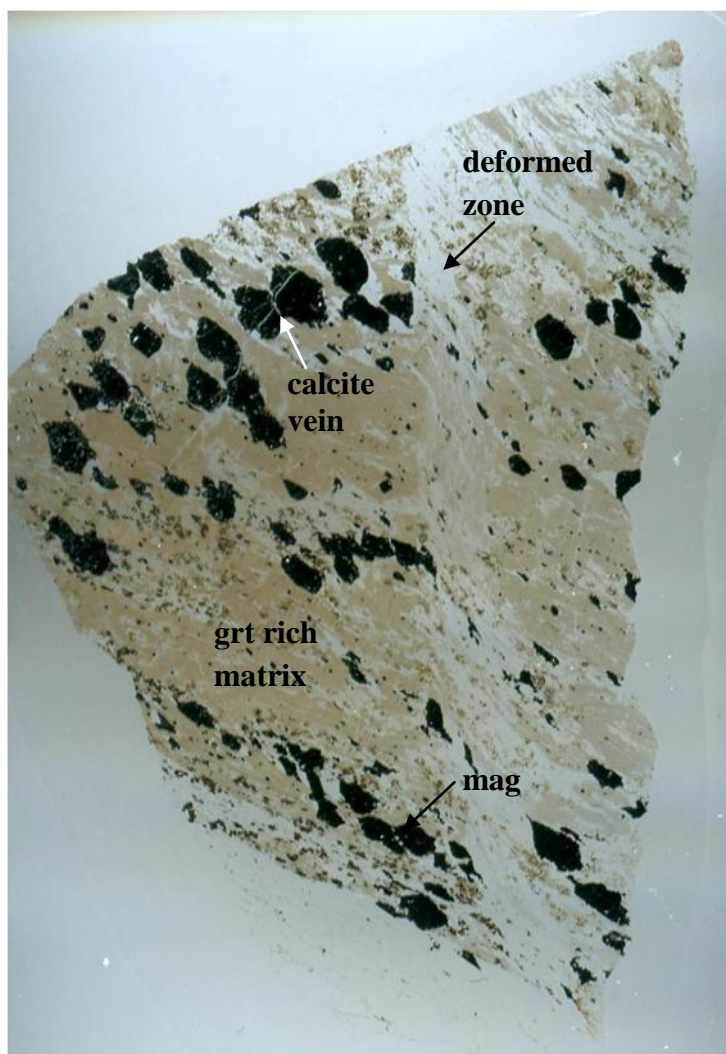
Figure 4.33. Thin section of J35, showing large magnetite porphyroblast (black), fine grained quartz and laminated brown garnet matrix, locally offset by later deformation.

Fernandes, J.
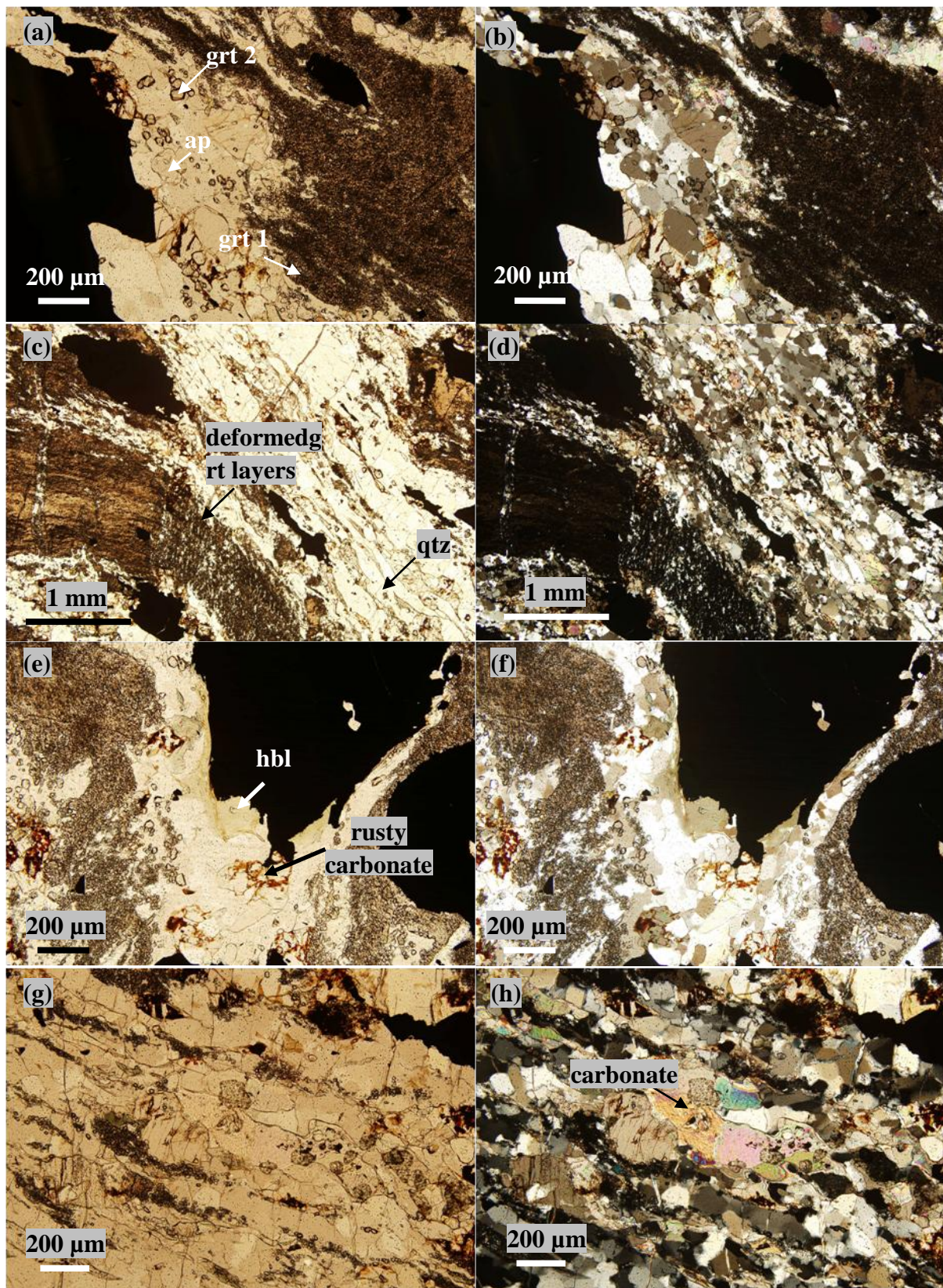
Fig. 4.34 (cont'd)
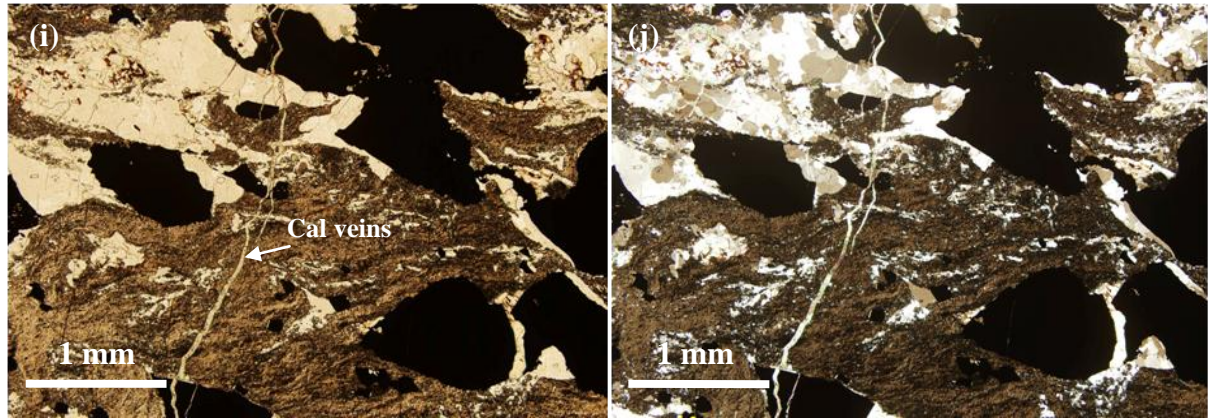
Figure 4.34. Thin section J35 in a, c, e, g and i in plane polarised illumination and b, d, f, h and j in crossed polarised light. Panels a-j show details of the mineral assemblage in J35.

The magnetite occurs as large, rounded or irregularly-shaped porphyroblasts (100 µm–2 mm) within a fine grained quartz (largest grain ~300 µm) and garnet matrix. Abundant, extremely fine-grained brown garnet (grt 1, <30 µm diameter) occurs as dense layers, and scattered, slightly larger (grt 2, largest grain ~ 200 µm) colourless garnet occurs in the intervening, more quartz-rich layers (Fig. 4.34a and 4.34b). Whether the fine brown garnet contains or grew in association with other early minerals could not be determined optically, and was not investigated further.

A later deformation locally cross-cuts and offsets the original compositional layering (Fig. 4.33, 4.34c and 4.34d) of the rock. Hornblende (Fig. 4.34e and f) occurs around the magnetite porphyroblasts, apatite (Fig. 4.34a and b) grows along the compositional layering, ilmenite grows in or at the margins of the magnetite porphyroblasts (distinguishable from magnetite by reflected light microscopy; shown in the µXRF composition maps Fig. 4.35a and SEM-based composition maps Fig. 4.36a) and a late stage calcite vein cross cutting the magnetite (Fig. 4.34i and j). Mica is absent in sample J35.

The bulk composition (Table 4.0) of sample J35 lies in the MnO end of the MnO-K_2O-Na_2O ternary plot (Fig. 4.0). This rock was chosen for study because it lies at the extreme end of the MnO spectrum with a 90.45% proportion of MnO, 9% Na_2O and 0.5% K_2O for cherts. It has a high proportion of Fe, about twice the amount in the other analysed chert cherts.

Micro X-ray fluorescence composition maps

The µXRF maps (Fig. 4.35) show quartz, garnet and large magnetite porphyroblasts with ilmenite, apatite and carbonate. Ilmenite occurrences are associated with the margins around the large magnetite grains, apatite occurs scattered throughout, and carbonate is common in the body of the rock (Fig. 4.35a) as well as late stage veins (Fig. 4.35b).
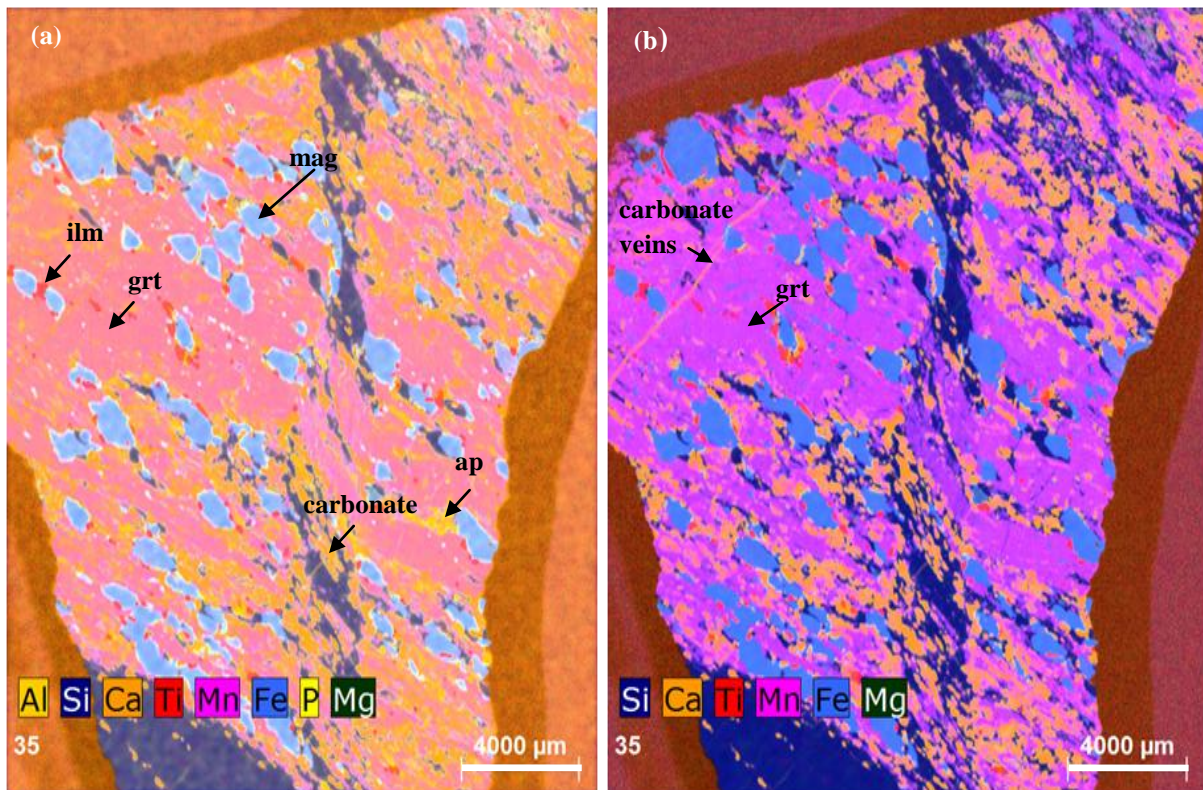
Figure 4.35. The µXRF maps showing fine grained chert with large magnetite porphyroblasts and a zone of deformation vertically across the thin section. a) Mn-rich garnet layers (pink in panel a), apatite (orange - yellow), large grains of magnetite (blue), carbonate (orange) and ilmenite (red). b) Fe- and Mn- rich garnet layers (pink) and quartz layers (dark blue). The carbonate vein (orange, panel b) is a late stage feature.

Fernandes, J.

Scanning Electron Microscopy (SEM)-based composition maps

The EDS element distribution maps show the texture and mineralogy of J35. The magnetite grains are wrapped by fine-grained Fe- and Mn-rich garnet layers. The carbonate occurs as four phases, calcite (Fig. 4.36a and b), Mg-calcite (Fig. 4.36a and b), dolomite (Fig. 4.36b) and a late stage calcite vein (Fig.4.36a).

Fernandes, J.
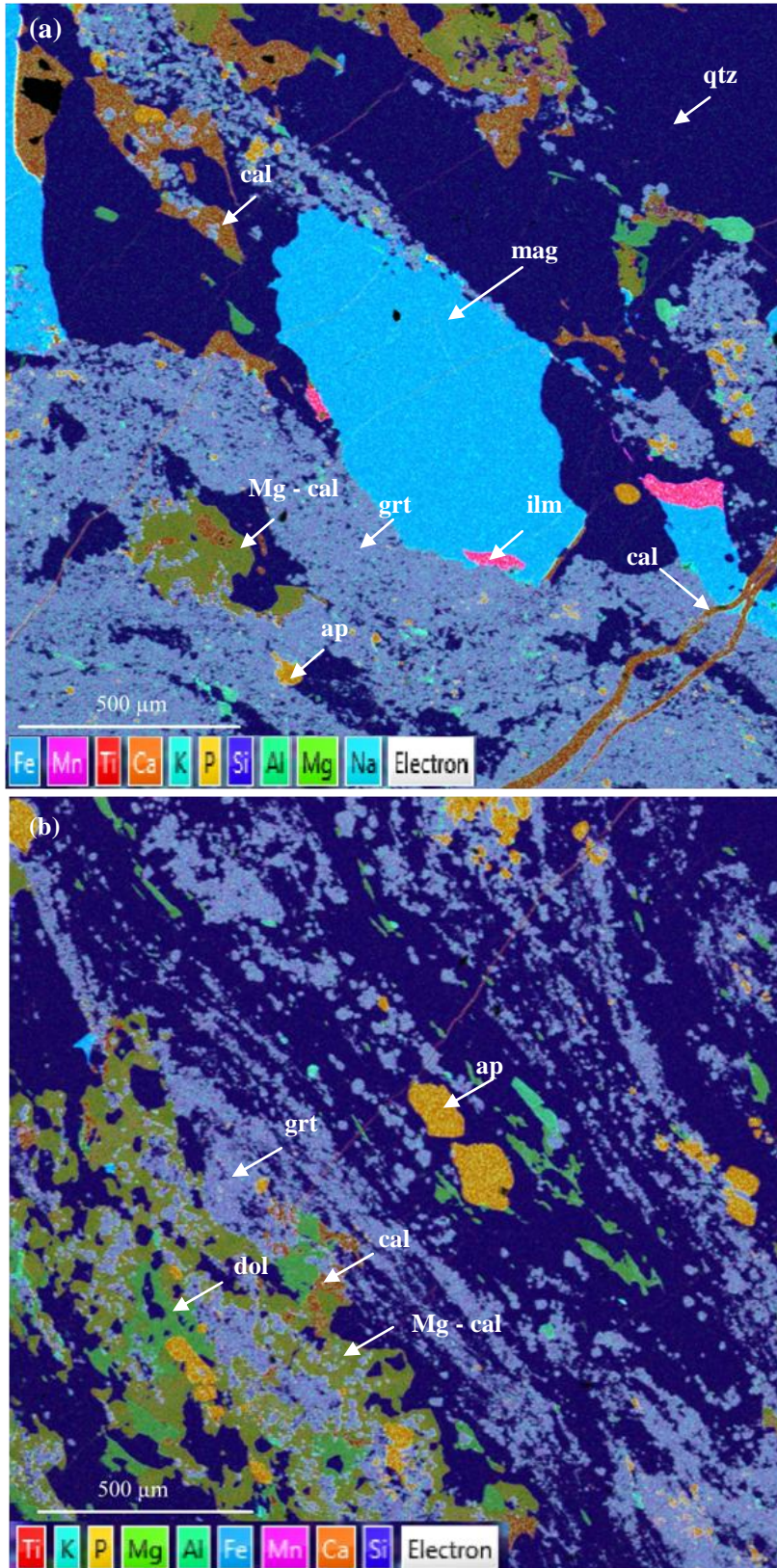
Figure 4.36. SEM composition maps of sample J35. Quartz (dark blue), Mn- and Fe-rich garnet layers (light pink-blue), large magnetite grain (bright blue) with ilmenite grains on the grain borders (red), calcite (brown), Mg-calcite (dull green), apatite (orange), dolomite (dark green) and a carbonate vein (brown).

Electron Probe Micro-Analysis

The results presented here are for the more abundant brown (grt 1) variation of garnet. Figure. 4.37 shows that multiple early garnet nuclei are overgrown by a single rim. The early multiply-nucleated cores of the garnet differ in their chemistry from the rim. Those chemical differences are subtle, seen as brighter cores within the darker rims (Fig. 4.37a). The compositional transect show that the Fe peaks correspond to the bright cores of the garnet. The composition of the garnet core is $X_{sps} \approx 0.30-0.34$, $X_{grs} \approx 0.12-0.21$, $X_{alm} \approx 0.42-0.46$ and $X_{pyp} \approx 0.04-0.06$. The rim composition is $X_{sps} \approx 0.31-0.35$, $X_{grs} \approx 0.15-0.21$, $X_{alm} \approx 0.41-0.45$ and $X_{pyp} \approx 0.05-0.06$.
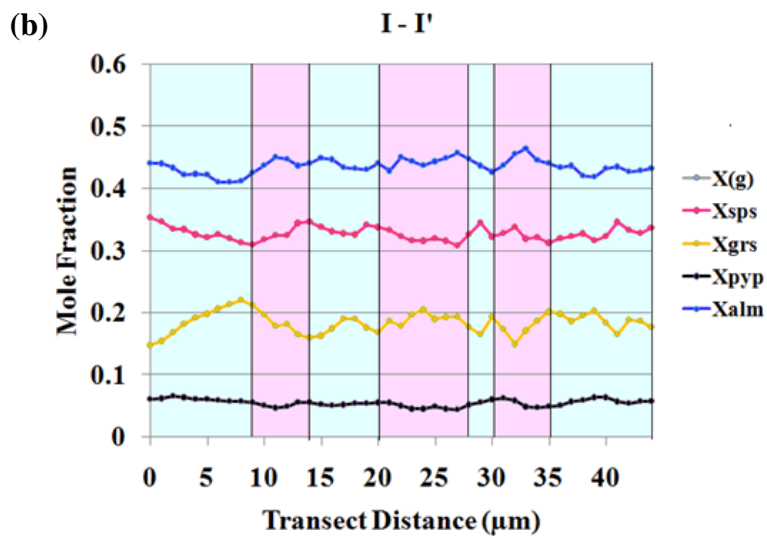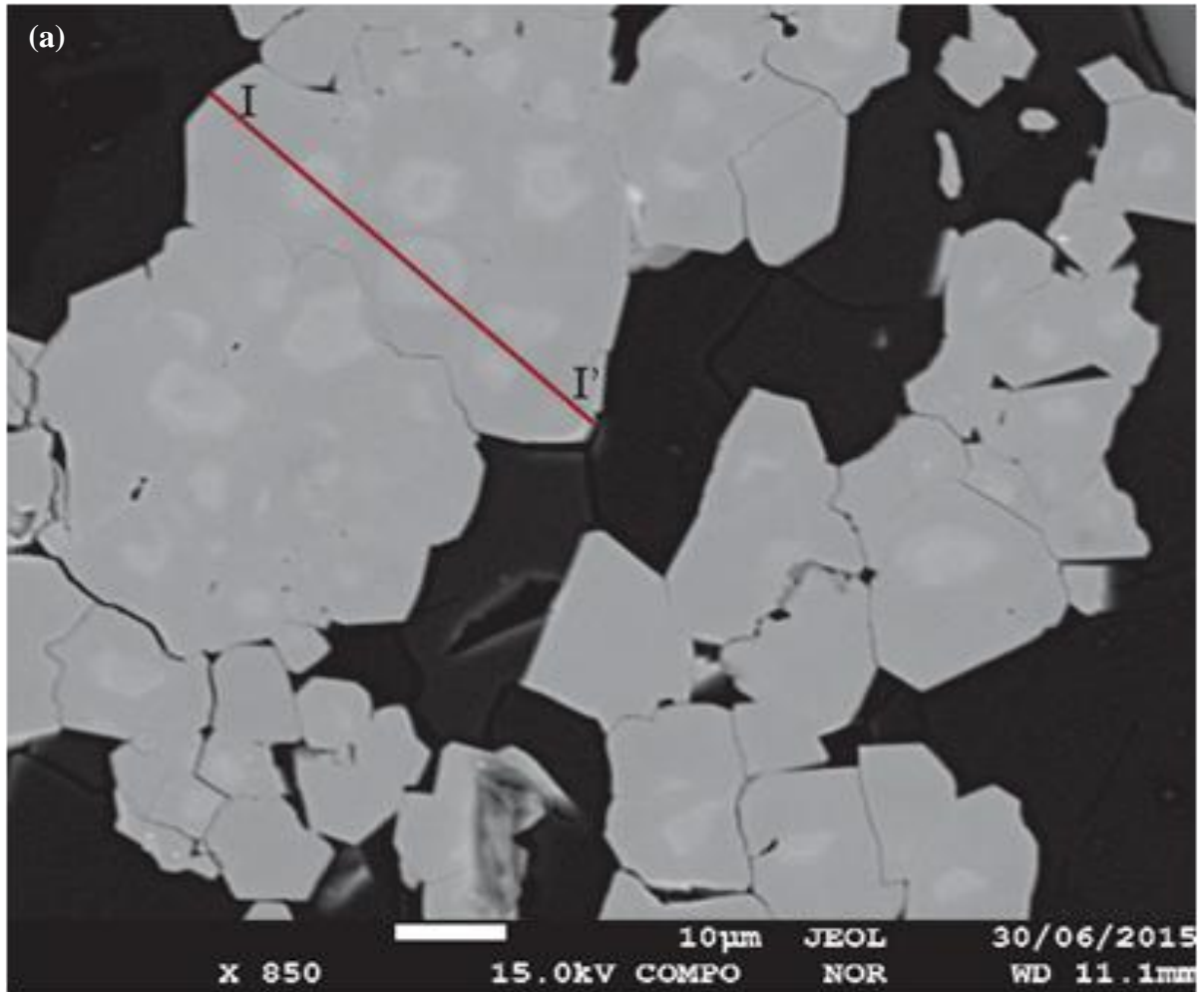
Figure 4.37. BSE image of J35 showing (a) transect I-I' across a multiply nucleated garnet. (b) Compositional transect shows compositional variation with $X_{alm}>X_{sps}>X_{grs}>X_{pyp}$.

Fernandes, J.

Petrographic Forward Modelling

P−T pseudosection

Input Bulk Composition (mol %)

$SiO_2 = 52.98$, $TiO_2 = 0.32$, $Al_2O_3 = 5.11$, $FeO = 21.65$, $MnO = 6.65$, $MgO = 2.21$,
$CaO = 5.63$, $Na_2O = 0.04$, $O = 5.41$.

J35 - All fields contain q and H₂O
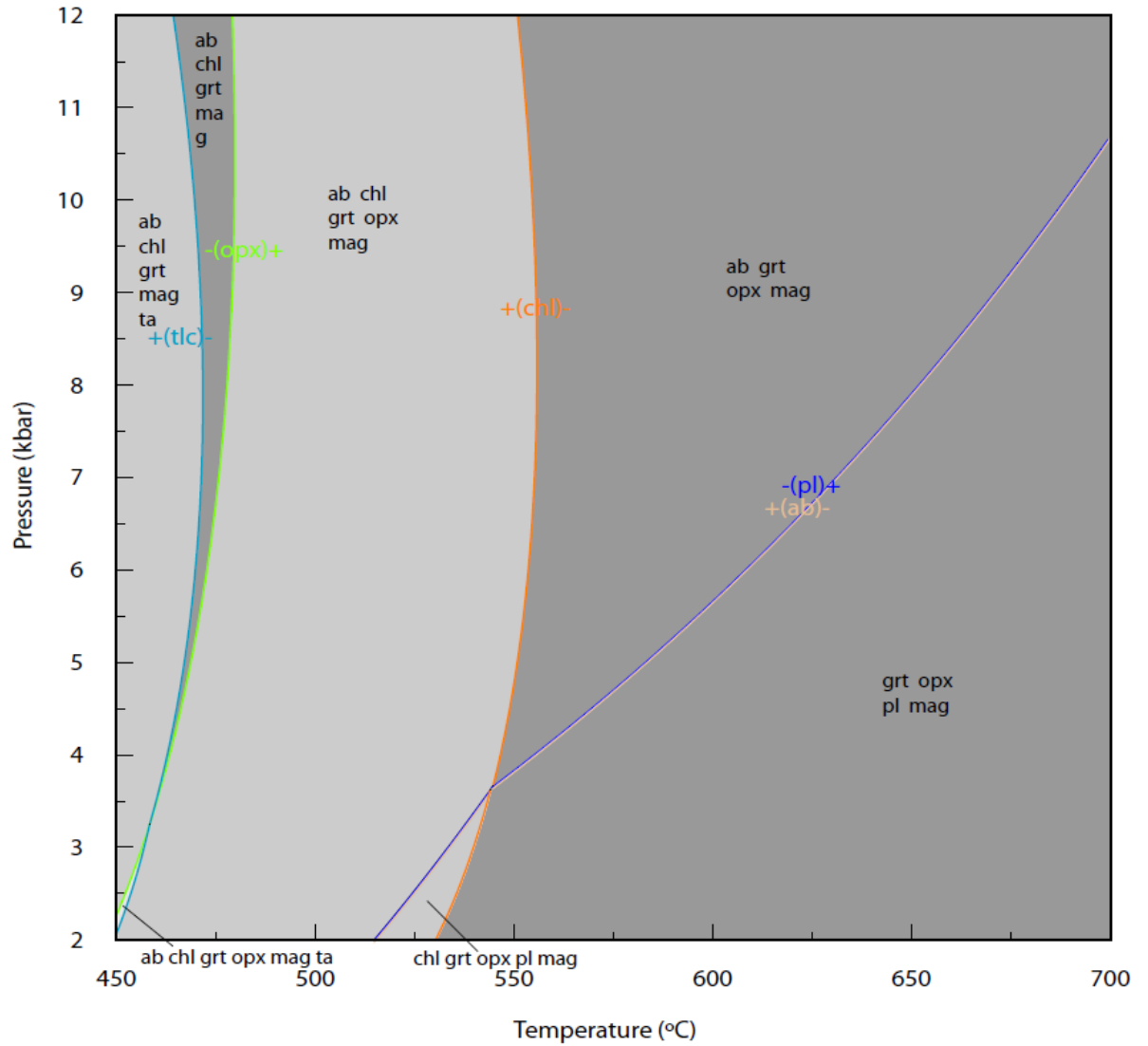
Figure 4.38. Initial *P−T* **pseudosection results for J35, calculated for** *X*H₂O = 1.0, **using THERMOCALC. Carbonate (present in the rock) requires a mixed H₂O-CO₂ fluid, so is not represented here.**

Fernandes, J.

Sample J35 contains amphibole which is not yet implemented in the latest THERMOCALC dataset and $a–x$ models (White *et al*., 2014a). For this reason, the older models White *et al.*, (2007) have been used. The $P–T$ pseudosection for J35 was calculated in a ten-component system MnNCFMASHTO, using White *et al*. (2007) models with the thermodynamic dataset ds55s. The K_2O = 0.01 oxide wt% (Table 4.0), which has been ignored and the calculations are done in a K-free system. The presence of carbonate in the rock requires the consideration of XCO_2 in order to effectively model the pseudosection. In order to find a starting place for more complex mixed fluid calculations, initial calculations (Fig. 4.38) used a pure H_2O fluid.

The pseudosection has an extensive orthopyroxene stability field and does not show the ilmenite, hornblende and epidote. With the simplifications made, the pseudosection is not expected to entirely predict the observed assemblage (since XCO_2 has been ignored), but it fails to match even the minerals that are not affected by the XCO_2 e.g. ilmenite, hornblende and epidote. This makes it highly unreliable as a useful starting point; therefore further calculations were not carried out.

Fernandes, J.

INTERPRETATION

Problems with forward modelling for sample J35

The bulk composition (Table 4.0) of J35 is very rich in Mn, Fe and Ca with MnO = 7.25 wt.%, Fe_2O_3 = 13.29 wt.%, FeO = 11.98 wt.% and CaO = 5.16 wt.% in comparison to other cherts studied in this research, where MnO = 0.64–1.68 wt.%, Fe_2O_3 = 0.13–1.61 wt.%, FeO = 0.94–2.71 wt.% and CaO = 0.54–0.92 wt.% (Table 4.0). Correspondingly, J35 is low in silica with SiO_2 = 48.83 wt.%. Sample J35 is different from other studied cherts in that it contains hornblende, abundant carbonate and bulk chemistry unlike the other metacherts studied here.

Complications arise for the following reasons:

(1) There are texturally two unique garnet groups; one fine grained, occurring clustered together forming layers (grt 1, Fig. 4.34a) and a second (grt 2, Fig. 4.34a), more rare, occurring as single large garnet with no evidence of deformation. There is a primary and secondary carbonate phase. The primary phase is sometimes rusty (Fig. 4.34e) which implies a chemical deterioration of the sample and the secondary calcite (Fig. 4.34i & f) also interferes with the bulk composition. The presence of carbonate requires consideration of a XCO_2 in the pseudosection modelling. In order to calculate pseudosections the fluid phase used for modelling needs to be adjusted to the equilibrium conditions at which the rock grew (Korhonen *et al.*, 2013). The absence of fluid inclusions makes it difficult to robustly constrain the XCO_2 value.

(2) The presence of amphibole in combination with a Mn-rich garnet also poses a problem. The latest Mn models (White *et al.*, 2014a) cannot be used for a rock containing amphibole and the White *et al.* (2007) models are not the latest optimised models for Mn, which make neither of the *a-x* models optimal.

(3) The fine grained nature of this rock makes it difficult to identify some of the numerous smaller minerals that may be present within the brown garnet layers as part of the matrix. Optically, they are sometimes coupled with high relief garnet making it impossible to identify these tiny matrix minerals. With such fine grain matrix, even

Fernandes, J.

high resolution (down to 1 μm) EPMA would encounter beam overlap and excitation volume effects. Assemblages with higher variances in their mineral assemblage have more uncertainties in their reaction histories, making it very difficult to constrain $P-T$ conditions (Vance and Maher, 1998). The fine grained nature of this rock along with the presence of hornblende and four phases of carbonate make it a challenge to model. As stated before, in order to model the hornblende we have used the ds55S (which includes hornblende) and not the latest ds6 (latest models ideal for dealing with Mn-rich compositions) which does not yet include hornblende. Sample J35 is Mn-rich which would require the new models (ds6, White *et al.*, 2014a) to deal with the Mn. But since ds6 does not contain amphibole yet, it was not used. In addition, the Ca-rich chemistry of sample J35 would need mixed fluid calculations, which can only be made once an appropriate starting pseudosection is calculated.

The textural relationships between minerals are unclear. Ilmenite grows along the magnetite margins, with amphibole growing around the magnetite porphyroblast. Garnet occurs as two textural variants, the fine grain deformed layers and the larger isolated garnet, with little textural relationship between the two. Rusted carbonate and late stage veins and deformation of the layers increase the textural complexity of this garnet chert. The unknown equilibrium relationships of the minerals with each other and chronology of phases make it challenging to make assumptions for pseudosection modelling with any certainty. For the aforementioned reasons J35 was not further investigated.

Fernandes, J.

5. CONCLUSIONS

The present research has been conducted using the new $a-x$ Mn models for THERMOCALC (White *et al*., 2014a), for five samples of garnetifierous metachert from the Southern Alps, New Zealand. The garnets within the metacherts may preserve a wealth of extractable information in their textures and chemistry. Compositional data from EPMA of the garnets have been used in combination with pseudosections to understand how these rocks respond to metamorphism.

COMPARISON OF RESULTS WITH RAMAN SPECTROSCOPY TEMPERATURES

The results from the THERMOCALC modelling in this study can be compared to temperature results obtained for nearby Alpine Schist rocks based on Raman Spectroscopy of carbonaceous material (RSCM; Beyssac *et al*., 2016). The RSCM only record a peak temperature; hence comparisons are made with the garnet rim estimates from results of this research. The Table 5.1 below shows that the compared results match well, with a maximum difference of 46 ℃.

Table 5.1. $P-T$ results from the present thermodynamic modelling study in comparison with T results from RSCM.

Sample	$P-T$ from pseudosections	T from RSCM
J34	Rim: 520–550 °C, >7 kbar	Fox Glacier: 526–546 °C
J35	-	Moeraki River: 552–583 °C
J36	Rim: 560–575 °C, 6–6.7 kbar	Franz Josef: 530–571 °C
A12E	Rim: 510 °C, 5.5 kbar	Near Hokitika: 556 °C
AMS01	Rim: 475 °C, >3kbar	Hari Hari: 382–544 °C

SUMMARY OF RESULTS

SAMPLE J34

The initial pseudosection with $X\text{H}_2\text{O} = 1$ calculated for this sample was not representative of its bulk composition, since the presence of dolomite required a mixed H_2O–CO_2 fluid calculation. By examining how the calculated mineral assemblage stability fields shift with changes in $X\text{CO}_2$, it was possible to obtain improved constraints on the composition of the associated mixed H_2O–CO_2 fluid ($X\text{CO}_2 \geq 0.1$). The results of pseudosection calculations for a system involving a mixed fluid with $X\text{CO}_2 \approx 0.2$ probably closely represent the effective bulk composition. Calculating the $P\text{-}T$ pseudosection using $X\text{CO}_2 = 0.2$ resulted in a match between the predicted and the observed mineral assemblage, and a close match to the garnet compositions in the rock. The calculated garnet composition contours constrain $P\text{-}T$ conditions of 475–535 °C/5–9 kbar for the core and 520–550 °C/7–10 kbar for the rim. These results demonstrate applicability of the THERMOCALC modelling to constrain $P\text{-}T$ conditions in these rocks, and the constraints could perhaps be refined even further by continuing the process of iterative calculations. As the garnet is zoned, there would also have been some fractionation of elements into the cores of the growing garnet. Although the effects of this fractionation appear likely to have been comparatively small, they introduce additional uncertainty into estimates of the effective bulk composition. On that basis, attempts to further constrain $X\text{CO}_2$ through a continued process of iterative pseudosection calculations was considered unwarranted.

SAMPLE J35

The textural and compositional complexity of this rock makes it unsuitable for pseudosection studies at the present time. The bulk composition is very Mn, Fe and Ca rich and contains amphibole. The sample has abundant carbonate, both late stage carbonate as well as carbonate that is part of the peak assemblage. The carbonate that is part of the peak assemblage would require a mixed fluid consideration for pseudosection calculations. In addition the White *et al.*(2014a) *a-x* models presently available do not include amphibole or pyroxene, thus are not well-suited to dealing with a rock of this chemistry and mineralogy, so this rock was not investigated further.

Fernandes, J.

SAMPLE J36

This sample proved surprising, as the mineral assemblage is simple, the rock contains no carbonate, the garnet shows very limited compositional zoning, and there is no textural evidence of fluid infiltration that could alter the bulk rock chemistry. All the textural and garnet composition data thus appear consistent with garnet growth over a narrow range of P-T conditions, during a single episode of metamorphism. There was no textural evidence for further garnet growth during later tight folding of the garnet-rich layers, which was probably associated with mylonitisation along the Alpine Fault. The garnet component contours intersect well and provide P–T conditions of 563–583 °C/5.8–6.7 kbar for the core and 560–575 °C/6–6.7 kbar for the rim. But, there is no field on the P-T pseudosection that contains a mineral assemblage matching the observed minerals in the rock. The pseudosection partitioning the Ca into margarite predicts the stability of margarite instead of oligoclase, causing a peak field mismatch. The issue of stability of margarite on the pseudosection and its real rock absence has been previously encountered (White *et al*., 2014b).

SAMPLE A12E

Sample A12E has strongly zoned garnets that cause Mn to be fractionated into the garnet cores. The fractionation effects have been dealt with by removal of the Mn rich cores from the bulk composition forming an effective rock composition with which a recalculation of the pseudosection was done. Sample A12E, was able to provide a tight P-T peak (rim) estimate.

The recalculated pseudosection using a bulk composition with the Mn-rich garnet cores removed, successfully represents both the mineral assemblage in the rock, and the garnet rim compositions, yielding a *P-T* estimate of 510 °C/5.5 kbar. But, the recalculated pseudosection is unable to constrain core *P-T* conditions. The initial garnet nucleation occurred at sites where the local effective bulk composition differed (more Mn-rich), perhaps significantly, from the overall bulk rock composition. Garnet nucleation in Mn-rich rocks is commonly controlled by small-scale compositional variability ± kinetic effects; extracting information about the conditions of early garnet growth (core conditions) along a P–T path may be impossible without detailed studies of the effects of local bulk composition on initial

Fernandes, J.

garnet growth. This rock preserves evidence for diffusion controlled garnet growth and a polymetamorphic history.

SAMPLE AMS01

The pseudosection for this sample represents the rock and contains a field that matches the observed peak assemblage. The peak field on the pseudosection was able to provide only a broad constraint on $P-T$ conditions >475 °C/>3.5 kbar for core and >475 °C/>3 kbar for the rim. Tight constraints were not obtained since the bulk-rock composition did not effectively mimic the effective bulk composition of the rock at the sites of the garnet growth. Compositional variation in the layering or a local variation in the bulk composition may have caused variation in the effective bulk chemistry. A recalculation for this rock would require a detailed study of the effective bulk composition for different layers or for the locality from which the garnets were analysed. Sample AMS01 shows evidence of a single stage metamorphic history. The mechanism for growth of garnet was inferred to be diffusion controlled in this sample.

Fernandes, J.

THE THERMODYNAMIC FORWARD MODELLING OF GARNETIFEROUS METACHERT

This study demonstrates that garnetiferous metacherts can yield useful information of metamorphism using thermodynamic forward modelling techniques (i.e. THERMOCALC). However, several factors have affected the pseudosections during the course of this study:

I.   **ASSUMPTION OF EQUILIBRIUM**

Thermodynamic forward modelling calculations are fundamentally based on the concepts of equilibrium thermodynamics, and rely on the idea that an appropriate effective bulk composition can be defined for the reacting assemblage. Problems may arise if the bulk composition used for the calculations does not successfully mimic the effective bulk composition.

Fractionation

Fractionation of elements (i.e. Mn) into the core of a growing mineral (garnet), removes them from the effective bulk composition, and as a result, the overall bulk composition no longer represents the effective bulk composition available at the time the garnet rims grow. A new effective bulk composition, without the mineral cores, can be estimated and the pseudosections can be recalculated. This approach was successful for sample A12E. Other strongly zoned minerals may also contribute to the effects of fractionation.

Compositional layering and mineral zonation

If the rock does not have homogenous composition, then a bulk composition of the rock may not be representative of the entire rock, as was probably the case for samples A12E, AMS01. In this case, the bulk composition cannot be used for modelling to constrain the P–T conditions of mineral nucleation and early growth. It may be possible to estimate a new effective bulk composition for a small area immediately associated with analysed mineral(s) of interest, using measured mineral

Fernandes, J.

compositions and image analysis. This has not been done in the present study.

Late stage veining

Late-stage fluid flow that can produce features such as veining could also result in a measured bulk rock composition that does not match the effective bulk composition at the time the (peak) metamorphic minerals grew.

Reaction overstepping

When sluggish kinetics cause a phase to be nucleated at P-T's higher than typically expected for that phase, the phase will, at least briefly, be out of equilibrium with the rest of the assemblage. The garnet in AMS01 may have been affected by reaction overstepping (as discussed in 'INTERPRETATIONS' under '**Reaction Overstepping**' of Sample AMS01), and hence might have nucleated at higher P-T conditions than predicted by the peak field. The extent of disequilibrium is dependent on the degree of reaction overstepping, and thus the error of intersection of the isopleths estimating P–T conditions is direct function of the degree of overstepping (Spear *et al*., 2014).

II.   **AN IMPURE FLUID PHASE**

Sample J34 grew in a mixed-fluid system of H_2O and CO_2 (as discussed in 'INTERPRETATIONS' under '*Mixed fluid calculations'* of Sample J34). Hence the oversimplification of modelling the pseudosection in a pure H_2O system is unrepresentative of the metamorphic conditions that this rock experienced.

III.   **A-X MODELS**

The latest Mn *a-x* models of White *et al*. (2014a) have been used in this study to model Mn-rich garnet bearing metachert. This study proves that these new models successfully constrain P–T conditions in these Mn-rich bulk compositions, but highlight some concerns.

Fernandes, J.

i. Stability of margarite: In sample J36, the results of the $P–T$ pseudosection calculations indicated that margarite should be stable. However, in the rock margarite was not found, instead plagioclase (oligoclase) was present. Pseudosection calculations do not take into consideration kinetic effects that affect the growth of margarite (White *et al*., 2014b), causing it to be absent on the pseudosection, but present in the rock. The pseudosection occurrence of margarite has been discussed in the 'INTERPRETATIONS' under '*Peak field mismatch* ' of Sample J36.

ii. Stability of garnet below 300 °C: The conditions below which spessartine is unstable are 414 ± 5 °C/3 kbar; 405 ± 5 °C/2 kbar; 386 ± 10 °C/1 kbar (Hsu, 1968). All of the pseudosections calculated here indicate that the Mn-rich garnet should be stable to temperatures below 300 °C. It appears very likely that the local chemical or kinetic effects may control initial garnet nucleation and growth in very Mn-rich rocks, which the pseudosection calculations using overall bulk rock compositions cannot take cannot take into consideration.

This research demonstrates that good constraints on the $P–T$ conditions derived from the composition of the garnet rims may be obtained if the XCO_2 is low. Lo Pò & Braga (2014) note that the main considerations for thermodynamic forward modelling are an inappropriate assessment of the rock growth conditions that affect the bulk composition and the suitability of *a-x* models. All these factors played an important role in determining the samples that produced good $P–T$ estimates and the ones that did not.

A FINAL REVIEW

The garnetiferous metacherts were successfully investigated for the first time by forward thermodynamic modelling (THERMOCALC).

i. Four of the five metachert samples examined in this study have been successfully modelled using pseudosections, showing how the metamorphic assemblages and mineral compositions of these rocks respond to changing metamorphic conditions, using the latest internally-consistent Mn *a-x* models of White *et al*. (2014a).

ii. Using those pseudosections with mineral composition data for those samples, P–T conditions of samples J34 and J36 have been constrained for garnet core and rims; only an estimate of P–T conditions for the garnet rim was constrained for sample A12E, and only a broad field constrained P-T conditions for sample AMS01. Sample J35 fails to be useful in yielding any P–T constraints. The successful results of T conditions compare well with RSCM results (Beyssac *et al*., 2016).

iii. It has not been possible to obtain P–T paths for the metachert, for the following reasons: P–T constraints were not tight enough to draw a path between the core and rim conditions for samples J34 and AMS01; sample A12E has a tight constraint for the rim, but not for the core. For sample J36 the core and rim conditions overlap leaving no potential for a P–T path to be constrained.

This research shows that garnetiferous metacherts are amenable to thermodynamic forward modelling and can provide good P-T constraints. A mixed fluid composition and zoned garnets can be dealt with, but they add complexity. This study has succeeded in studying the effects of a mixed fluid phase in J34 and its effects on the pseudosection, peak assemblage and P–T conditions. The study also shows the change on topology of the pseudosection with an increase in XCO_2 which stabilises dolomite and calcite. The fractionation effect of strongly zoned garnet cores, on a pseudosection has been observed for sample A12E, and removal of the core lead to slightly lower (1 kbar and 60 °C) P–T conditions for the peak field in this case.

Fernandes, J.

The Mn-bearing $a{-}x$ models of White *et al*. (2014a) are for the most part successful in constraining $P{-}T$ conditions, but results of this research have identified a few concerns that merit further investigation, notably: the calculated stability of margarite where it was not observed in the rock, and the stability of garnet at temperatures below 300 °C.

This is the first study of garnetifierous metachert that provides $P{-}T$ estimates of metamorphism from the Southern Alps. This research has pushed compositional boundaries amenable to thermodynamic forward modelling, in trying to construct pseudosections for metachert. The $a{-}x$ models have successfully dealt with changes in the effective bulk rock composition by removal of Mn-rich garnet cores from the overall bulk rock composition (Sample A12E) and the increase in $X\mathrm{CO}_2$ (Sample J34) providing good estimates of the metamorphism for those metacherts.

Fernandes, J.

REFERENCES

Adams, C. J., & Gabites, J. E., 1985. Age of metamorphism and uplift in the Haast schist group at Haast Pass, Lake Wanaka and Lake Hawea, South Island, New Zealand. *New Zealand Journal of Geology and Geophysics*, **28**(1), 85–96.

Adams, C. J., Bishop, D. G. & Gabites, J. E., 1985. Potassium-argon age studies of a low-grade, progressively metamorphosed greywacke sequence, Dansey Pass, South Island, New Zealand. *Journal of the Geological Society of London*, **142**, 339–349.

Adams, C. J., & Graham, I. J., 1997. Age of metamorphism of Otago Schist in eastern Otago and determination of protoliths from initial strontium isotope characteristics. *New Zealand Journal of Geology and Geophysics*, **40**, 275–286.

Adams, C. J., & Robinson, P., 1993. Potassium-argon age studies of metamorphism/uplift/cooling in Haast Schist coastal sections south of Dunedin, Otago, New Zealand. *New Zealand journal of geology and geophysics*, **36**, 317–325.

Ague, J. J., & Carlson, W. D., 2013. Metamorphism as Garnet Sees It: The Kinetics of Nucleation and Growth, Equilibration, and Diffusional Relaxation. *Elements,* **9**, 439–445.

Atherton, M. P., & Edmunds, W. M., 1966. An electron microprobe study of some zoned garnets from metamorphic rocks. *Earth and Planetary Science Letters*, **1**(4), 185–193.

Batt, G. E., Baldwin, S. L., Cottam, M. A., Fitzgerald, P. G., Brandon, M. T., & Spell, T. L., 2004. Cenozoic plate boundary evolution in the South Island of New Zealand: New thermochronological constraints. *Tectonics*, **23**(4).

Batt, G. E., Braun, J., Kohn, B. P. & McDougall, I., 2000. Thermochronological analysis of the dynamics of the Southern Alps, New Zealand. *Geological Society of American Bulletin*, **112**, 250–266.

Bell, T. H., Rubenach, M. J., & Fleming, P. D., 1986. Porphyroblast nucleation, growth and dissolution in regional metamorphic rocks as a function of deformation partitioning during foliation development. *Journal of Metamorphic Geology*, **4**, 37–67.

Beyssac, O., Cox, S. C., Vry, J., & Herman, F., 2016. Peak metamorphic temperature and thermal history of the Southern Alps (New Zealand). *Tectonophysics*. doi:10.1016/j.tecto.2015.12.024

Fernandes, J.

Blackburn, W. H., & Navarro, E., 1977. Garnet zoning and polymetamorphism in the eclogitic rocks of Isla De Margarita, Venezuela. *Canadian Mineralogist*, **15**, 257–266.

Bruker, 2015. M-4 Tornado. Retrieved from: https://www.bruker.com/products/x-ray-diffraction-and-elemental-analysis/micro-xrf-and-txrf/m4-tornado/overview.html

Cande, S. C., & Stock, J. M., 2004. Pacific—Antarctic—Australia motion and the formation of the Macquarie Plate. *Geophysical Journal International*, **157**(1), 399–414.

Carlson, W. D., 2006. Rates of Fe, Mg, Mn, and Ca diffusion in garnet. *American Mineralogist*, **91**(1), 1–11.

Carlson, W. D., & Denison, C., 1992. Mechanisms of Porphyroblast Crystallization: Results from High-Resolution Computed X-ray Tomography. *Science,* **257**, 1236–1239.

Cesare, B., 1999. Multi-stage pseudomorphic replacement of garnet during polymetamorphism: 1. Microstructures and their interpretation. *Journal of Metamorphic Geology*, **17**, 723–734.

Chamberlain, C. P., Zeitler, P. K., & Cooper, A. F., 1995. Geochronologic constraints of the uplift and metamorphism along the Alpine Fault, South Island, New Zealand. *New Zealand Journal of Geology and Geophysics*, **38**(4), 515–523.

Cheng H., & Cao D., 2015. Protracted garnet growth in high-P eclogite: constraints from multiple geochronology and P–T pseudosection. *Journal of Metamorphic Geology*, **33**, 613–632.

Cooper, A.F., 1970. Metamorphism, structure, and post-metamorphic intrusives of the Haast River area, South Westland, New Zealand. Otago University, unpublished PhD thesis.

Cooper, A. F., 1974. Multiphase deformation and its relationship to metamorphic crystallisation at Haast River, South Westland, New Zealand. *New Zealand Journal of Geology and Geophysics*, **17**(4), 855–880.

Cooper, A.F., 1980. Retrograde alteration of chromian kyanite in metachert and amphibolite whiteschist from the Southern Alps, New Zealand, with implications for uplift on the Alpine Fault. *Contributions to Mineralogy and Petrology*, **75**, 153–164.

Fernandes, J.

Cooper, A. F., & Ireland, T. R., 2013. Cretaceous sedimentation and metamorphism of the western Alpine Schist protoliths associated with the Pounamu Ultramafic Belt, Westland, New Zealand. *New Zealand Journal of Geology and Geophysics*, **56**(4), 188–199.

Craw, D., Rattenbury, M. S., & Johnstone, R. D., 1994. Structures within greenschist facies Alpine Schist, central Southern Alps, New Zealand. *New Zealand Journal of Geology and Geophysics*, **37**(1), 101–111.

Cross, C. B., Diener, J. F. A., & Fagereng, A., 2015. Metamorphic imprint of accretion and ridge subduction in the Pan-African Damara Belt, Namibia. *Journal of Metamorphic Geology,* **33**(6),633–648.

De Capitani, C., & Brown, T., 1987. The computational of chemical equilibrium in complex systems containing non-ideal solutions. *Geochimica et Cosmochimica Acta,* **51**, 2639–2652.

Edmunds, W. M., & Atherton, M. P., 1971. Polymetamorphic evolution of garnet in the Fanad aureole, Donegal, Eire. *Lithos*, **4**(2), 147–161.

Faryad, S. W., & Hoinkes, G., 2004. Complex growth textures in a polymetamorphic metabasite from the Kraubath Massif (Eastern Alps). *Journal of Petrology*, **45**(7), 1441–1451.

Gaidies, F., Abart, R., De Capitani, C., Schuster, R., Connolly, J. A. D., & Reusser, E., 2006. Characterization of polymetamorphism in the Austroalpine basement east of the Tauern Window using garnet isopleth thermobarometry. *Journal of Metamorphic Geology*, **24**(6), 451–475.

Gaidies, F., Petley-Ragan, A., Chakraborty, S., Dasgupta, S., & Jones, P., 2015. Constraining the conditions of Barrovian metamorphism in Sikkim, India: P–T–t paths of garnet crystallization in the Lesser Himalayan Belt. *Journal of Metamorphic Geology*, **33**(1), 23–44.

Gazley, M. F., Vry, J. K., & Boorman, J. C., 2011. P–T evolution in greenstone-belt mafic amphibolites: an example from Plutonic Gold Mine, Marymia Inlier, Western Australia. *Journal of Metamorphic Geology*, **29**(6), 685–697.

Geochemistry, R., 2011. Reflex ioGAS: Data Analysis Software. Retrieved from: http://reflexnow.com/iogas/

Fernandes, J.

Giletti, B. J., 1986. Diffusion effects on oxygen isotope temperatures of slowly cooled igneous and metamorphic rocks. *Earth and Planetary Science Letters*, **77**, 218–228.

Grapes, R., 1993. Barian mica and distribution of barium in metacherts and quartzofeldspathic schists, Southern Alps, New Zealand. *Mineralogical Magazine, London,* **57**, 265–265.

Grapes, R. H., 1995. Uplift and exhumation of Alpine schist, Southern Alps, New Zealand: thermobarometric constraints. *New Zealand Journal of Geology and Geophysics*, **38**, 525–533.

Grapes, R. H., & Hoskin, P., 2004. Epidote group minerals in low-medium pressure metamorphic terranes. *Reviews in Mineralogy & Geochemistry,* **56**, 301–345.

Grapes, R., & Watanabe, T., 1992. Metamorphism and uplift of Alpine schist in the Franz Josef–Fox Glacier area of the Southern Alps, New Zealand. *Journal of Metamorphic Geology*, **10**, 171–180.

Grapes, R. H. & Watanabe, T., 1994. Mineral composition variation in Alpine Schist, Southern Alps, New Zealand: implications for recrystallization and exhumation. *Island Arc*, **3**, 163–181.

Grapes, R., Watanabe, T., & Palmer K., 1985. X.R.F analyses of quartzo feldspathic schists and metacherts Franz Josef-Fox glacier area, Southern Alps of New Zealand, 1–13.

Hay, R., & Craw, D., 1993. Syn-metamorphic gold mineralisation, Invincible Vein, NW Otago Schist, New Zealand. *Mineralium Deposita*, **28**, 90-98.

Hollister, L. S., 1966. Garnet zoning: an interpretation based on the Rayleigh fractionation model. *Science*, **154**(3757), 1647–1651.

Hsu, L. C., 1968. Selected phase relationships in the system Al-Mn-Fe-Si-OH: A model for garnet equilibria. *Journal of Petrology*, **9**(1), 40–83.

Jamieson, R. A., & Craw, D., 1987. Sphalerite geobarometry in metamorphic terranes: an appraisal with implications for metamorphic pressure in the Otago Schist. *Journal of Metamorphic Geology*, **5**, 87–99.

Fernandes, J.

Jugum, D., Norris, R.H., & Palin, J.M., 2013. Late Jurassic detrital zircons from the Haast Schist and their implications for New Zealand terrane assembly and metamorphism. *New Zealand Journal of Geology and Geophysics*, **56**, 223–228.

Karabinos, P., 1984. Polymetamorphic garnet zoning from south-eastern Vermont. *American Journal of Science*, **284**(9), 1008–1025.

King, P. R., 2000. Tectonic reconstructions of New Zealand: 40 Ma to the present. *New Zealand Journal of Geology and Geophysics*, **43**(4), 611–638.

Kohn, M. J., & Spear, F., 2000. Retrograde net transfer reaction insurance for pressure-temperature estimates. *Geology*, **28**(12), 1127–1130.

Konrad-Schmolke, M., Zack, T., O'Brien, P. J., & Jacob, D. E., 2008. Combined thermodynamic and rare earth element modelling of garnet growth during subduction: examples from ultrahigh-pressure eclogite of the Western Gneiss Region, Norway. *Earth and Planetary Science Letters*, **272**(1), 488–498.

Korhonen, F. J., Brown, M., Clark, C., & Bhattacharya, S., 2013. Osumilite–melt interactions in ultrahigh temperature granulites: phase equilibria modelling and implications for the P–T–t evolution of the Eastern Ghats Province, India. *Journal of Metamorphic Geology*, **31**(8), 881–907.

Korhonen, F. J., Clark, C., Brown, M., & Taylor, R. J. M., 2014. Taking the temperature of Earth's hottest crust. *Earth and Planetary Science Letters*, **408**, 341–354.

Kretz, R., 1983. Symbols for rock-forming minerals. *American Mineralogist*, **68**, 277–279.

Little, T. A., Cox, S., Vry, J. K., & Batt, G., 2005. Variations in exhumation level and uplift rate along the oblique-slip Alpine Fault, central Southern Alps, New Zealand. *Geological Society of America Bulletin*, **117**, 707–723.

Little, T. A., Holcombe, R. J., & Ilg, B. R., 2002a. Ductile fabrics in the zone of active oblique convergence near the Alpine Fault, New Zealand: identifying the neotectonic overprint. *Journal of Structural Geology*, **24**(1), 193–217.

Little, T. A., Holcombe, R. J., & Ilg, B. R., 2002b. Kinematics of oblique collision and ramping inferred from microstructures and strain in middle crustal rocks, central Southern Alps, New Zealand. *Journal of Structural Geology*, **24**(1), 219–239.

Fernandes, J.

Little, T. A., Mortimer, N. & McWilliams, M. O., 1999. An episodic Cretaceous cooling model for the Otago-Marlborough Schist, New Zealand, based on $^{40}Ar/^{39}Ar$ white mica ages. *New Zealand Journal of Geology and Geophysics*, **42**(3), 305–325.

Lo Pò, D., & Braga, R., 2014. Influence of ferric iron on phase equilibria in greenschist facies assemblages: the hematite-rich metasedimentary rocks from the Monti Pisani (Northern Apennines). *Journal of Metamorphic Geology*, **32**(4), 371–387.

Majka, J., Kośmińska, K., Mazur, S., Czerny, J., Piepjohn, K., Dwornik, M., &Manecki, M., 2015. Two garnet growth events in polymetamorphic rocks in southwest Spitsbergen, Norway: insight in the history of Neoproterozoic and early Paleozoic metamorphism in the High Arctic. *Canadian Journal of Earth Sciences*, **52**(12), 1045–1061.

MacKinnon, T. C., 1983. Origin of the Torlesse terrane and coeval rocks, South Island, New Zealand. *Geological Society of America Bulletin*, **94**(8), 967–985.

Mortimer, N., 2000. Metamorphic discontinuities in orogenic belts: example of the garnet-biotite-albite zone in the Otago Schist, New Zealand. *International Journal of Earth Science*, **89**, 295–306.

Mortimer, N., & Cooper, A. F., 2004. U-Pb and Sm-Nd ages from the Alpine Schist, New Zealand. *New Zealand Journal of Geology and Geophysics*, **47**(1), 21–28.

Nabelek, P. I., & Chen, Y., 2014. The initial garnet-in reaction involving siderite–rhodochrosite, garnet re-equilibration and P–T–t paths of graphitic schists in the Black Hills orogen, South Dakota, USA. *Journal of Metamorphic Geology*, **32**(2), 133–150.

Norris, R. J., & Cooper, A. F., 1995. Origin of small-scale segmentation and transpressional thrusting along the Alpine fault, New Zealand. *Geological Society of America Bulletin*, **107**(2), 231–240.

Norris, R. J., Koons, P. O. & Cooper, A. F., 1990. The obliquely–convergent plate boundary in the south Island of New Zealand: implications for ancient collision zones. *Journal of Structural Geology*, **12**, 715–725.

Okamoto, K., Jahn, B., Yui, T. F., & Akasaka, M., 2013. Redox state at ultrahigh-pressure metamorphism: Constraint from the Chinese Continental Scientific Drilling eclogites. *Island Arc*, **22**(1), 25–36.

Fernandes, J.

Pearce, M. A., White, A. J. R., & Gazley, M. F., 2015. TCInvestigator: automated calculation of mineral mode and composition contours for thermocalc pseudosections. *Journal of Metamorphic Geology*, **33**(4), 413–425.

Pepper, A, 2000. Metamorphism and fluid processed in the mylonitised Alpine Schist, south east of Hokitika, South Island, New Zealand. Unpublished BSc Honours thesis, lodged in the Library, Victoria University of Wellington, New Zealand.

Powell, R., & Holland, T., 1988. An internally consistent dataset with uncertainties and correlations; 3, Applications to geobarometry, worked examples and a computer program. *Journal of Metamorphic Geology*, **6**, 173–204.

Powell, R., & Holland, T., 2008. On thermobarometry. *Journal of Metamorphic Geology*, **26**(2), 155–179.

Powell, R., Holland, T., & White, R., 2009. THERMOCALC. Retrieved from: http://www.metamorph.geo.uni-mainz.de/thermocalc/

Powell, R., & Holland, T., 2010. Using equilibrium thermodynamics to understand metamorphism and metamorphic rocks. *Elements*, **6**(5), 309–314.

Prakash, D., Arima, M., & Mohan, A., 2007. Ultrahigh-temperature mafic granulites from Panrimalai, south India: Constraints from phase equilibria and thermobarometry. *Journal of Asian Earth Sciences*, **29**(1), 41–61.

Prinz, M., Manson, D. V., Hlava, P. F., & Keil, K., 1975. Inclusions in diamonds: garnet lherzolite and eclogite assemblages. *Physics and Chemistry of the Earth*, **9**, 797–815.

Purwin, H., Lauterbach, S., Brey, G. P., Woodland, A. B., & Kleebe, H. J., 2013. An experimental study of the Fe oxidation states in garnet and clinopyroxene as a function of temperature in the system $CaO–FeO–Fe_2O_3–MgO–Al_2O_3–SiO_2$: implications for garnet–clinopyroxene geothermometry. *Contributions to Mineralogy and Petrology*, **165**(4), 623–639.

Raith, M., Raase, P., & Reindhart, J., 2012. A guide to Thin Section Microscopy. 2nd Edition, 127p.
Retrieved from:
http://www.minsocam.org/msa/openaccess_publications/Thin_Sctn_Mcrscpy_2_rdcd_eng.pdf*ISBN 978-3-00-037671-9*

Fernandes, J.

Schmaltz, J., 2007. The South Island, New Zealand. NASA Global Forecasting System. Retrieved from http://earthobservatory.nasa.gov/IOTD/view.php?id=3101

Simpson, G. D., Cooper, A. F., & Norris, R. J., 1994. Late Quaternary evolution of the Alpine fault zone at Paringa, South Westland, New Zealand. *New Zealand Journal of Geology and Geophysics*, **37**(1), 49–58.

Spear, F. S., Thomas, J. B., & Hallett, B. W., 2014. Overstepping the garnet isograd: a comparison of QuiG barometry and thermodynamic modeling. *Contributions to Mineralogy and Petrology*, **168**(3), 1–15.

Spear, F. S., & Daniel, C. G., 1998. Three-dimensional patterns of garnet nucleation and growth. *Geology,* **26**, 503–506.

Spear, F. S., & Daniel, C. G., 2001. Diffusion control of garnet growth, Harpswell Neck, Maine, USA. *Journal of Metamorphic Geology*, **19**, 179–195.

St-Onge, M. R., 1987. Zoned Poikiloblastic Garnets: *P-T* Paths and Syn-Metamorphic Uplift through 30 km of Structural Depth, Wopmay Orogen, Canada. *Journal of Petrology,* **28**(1), 1–21.

Sutherland, R., 1999. Cenozoic bending of New Zealand basement terranes and Alpine Fault displacement: a brief review. *New Zealand Journal of Geology and Geophysics*, **42**(2), 295–301.

Sutherland, R., Berryman, K., & Norris, R., 2006. Quaternary slip rate and geomorphology of the Alpine fault: Implications for kinematics and seismic hazard in southwest New Zealand. *Geological Society of America Bulletin*, **118**(3–4), 464–474.

Taylor, R. J., Clark, C., Johnson, T. E., Santosh, M., & Collins, A. S., 2015. Unravelling the complexities in high-grade rocks using multiple techniques: the Achankovil Zone of southern India. *Contributions to Mineralogy and Petrology*, **169**(5), 1–19.

Tenzer, R., Sirguey, P., Rattenbury, M., & Nicolson, J., 2010. A digital rock density map of New Zealand. *Computers and Geosciences,* **37**, 1181–1191.

Thakur, S. S., Patel, S. C., & Singh, A. K., 2015. A *P–T* pseudosection modelling approach to understand metamorphic evolution of the Main Central Thrust Zone in the Alaknanda valley, NW Himalaya. *Contributions to Mineralogy and Petrology*, **170**(1), 1–26.

Fernandes, J.

Tippett, J.M., Kamp, P.J.J., 1993. The role of faulting in rock uplift in the Southern Alps. *New Zealand Journal of Geology and Geophysics*, **36**(4), 497−504.

Toteu, S. F., & Macaudière, J., 1984.Complex synkinematic and postkinematic garnet porphyroblast growth in polymetamorphic rocks. *Journal of Structural Geology*, **6**(6), 669−677.

Toy, V. G., Craw, D., Cooper, A. F., & Norris, R. J., 2010. Thermal regime in the central Alpine Fault zone, New Zealand: Constraints from microstructures, biotite chemistry and fluid inclusion data. *Tectonophysics*, **485**(1), 178–192.

Toy, V.G., Prior, D.J., Norris R.J., 2008. Quartz textures in Alpine Fault mylonites: influence of pre-existing preferred orientations on fabric development during uplift. *Journal of Structural Geology,* **30**(1), 602–621.

Tuccillo, M. E., Essene, E. J., & van der Pluijm, B. A., 1990. Growth and retrograde zoning in garnets from high-grade, metapelites: Implications for pressure-temperature paths. *Geology*, **18**, 839−842.

Vance, D., & Mahar, E., 1998. Pressure-temperature paths from P-T pseudosections and zoned garnets: potential, limitations and examples from the Zanskar Himalaya, NW India. *Contributions to Mineralogy and Petrology*, **132**(3), 225–245.

von Bohlen, A., 2009. Total reflection X-ray fluorescence and grazing incidence X-ray spectrometry—tools for micro-and surface analysis. A review. *Spectrochimica Acta Part B: Atomic Spectroscopy*, **64**(9), 821–832.

Vry, J. K., Baker, J., Maas, R., Little, T. A., Grapes, R., & Dixon, M., 2004. Zoned (Cretaceous and Cenozoic) garnet and the timing of high grade metamorphism, Southern Alps, New Zealand. *Journal of Metamorphic Geology*, **22**(3), 137–157.

Vry, J., Powell, R., & Williams, J., 2008. Establishing the *P–T* path for Alpine Schist, Southern Alps near Hokitika, New Zealand. *Journal of Metamorphic Geology*, **26**, 81–97.

Walcott, R. I., 1998. Modes of oblique compression: Late Cenozoic tectonics of the South Island of New Zealand. *Reviews of Geophysics*, **36**, 1–26.

Walker, N.W., & Mortimer, N., 1999. Dating high-grade metamorphic mineral growth in the Haast schist using U-Pb TIMS. *Geological Society of New Zealand Miscellaneous Publication*, **107 A**, 167.

Fernandes, J.

Wallace, R., 1975. Staurolite from Haast Schist in the South Westland. *New Zealand Journal of Geology and Geophysics,* **18**, 343–348.

Wellman, H. W., 1972. Rate of horizontal fault displacement in New Zealand. *Nature*, **237**, 275–277.

White, S., 1996. Composition and zoning of garnet and plagioclase in Haast Schist, northwest Otago, New Zealand: implications for progressive regional metamorphism. *New Zealand Journal of Geology and Geophysics*, **39**(4), 515–531.

White, R. W., Powell, R., & Holland, T. J. B., 2007. Progress relating to calculation of partial melting equilibria for metapelites. *Journal of Metamorphic Geology*, **25**(5), 511–527.

White, R. W., Powell, R., Holland, T. J. B., Johnson, T. E., & Green, E. C. R., 2014b. New mineral activity–composition relations for thermodynamic calculations in metapelitic systems. *Journal of Metamorphic Geology*, **32**(3), 261–286.

White, R. W., Powell, R., & Johnson, T. E., 2014a. The effect of Mn on mineral stability in metapelites revisited: new a–x relations for manganese-bearing minerals. *Journal of Metamorphic Geology*, **32**(8), 809–828.

Yardley, B. W., 1977. An empirical study of diffusion in garnet. *American Mineralogist*, **62**, 793–800.

Yardley, B. W., 1982. The early metamorphic history of the Haast Schists and related rocks of New Zealand. *Contributions to Mineralogy and Petrology*, **81**, 317–327.

Zhang, Z., Yang, Y., &Zhang, J., 2000. The compositional zoning of garnet in eclogite from western segment of Altyn Tagh, northwestern China and its dynamic significance. *Chinese Science Bulletin,* **45** (1), 79–83.

Zheng, Y. F., Wang, Z. R., Li, S. G., & Zhao, Z. F., 2002. Oxygen isotope equilibrium between eclogite minerals and its constraints on mineral Sm-Nd chronometer. *Geochimica et Cosmochimica Acta*, **66**, 625–634.

Fernandes, J.